Sol electrophoretic growth of oxide nanostructures: Synthesis, properties and modeling

Steven J. Limmer

A dissertation
submitted in partial fulfillment of the
requirements for the degree of

Doctor of Philosophy

University of Washington

2004

Program Authorized to Offer Degree:

Materials Science and Engineering

University of Washington

Graduate School

This is to certify that I have examined this copy of a doctoral dissertation by

Steven J. Limmer

and have found that it is complete and satisfactory in all respects,
and that any and all revisions required by the final
examining committee have been made.

Chair of Supervisory Committee:

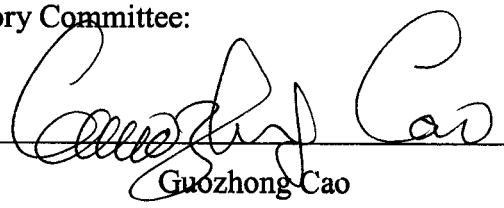

Guozhong Cao

Reading Committee:

Guozhong Cao

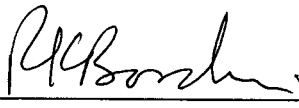

Rajendra K. Bordia

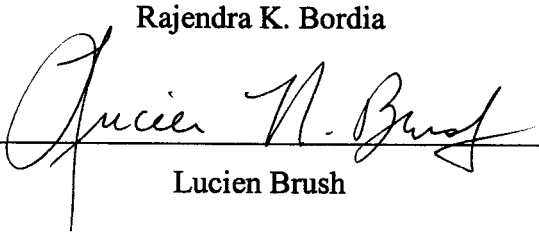

Lucien Brush

J. W. Rogers, Jr

Date: 5/28/2001

In presenting this dissertation in partial fulfillment of the requirements for the doctoral degree at the University of Washington, I agree that the Library shall make its copies freely available for inspection. I further agree that extensive copying of the dissertation is allowable only for scholarly purposes, consistent with "fair use" as prescribed in the U.S. Copyright Law. Requests for copying or reproduction of this dissertation may be referred to Proquest Information and Learning, 300 North Zeeb Road, Ann Arbor, MI 48106-1346, to whom the author has granted "the right to reproduce and sell (a) copies of the manuscript in microform and/or (b) printed copies of the manuscript made from microform."

Signature 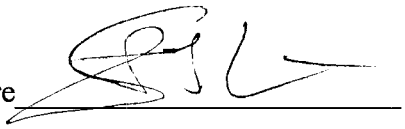

Date 6/2/2004

University of Washington

Abstract

Sol electrophoretic growth of oxide nanostructures: Synthesis, properties and modeling

Steven J. Limmer

Chair of the Supervisory Committee:
Associate Professor Guozhong Cao
Materials Science and Engineering

There is great interest in the ability to form oxide (especially complex oxide) nanorods, given the number of functional properties exhibited by oxide materials. This research examines the template-based growth of nanorods of several oxide ceramics, formed by means of a combination of sol-gel processing and electrophoretic deposition. While sol electrophoretic deposition has been known for some time as a technique for formation of films, this work pioneers its use for the formation of nanorods.

Both single metal oxides (TiO_2, SiO_2) and complex oxides ($BaTiO_3$, $Sr_2Nb_2O_7$, and $Pb(Zr_{0.52}Ti_{0.48})O_3$) have been grown by this method. Uniformly sized nanorods of about 45-200 nm in diameter and 10-60 μm in length were grown over large areas with near unidirectional alignment. Desired stoichiometric chemical composition and crystal structure of the oxide nanorods was readily achieved by an appropriate procedure of sol preparation, with a heat treatment for crystallization and densification. A systematic study of the influence of the several processing parameters was undertaken to determine optimal processing conditions. Preliminary property measurements for several oxide nanorod systems are also reported.

In addition, this work presents and discusses the formation and properties of silica and titania nanorods encapsulated with a thin gold shell. Nanorods of silica and titania ~10 μm in length and with diameters ~ 90-200 nm are made by combining sol-gel electrophoresis with a suitable template. After removing the template at high

temperature, the surface of the rods is re-hydrolyzed by heating in water. 3-Aminopropyltrimethoxysilane is reacted with the surface hydroxyl groups, self-assembling amine functionality on the surface of the rods. These groups act as anchoring sites for the gold, which forms a thin shell around the oxide nanorod. UV-vis absorbance spectra of these samples are analyzed to determine the relationships between shell thickness, core size, core material and properties.

Table of Contents

Page

List of Figures

Figure Number Page

List of Tables

Table Number Page

1 Introduction and background

1.1 Introduction

Oxides possess many important physical properties conducive to a wide range of applications. Examples include electronic and ionic conductors, semiconductors, dielectrics, ferroelectrics, piezoelectrics, pyroelectrics, electro-optics, magnets and high T_c superconductors. In addition, they offer excellent thermal and chemical stabilities. The physical and functional properties of these materials are highly sensitive to chemical stoichiometry, crystallinity and microstructure, and thus can be tailored by doping, or by controlling the crystal structure and microstructure. There is, therefore, no doubt nanostructured oxides would play an important role in nanotechnology.

Nanoscale material synthesis has been an active research area over the past few years, because of the wide variety of interesting behaviors seen in nanomaterials. For instance, some materials show markedly different properties when their size is suitably constrained, and nano-sized materials give scientists an opportunity to analyze many quantum phenomena, which were previously inaccessible for study. The drive towards fabrication of ever-smaller sized materials is also reflected in the microelectronics industry, where size scales have been greatly reduced over the past few decades. These two examples give an idea of the many reasons why processes for developing nanostructured materials are of interest.

Nanostructured materials can be generally grouped into four categories. There are: 1) zero-dimensional structures, i.e., quantum dots; 2) one-dimensional structures, i.e., nanorods and nanowires; 3) two-dimensional structures: thin films; and 4) three-dimensional structures: bulk materials with nanoscale building blocks. Although all of these categories have a large variety of potentially interesting properties and applications, it would be difficult to explore more than one of them in any depth. Thus, this research has focused on one-dimensional (1D) nanostructures.

1D nanostructures can show behaviors that are characteristic of both the nanoscale and bulk forms of the material. For example, Ag nanowires show optical responses that are size-specific along their radius, but are like the bulk behavior along

their length[1]. There are a number of interesting properties and potential applications for 1D nanostructures. One-dimensional nanostructures can have mechanical properties far superior to the bulk, in part because they contain fewer defects[2], and nanowires have been shown to exhibit single-electron conduction[3]. Individual nanowires have been used as novel probes for atomic force microscopes (AFM)[4]. One can also imagine an ordered array of nanorods being used to form a 2D photonic bandgap structure, as it would be the inverse of the arrays of pores in alumina that have already been demonstrated as photonic materials[5]. These, along with numerous other applications, have made oxide nanorod synthesis an active area of research over the past few years[6].

1.2 Synthesis of 1D nanostructured oxides.

One-dimensional nanostructures have been called by a variety of names including whiskers, fibers or fibrils, nanowires, and nanorods. Often, nanotubes and nanocables are also considered as one-dimensional structures. Although whiskers and nanorods are in general considered shorter than fibers and nanowires, the definition is often a little arbitrary. In addition, one-dimensional structures with diameters ranging from several nanometers to several hundred microns were referred to as whiskers and fibers in the early literature, whereas nanowires and nanorods with diameters less than a few hundred nanometers are used predominantly in the recent literature. In this chapter, various terms of one-dimensional structures will be used interchangeably, though nanowires in general have a higher aspect ratio than that of nanorods.

Many techniques have been developed in the synthesis and formation of one-dimensional nanostructured materials, though some techniques have been explored extensively; others have attracted less attention. These techniques can be generally grouped into four categories (with associated sub-categories):

1. Spontaneous growth:
   a. Evaporation (or dissolution) – condensation
   b. Vapor – liquid – solid (VLS) growth
2. Lithography

3. Electrospinning / fiber drawing
4. Template-based synthesis:
    a. Colloidal dispersion, melt, or solution filling
    b. Electrodeposition
    c. Conversion through chemical reactions (consumable templates)
    d. Electrophoretic deposition

Spontaneous growth commonly results in the formation of single crystal nanowires or nanorods along a preferential crystal growth direction depending on the crystal structures and surface properties of the nanowire materials. Template-based synthesis can produce single crystalline, polycrystalline or even amorphous products. All the above techniques for the preparation of one-dimensional nanostructured materials will be discussed in this chapter.

1.2.1 Spontaneous growth

Spontaneous growth is a process driven by the reduction of free energy, often through phase transformations, chemical reactions or the release of stress. Anisotropic growth is required for the formation of nanowires or nanorods. That is, the crystal must grow faster along a specific orientation than in other directions. Uniformly sized nanowires can be obtained when the crystal growth proceeds along only one direction, with no growth along other directions. In some systems, the anisotropic growth may not be inherent in the system, but because of some sort of confinement, or poisoning of the growth of specific crystal directions. In spontaneous growth, for a given material and set of growth conditions, defects and impurities on the growth surfaces can play a significant role in determining the morphology of the final products.

1.2.1.1 Evaporation (dissolution) – condensation

The evaporation-condensation process is also referred to as the vapor-solid (VS) process; however, the discussion in this section will not be limited only to simple evaporation-condensation process. Chemical reactions among various precursors may be involved to produce the desired materials. The growth of nanorods from solution (by

dissolution-condensation) is also included. The driving force for the synthesis of nanorods by spontaneous growth is a decrease in Gibbs free energy, which arises from either re-crystallization or a decrease in supersaturation. Nanorods grown by evaporation-condensation methods are commonly single crystals with a small number of imperfections, and their formation is through anisotropic growth.

For the vapor solid growth, there have been three main techniques reported for the formation of oxide nanostructures. The difference in these methods is the material used for the evaporation, which can be a metal oxide, metal, or a precursor that contains the desired metal to be oxidized.

The simplest VS method involves directly heating the metal oxide under appropriate conditions. Using this technique, a wide variety of metal oxide 1D nanostructures have been synthesized. Examples include belt-like structures of ZnO, SnO_2, In_2O_3 and CdO[7,8], nanorods of YBCO[9] and both nanowires and nanobelts of Ga_2O_3[10]. The ease of the VS method is seen in work done by Pan et al[7,8], who reported the growth of single crystal nanobelts of various semiconducting oxides. For instance, nanobelts of ZnO were formed by heating ZnO powder in an alumina tube furnace to 1400 °C for 2 hours under a low-pressure (300 torr) Ar flow. ZnO vapor is carried downstream by the Ar flow, and ZnO nanobelts are collected on an alumina plate at the downstream end of the tube. Figure 1-1 shows TEM micrographs of some of these ZnO nanobelts.

Heating of metals can also lead to the formation of oxide nanowires. The process can be as simple as heating of a Cu grid in air to form CuO nanowires on the surface[11]. Although an intentionally oxidizing atmosphere can be used, for example to make In_2O_3[12] or Fe_2O_3[13] nanowires, it is sometimes unnecessary. Several groups have reported growth of oxide nanowires such as WO_x[14] and GeO_2[15] by simply heating the metals in Ar. It is assumed that a sufficient amount of oxygen either leaks into the system or is present in the carrier gas to cause the oxidation reaction to occur.

Such an oxygen leakage/contamination is likely also responsible for oxide growth when certain precursors are decomposed. Yin et al found that heating MgB_2 to 800-900 °C in Ar caused the formation of MgO nanowires on a substrate above the

powders[16]. A similar report has demonstrated the growth of ZrO_2 nanorods within BN nanotubes by heating ZrB_2 in an N_2/NH_3 mixture[17].

Other precursors have been intentionally decomposed in O_2, as in metal-organic vapor phase epitaxy (MOVPE). Park et al have created single crystal ZnO nanorods on single crystal sapphire substrates from diethyl zinc and O_2 in an Ar carrier[18]. Similarly, Wu et al formed TiO_2 nanorods from titanium acetylacetonate ($Ti(C_{10}H_{14}O_5)$[19].

Dissolution – condensation process differs from evaporation – condensation in growth media. In dissolution - condensation process, the growth species first dissolve into a solvent, and then diffuse to and deposit on the growth surface resulting, in the formation of nanorods or nanowires. This general concept can be applied in a number

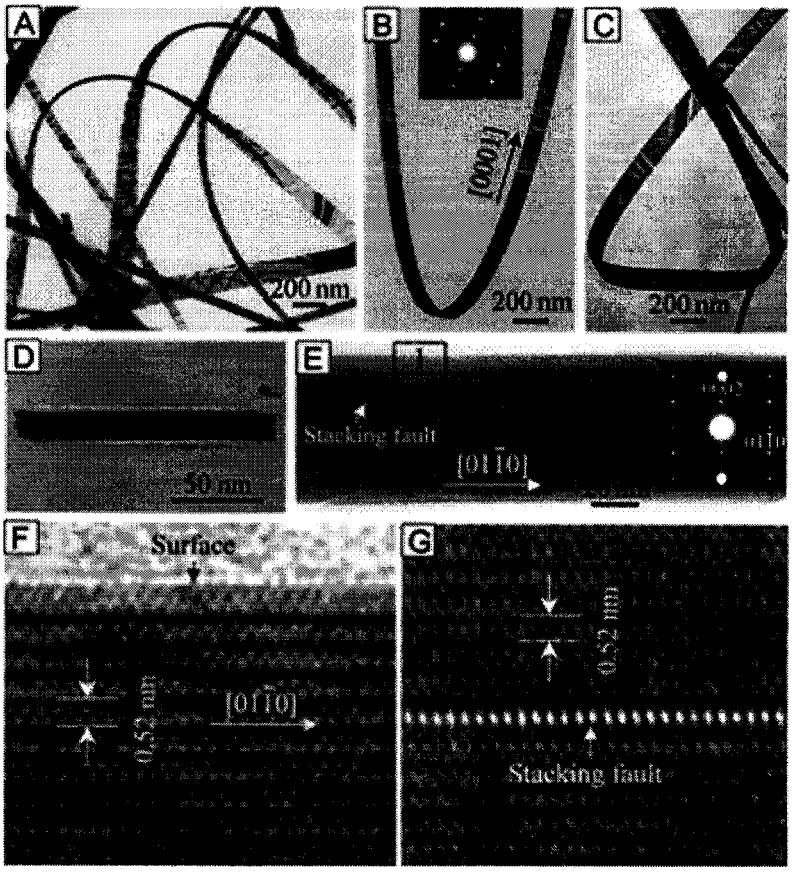

Figure 1-1 ZnO nanobelts grown by evaporation-condensation. These TEM images show the rectangular cross section, high crystallinity and lack of an oxide sheath on these nanobelts.

of ways for the growth of oxide nanorods. In the simplest methods, the desired material is simply precipitated out of a solution. α-Fe_2O_3 nanorods have been grown by reacting aqueous $FeCl_3$ and $NaNO_3$ at a pH of 1.5, then evaporating the water to precipitate nanorods of β-FeOOH, which transform to Fe_2O_3 upon heating to about 390 °C[20]. An SEM micrograph of these rods is shown in Figure 1-2. Similar methods have been used to create nanorods of α-FeOOH[21] and long nanoscale fibers of V_2O_5[22].

Solution processing can grow nanowires on alien crystal nanoparticles, which serve as seeds for heteroepitaxial growth. Dissolution – condensation processes can also grow nanowires on a substrate. Govender et al formed ZnO nanorods on glass substrates from a solution of zinc acetate or zinc formate and hexamethylenetetramine at room temperature[23]. These faceted nanorods were preferentially oriented in the [0001] direction (that is, along the c-axis), with diameters of about 266 nm and a length of ~3 μm. Others have formed helical nanorods of ZnO on ZnO crystalline seeds[24].

Some oxide materials do not spontaneously form into 1D nanostructures. To assist in the formation of nanorods, researchers have applied sonication[25,26] and reaction inside cylindrical inverse micelles[27,28,29]. Others have used surfactant additives to control the shape of their products. For example, Guo et al have used polyvinylpyrrolidone (PVP) to form ZnO nanorods with an aspect ration of ~4 from a solution that produces spherical ZnO colloids when the PVP is omitted[30]. Similarly,

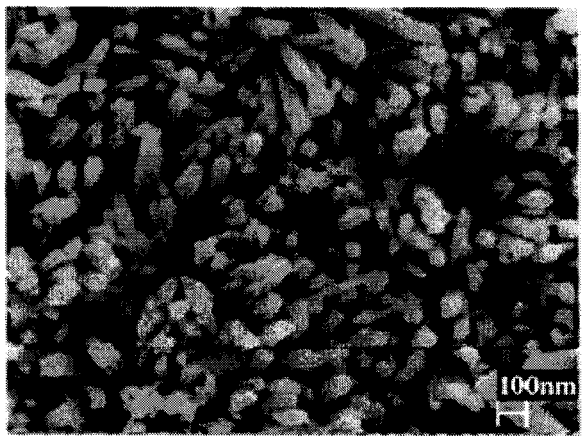

Figure 1-2 Fe_2O_3 nanorods from a solution growth technique. These ~50 nm bundles contain nanorods ~5nm in diameter, and are up to ~ 1μm in length

polyethyleneglycol (PEG) has been used in the formation of Cu_2O nanorods by reduction of $Cu(OH)_2$ with hydrazine (N_2H_4)[31]. Such additives may work by preferentially adsorbing to certain crystal facets, restricting the growth to specific directions, as has been reported for the growth of Ag nanowires in the presence of PVP[1].

For some oxide systems, higher growth temperatures are required than can be obtained in a normal aqueous solution. One method to overcome this is the use of hydrothermal growth. $CdWO_4$ nanorods were directly synthesized by reacting $CdCl_2$ and $NaWO_4$ at 130 °C under pressure, at a pH ranging from 3 to 11, for 5 hours[32]. Hollow nanotubes of $H_2Ti_3O_7$ have been hydrothermally synthesized from TiO_2 powder dissolved in a NaOH aqueous solution at 130 °C[33]. Other hydrothermally synthesized nanorods include α-MnO_2[34,35], β-MnO_2[35], ZnO[36], MoO_3[37], V_2O_5[38], $Li_xV_{2-\delta}O_{4-\delta}\cdot H_2O$[39] and (La,Ba)$MnO_3$[40], all at temperatures in the range of 120-270 °C. Epitaxial agglomeration of two nanoscale crystalline particles under hydrothermal conditions has also been reported to form small, low aspect ratio nanorods of TiO_2[41] and ZnO[42].

Another way to work at elevated temperatures is to use a molten salt flux as the liquid phase. Wang et al have developed a method of decomposing precursors (either metal carbonates or metal oxalates) formed in an inverse microemulsion by heating in a molten salt (usually NaCl) flux to form metal oxide nanowires. For example, Mn_3O_4 nanorods were synthesized by first grinding together $MnCl_2$ and Na_2CO_3 to form a precursor powder. This precursor was then mixed with NaCl and a surfactant (nonylphenyl ether) and heated to 850 °C for 2 hrs. After cooling, the NaCl flux was washed away with DI water, leaving the Mn_3O_4[43] nanorods. Numerous metal oxides have been synthesized in the manner, including Co_3O_4[44], CdO[45] and SnO_2[46] among many others.

1.2.1.2 Vapor–liquid–solid (VLS) growth

In VLS growth, a second material (catalyst) is purposely introduced to direct and confine the crystal growth within a specific area. Typically, the catalyst forms a liquid droplet either by itself or by alloying with the growth material during the growth. This liquid drop acts to trap the growth species. As the concentration of growth species in the

catalyst droplet becomes supersaturated, the material precipitates out from the droplet at the growth surface, resulting in the one-directional growth. Wagner et al[47,48] first proposed the VLS theory over 40 years ago to explain the experimental results in the growth of silicon whiskers, which was inexplicable by the evaporation – condensation theory. The seven requirements for VLS growth that were laid out over 30 years ago sum up all that is needed for VLS growth[49]:

1. The catalyst or impurity must form a liquid solution with the crystalline material to be grown at the deposition temperature,
2. The distribution coefficient of the catalyst or impurity must be less than unity at the deposition temperature.
3. The equilibrium vapor pressure of the catalyst or impurity over the liquid droplet must be very small. Although the evaporation of the catalyst does not change the composition of the saturated liquid composition, it does reduce the total volume of the liquid droplet. Unless more catalyst is supplied, the volume of the liquid droplet reduces. Consequently, the diameter of the nanowire will reduce and the growth will eventually stop, when all the catalyst is evaporated.
4. The catalyst or impurity must be chemically inert. It must not react with the chemical species such as the by-products present in the growth chamber.
5. The interfacial energy plays an important role. The wetting characteristics influence the diameter of the grown nanowire. For a given volume of liquid droplet, a small wetting angle results in a large growth area, leading to a large diameter of nanowires.
6. For growth of compound nanowires, one of the constituents can serve as the catalyst.
7. For controlled unidirectional growth, the solid-liquid interface must be well defined crystallographically. One of the simplest methods is to choose a single crystal substrate with the desired crystal orientation.

In VLS growth, vapor phase growth species diffuse to and dissolve in the liquid catalyst droplet. This liquid droplet is often supported on some type of a substrate, which may be the same materials as the grown nanowires. When the concentration of growth species dissolved in the droplet becomes saturated, those species will diffuse to and precipitate out at the interface between the liquid and the underlying substrate. The precipitation will follow first nucleation and then crystal growth. Continued precipitation separates the substrate and the liquid droplet, resulting in the growth of nanowires. The nanowires can be single crystal, polycrystalline or amorphous depending on the substrates and growth conditions. It is noted that the diameter of the nanowire may change if the growth conditions vary, or if the catalyst evaporates or is incorporated into the nanowires. Figure 1-3 illustrates the steps of VLS growth.

The catalyst can be introduced in situ as well. Here, the growth precursor is mixed with the catalyst and evaporated simultaneously at a higher temperature. Both the growth precursor or species and the catalyst condense at the substrate surface when a supersaturation is reached at a temperature lower than the evaporation temperature. The mixture of the growth species and catalyst react either in the vapor phase or on the substrate surface to form a liquid droplet. The subsequent nanowire growth then proceeds as discussed above.

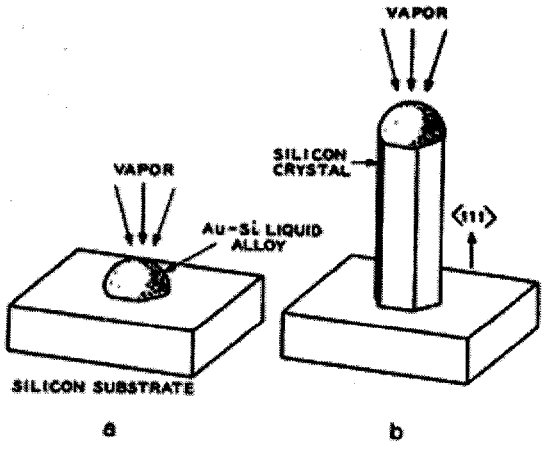

Figure 1-3 VLS growth mechanism. In part a, a vapor Si source dissolves in the catalyst droplet, precipitating out a Si nanowire in part b.

Despite the (seemingly restrictive) requirement of a eutectic oxide-catalyst system for the VLS growth of oxide nanorods, a number of materials have been synthesized with this method. Examples include ZnO[50], amorphous silica[51], Ga_2O_3[52], In_2O_3[53], and MgO[54]. ZnO nanowire growth is discussed as an example.

ZnO nanowires have been grown using the VLS method on Au-coated (thickness ranging from 2 to 50 nm) silicon substrates by heating a 1:1 mixture of ZnO and graphite powder to 900 –925 °C under a constant flow of argon for 5-30 min[50]. The grown ZnO nanowires vary with the thickness of the initial Au coatings. For a 50 nm Au coating, the diameters of the nanowires normally range from 80 to 120 nm and their lengths are 10-20 μm. Thinner nanowires of 40-70 nm with lengths of 5-10 μm were grown on 3 nm Au-coated substrates. The grown ZnO nanowires are single crystal with a preferential growth direction of <001>. Examples of these VLS-grown ZnO nanowires are shown in Figure 1-4. The growth process of ZnO is believed to be different from that of elementary nanowires. The process involves the reduction of ZnO by graphite to form Zn and CO vapor at high temperatures (above 900 °C). The Zn vapor is transported to and reacted with the Au catalyst, which would have already reacted with silicon to form a eutectic Au-Si liquid on silicon substrates, located downstream at a lower temperature to form Zu-Au-Si alloy droplets. As the droplets become supersaturated with Zn, crystalline ZnO nanowires are formed, possibly through the reaction between Zn and CO at a lower temperature. The above process can be

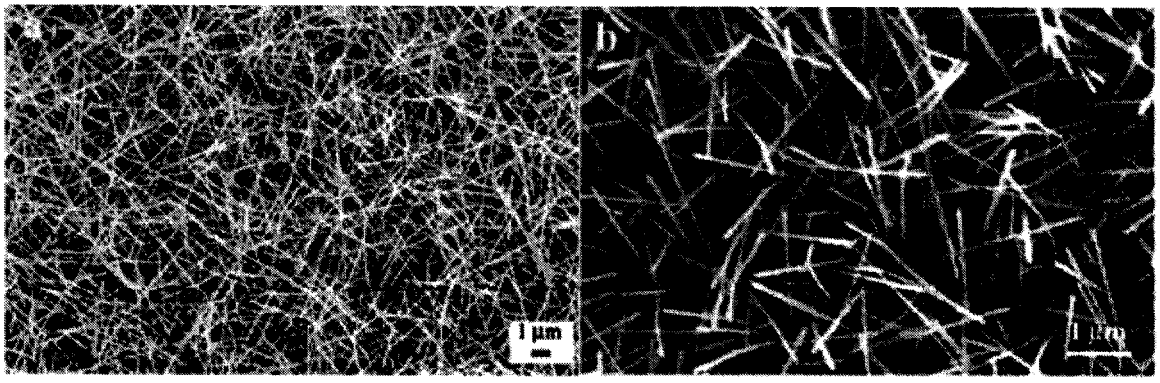

Figure 1-4 ZnO nanowires by VLS growth. The nanorods were grown on a substrate with either ~50Å (A) or ~30Å (B) thick Au film for the catalyst.

easily understood because the reaction:

$$ZnO + C \leftrightarrow Zn + CO \qquad \text{Reaction 1-1}$$

is reversible at temperatures around 900 °C[55]. Although the presence of a small amount of CO is not expected to change the phase diagram significantly, no ZnO nanowires were grown on substrates in the absence of graphite.

In some systems, it is possible for one of the components of the desired system to act as a catalyst for VLS growth. For example, Sn-doped In_2O_3 (ITO) nanorods have been synthesized by VLS growth[56]. Here a mixture of In and Sn metal powders were heated to 900 °C under a flow of Ar and O_2 gasses. At the growth temperature, there is a co-existence of both In_2O_3, and a Sn-rich liquid. When the concentration of In_2O_3 in the liquid droplet becomes supersaturated, In_2O_3 nanowires begin to precipitate out from the drop. Since there is a moderate solubility of Sn in In_2O_3, the grown nanorods are actually ITO, with a Sn content close to that of the starting powder mixture.

1.2.1.3 Solution–liquid–solid (SLS) growth

Similar to the VLS technique, SLS growth also relies on the formation of a supersaturated alloy liquid droplet. However, in this case the precursors are provided through a liquid phase, rather than vapor. Typically, these precursors are organometallic compounds dissolved in hot organic solvents. So far, this method has been widely applied to Si[57], Ge[57,58], III-V (such as InAs[59]) and II-VI semiconductor nanorods, and more complicated materials (such as $CuInS_2$[60]) but as yet has not been used to synthesize oxides.

1.2.2 Lithography

Lithography represents another route to the synthesis of nanowires. Various techniques have been explored in the fabrication of nanowires, such as electron beam

lithography[61,62], ion beam lithography[63], scanning tunnel microscope (STM) lithography, X-ray lithography, proximal-probe lithography and near-field photolithography[64]. The basic idea behind these techniques is that an incident energy source (light, electrons, ions, etc.) is directed to a specific location on a substrate, whereby some localized change occurs. Possible changes include the crosslinking of a polymer (negative resist), the damaging of a polymer (positive resist), or even the direct oxidation of the surface. Nanowires with diameters less than 10 nm and an aspect ratio of 100 can be readily prepared.

1.2.3 Electrospinning

The electrospinning process involves the application of very high electric fields to a liquid in a capillary. Above a certain threshold field, the liquid is ejected from the capillary in a continuous stream. This occurs because the nonconductive liquid builds up a large static charge, of the same sign as the charge on the nozzle. This electrostatic repulsion becomes sufficient to overcome the surface tension of the liquid, ejecting it out from the nozzle as a thin jet. If the liquid is a polymer solution, for example, evaporation of solvent from the expelled jet yields a polymeric nanofiber. Similarly, if the liquid contains both a polymer and the precursors for an oxide material (such as alkoxides), it is possible to spin composite nanofibers of polymer/amorphous oxide. Thermal treatments burn off the polymer and crystallize the oxide, yielding an oxide nanofiber. This technique has been applied to a variety of simple and complex oxides, such as TiO_2[65], V_2O_5[66], Nb_2O_5[67] and $NiFe_2O_4$[68]. An alternative method uses sol-gel processing to form a liquid of the desired viscosity, which is then electrospun and calcined into an oxide nanofiber, as has been seen in $Pb(Zr,Ti)O_3$[69].

1.2.4 Template-based synthesis

Template-based synthesis of nanostructured materials is a general method that can be used in fabrication of nanorods, nanowires and nanotubes of polymers, metals, semiconductors and oxides. Various templates with nanosize channels have been

explored for the template growth of nanorods and nanotubes. The most commonly used and commercially available templates are anodized alumina membranes (AAM)[70] and radiation track-etched polymer (particularly polycarbonate, PC) membranes[71]. Other membranes have also used as templates such as nanochannel array glass[72], radiation track-etched mica[73], porous silicon by electrochemical etching of silicon wafer[74], mesoporous materials[75], zeolites[76], carbon nanotubes[77], step edges on graphite[78], and liquid crystal phases[79].

In addition to the desired pore or channel size, morphology, size distribution and density of pores, template materials must meet certain requirements. First, the template materials must be compatible with the processing conditions. For example, an electrical insulator is required for a template to be used in electrochemical deposition. Except for the template directed synthesis, template materials should be chemically and thermally inert during the synthesis and following processing steps. Secondly, the deposition material/solution must wet the internal pore walls. Thirdly, for the synthesis of nanorods or nanowires, it is preferred that deposition starts from one end of the template channels, proceeding through the template from one side to the other. In contrast, for the growth of nanotubes the deposition should start from the pore wall and proceed inwardly. Inward growth may result in the pore blockage, so that should be avoided in the growth of "solid" nanorods or nanowires. Kinetically, enough surface relaxation permits maximal packing density, so a diffusion-limited process is preferred. Other considerations include the ease of release of nanorods from the templates and ease of handling during the experiments.

1.2.4.1 Colloid dispersion, melt, or solution filling

Direct template filling is the most straightforward and versatile method in preparation of nanorods and nanotubes. In general, either a melt or a liquid precursor is used to fill the pores. There are several concerns in the template filling. First, the wetability of the pore wall should be good enough to permit the penetration and complete filling of the liquid precursor or precursor mixture. For filling at low temperatures, the surface of pore walls can be easily modified to be either hydrophilic or

hydrophobic by introducing a monolayer of organic molecules. Second, the template materials should be chemically inert. Thirdly, control of shrinkage during solidification is required.

A number of factors can lead to the formation of either nanorods or hollow nanotubes. Nanorods may form when adhesion between the pore walls and the filling material is weak. Another possibility is that solidification may start at the center of the pores and continues radially outward, if there is electrostatic repulsion between the growth species and the pore walls. If homogeneous nucleation is favored over heterogeneous nucleation, solid rods will be formed. Or, when solidification proceeds from one end of the pore to the other rods are formed. If the adhesion is very strong, the solidification starts at the interfaces and proceeds inwardly, or heterogeneous nucleation occurs preferentially, then hollow nanotubes are more likely.

Martin and his co-workers[80,81] have studied the formation of various oxide nanorods and nanotubes by simply filling the templates with colloidal dispersions. Colloidal dispersions were prepared using appropriate sol-gel processing. The filling of the template was accomplished by placing a template in the sol for a given time. Capillary force is believed to drive the sol into the pores. After the pores were filled with sol, the template was withdrawn from the sol and dried prior to firing at elevated temperatures. For example, TiO_2 nanorods were made by dissolving titanium isopropoxide in ethanol, and mixing with a solution of HCl in ethanol. Anodic alumina templates were dipped into this room temperature sol for a given time, and then the filled template was fired at 400 °C for 24 hrs. The results were TiO_2 nanorods of ~50 μm length and 200 nm diameter[81]. SEM micrographs of such rods are shown in Figure 1-5.

The typical sol consists of a large volume fraction of solvent up to 90% or higher[82]. Although the capillary force may ensure the complete filling of colloidal dispersion inside pores of the template, the amount of the solid filled inside the pores can be small. In fact, many groups have found that hollow rods are synthesized by sol filling[83,84,85] (see Figure 1-5). There are two possible explanations for such hollow structures. One is the diffusion of solvent through the membrane, leading to the

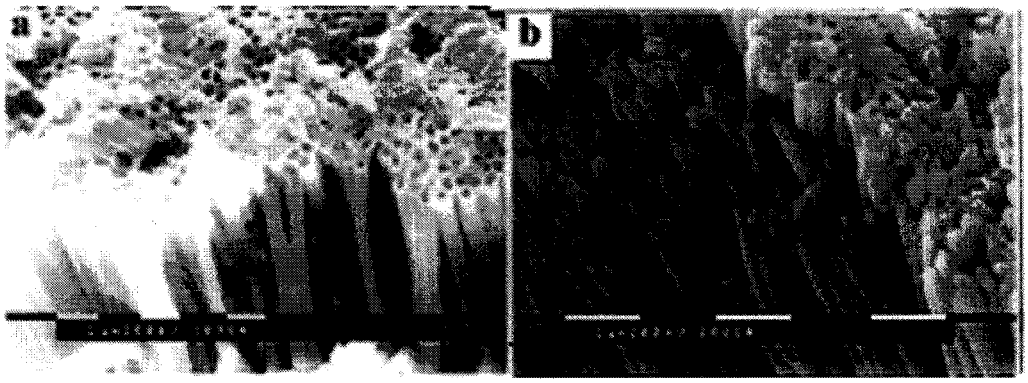

Figure 1-5 Hollow (a) and solid (b) nanorods of TiO_2 by sol filling. AAM templates were immersed in a TiO_2 sol for varying amounts of time.

enrichment of solid along the internal surface of template pores, a process used in ceramic slip casting[86]. For this mechanism to work, however, would require a very rapid diffusion of solvent through the template, considering that the templates typically were emerged into sol for just a few minutes. Another explanation is electrostatic attraction between oppositely charged sol nanoparticles and pore walls.

Hollow nanostructures do not always result, however. For example, Lakshmi et al. found that TiO_2 nanorods synthesized in this manner had the same diameter as the template pores, even after heating to 400 °C[80]. Although this is a low temperature compared to that which is generally used to sinter TiO_2, some shrinkage is still expected. This result indicates that there is some mechanism to enrich the concentration of solid inside the pores. Given that longer immersion times were found to yield solid rather than hollow rods[81], it could be that the growth is proceeding from the walls inward, with the same electrostatic attraction or slip-casting behavior further enriching the solid inside the template. It is likely that a complex interplay between sol concentration, particle charge and pore wall charge controls the morphology of the final nanorod.

This filling technique is a versatile method for synthesizing nanorods, and can be applied for any material that can be made by sol-gel processing. The drawback, however, is the difficulty of ensuring complete filling of the template pores. It is also noticed that the nanorods made by template filling are commonly polycrystalline or amorphous. An exception was found, however, when the diameter of nanorods is

smaller than 20 nm, single crystal TiO_2 nanorods were made[80]. Additionally, some larger TiO_2 nanorods show a large degree of preferential (101) orientation[87].

Some groups have reported the synthesis of more complex oxide nanowires through sol-gel template methods. Examples include polycrystalline $LiNi_{0.5}Co_{0.5}O_2$[88] and $La_{1-x}Ca_xMnO_3$[89] and related materials formed in AAM templates.

Because of the high melting temperatures of many oxides, it can be difficult to form nanorods by filling of a template directly with the molten oxide. It requires templates that are both stable and non-reactive at the elevated temperatures used. One material that has been found suitable for such applications is carbon nanotubes (CNTs). Several oxides with low melting temperatures, such as PbO[90], Bi_2O_3[91], V_2O_5[92] and MoO_3[93] have been filled into open CNTs to form oxide nanorods. This simple requires the oxidation of CNTs (typically with nitric acid) to open them, followed by mixing the CNTs with the molten metal. Because of the very low surface tensions of these molten oxides, they strongly wet the CNT, and are drawn in by capillary action. It is conceivable that nanorods of metals with multiple oxidation states could be formed in such a way, and then converted to a different oxidation state. For example, nanorods of MoO_2 can be synthesized by reducing MoO_3 synthesized in CNTs[93].

Solution filling of templates has also found limited application as a method for synthesizing oxide nanorods. In one example, solutions of RuO_4 dissolved in pentane have been filled into mesoporous silica templates, yielding nanowires of RuO_2 after cryogenic decomposition of the RuO_4[94]. Similarly, TiO_2 nanotubes and nanorods have been made by filling anodic alumina templates with solutions that precipitate TiO_2[95] or pyrolyze to TiO_2[96].

1.2.4.2 Electrodeposition

Electrodeposition is an electrochemical reaction that results in the deposition of solid material on an electrode. When deposition is confined inside the pores of template membranes, nanocomposites are produced. If the template membrane is removed, nanorods or nanowires are prepared. In general, electrochemical deposition is only applicable to electrical conductive materials such as metals, alloys, semiconductors and

electrical conductive polymers, since after the initial deposition, electrode is separated from the depositing solution by the deposit and the electrical current must go through the deposit to allow the deposition process to continue. Thus, most of the nanomaterials produced by template electrodeposition have not been oxides (mostly metals, chalcogenide semiconductors and conducting polymers). Nanostructures of a few semiconducting oxides, however, have been formed through conventional or novel electrochemical processes.

TiO_2 is a wide band-gap semiconductor with a high enough conductivity that it can be electrodeposited under certain conditions. For instance, the technique described by Kavan et al[97] for the electrodeposition of TiO_2 films from $TiCl_3$ solutions has been adapted to synthesize both polycrystalline[98] and single crystal[99] TiO_2 nanowires. The reaction consists of two parts. First, ionic species are generated:

$$Ti^{3+}_{(aq)} + H_2O \leftrightarrow TiOH^{2+} + H^+ \qquad \text{Reaction 1-2}$$

This species is then electrochemically oxidized to form TiO_2[97].

A similar technique was used by Miao et al to prepare single crystal TiO_2 nanowires, in a process they called template-based electrochemically induced sol-gel deposition[100]. Titania electrolyte solution was prepared using a method developed by Natarajan and Nogami[101], in which Ti powder was dissolved into a H_2O_2 and NH_4OH aqueous solution, forming TiO^{2+} ionic clusters. When an external electric field was applied, TiO^{2+} ionic clusters diffused to the cathode and underwent hydrolysis and condensation reactions, resulting in deposition of nanorods of amorphous TiO_2 gel. After heat treatment (240 °C for 24 hr in air), nanowires of single crystal TiO_2 with anatase structure and with diameters of 10, 20, and 40 nm and lengths ranging from 2 to 10 μm were synthesized.

Polycrystalline ZnO nanowires have been electrodeposited in AAM templates from aqueous $Zn(NO_3)_2$ solutions[102]. Cu_2O has been electrodeposited into several templates, such as track-etched polycarbonate[103] and surfactant liquid-crystal phases[104].

1.2.4.3 Converting through chemical reactions

Nanorods or nanowires can also be synthesized using consumable templates or template-directed reactions. For instance, GeO_2 nanorods have been synthesized by reacting Ge metal and carbon nanotubes in the presence of O_2 (introduced either as gas, or from the in-situ reduction of SiO_2)[105]. By coating carbon nanotubes with an appropriate metal oxide precursor (such as an alkoxide) and heating in air, Satishkumar et al have synthesized a number of oxide nanorods and nanotubes, such as SiO_2, Al_2O_3, V_2O_5, WO_3, MoO_3, MoO_2, Sb_2O_5, RuO_2 and IrO_2[106,107]. Similarly, $Co(NO_3)_2$ coatings on CNTs have been decomposed by heating under Ar to from Co_3O_4 nanorods[108].

Another example of conversion is the oxidation of metallic nanorods to form oxide nanorods. This technique is applicable to the formation of any single-metal oxide where the starting metal can be electrochemically deposited in a template (such as CdO[109], SnO_2[110], In_2O_3[111], SnO_2[112] and ZnO[113]) or otherwise formed into the desired shape (such as RuO_2 formed by oxidizing thin films of Ru coated on carbon nanotubes[114]). For example, ZnO nanowires were prepared in the following manner. In the first step, polycrystalline zinc nanowires without preferential crystal orientation were prepared by electrodeposition using anodic alumina membrane as a template, and in the second step, grown zinc nanowires were oxidized at 300 °C for up to 35 hr. in air, yielding polycrystalline ZnO nanowires with diameters ranging from 15 to 90 nm and length of ~ 50 μm. Although ZnO nanowires are embedded in the anodic alumina membranes, freestanding nanowires may be obtained by selectively dissolving alumina templates.

1.3 Electrophoretic deposition

The electrophoretic deposition technique has been widely explored, particularly in film deposition of ceramic and organoceramic materials from colloidal dispersions[115]. Electrophoretic deposition differs from electrochemical deposition in several aspects. First, the material deposited by electrophoretic deposition may be electrically insulating. Therefore, this method is particularly useful for oxide systems. Secondly, nanosized

particles in colloidal dispersions are typically stabilized by electrostatic or electrosteric mechanisms. When dispersed in a polar solvent or an electrolyte solution, the surface of nanoparticles develops an electrical charge via one or more of the following mechanisms: (1) preferential dissolution or (2) deposition of charges or charged species, (3) preferential reduction or (4) oxidation, and (5) adsorption of charged species such as polymers. Charged surfaces will electrostatically attract oppositely charged species (typically called counter-ions) in the solvent or solution. A combination of electrostatic forces, Brownian motion and osmotic forces results in the formation of the double layer structure, schematically illustrated in Figure 1-6. The figure depicts a positively charged particle surface, the concentration profiles of negative ions (counter-ions) and positive ions (surface-charge-determining ions) and the electric potential profile. The concentration of counter-ions gradually decreases with distance from the particle surface, whereas that of charge-determining ions increases. As a result, the electric potential decreases with distance. Near to the particle surface, the electric potential

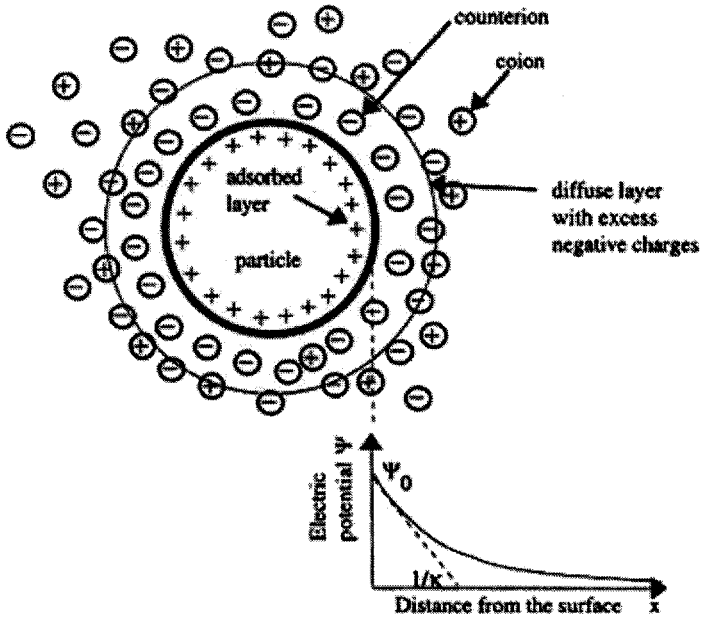

Figure 1-6 A schematic of the electrical double layer surrounding a particle in a colloidal suspension. This double layer is responsible for the electrostatic stabilization of a colloid

decreases linearly, in the region known as the Stern layer. Outside of the Stern layer, the decrease follows an exponential relationship, and the region between Stern layer and the point where the electric potential equals zero is called the diffusion layer. Together, the Stern layer and diffusion layer are called the double layer structure in the classic theory of electrostatic stabilization.

Upon application of an external electric field to a colloid or sol, the constituent charged particles are set in motion in response to the electric field, as schematically illustrated in Figure 1-7. This type of motion is referred to as electrophoresis. When a charged particle is in motion, some of the solvent or solution surrounding the particle will move with it, since part of the solvent or solution is tightly bound to the particle. The plane that separates the tightly bound liquid layer from the rest of the liquid is called the slip plane. The electric potential at the slip plane is known as the zeta-potential. Zeta-potential is an important parameter in determining the stability of a colloidal dispersion or a sol; a zeta potential larger than about 25 mV is typically required to stabilize a colloid[116].

Zeta potential is determined by a number of factors, such as the particle surface charge density, the concentration of counter-ions in the solution, solvent polarity and temperature. The zeta potential around a spherical particle can be described as[117]:

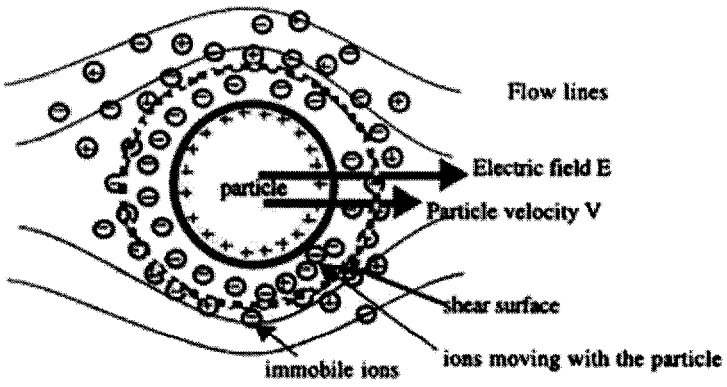

Figure 1-7 Diagram of the features of electrophoretic motion.

$$\zeta = \frac{Q}{4\pi\varepsilon_r a(1+\kappa a)} \qquad \textbf{Equation 1-1}$$

with

$$\kappa = \left(\frac{e^2 \sum n_i z_i^2}{\varepsilon_r \varepsilon_0 kT} \right)^{1/2} \qquad \textbf{Equation 1-2}$$

where Q is the charge on the particle, a is the radius of the particle out to the shear plane, ε_r is the relative dielectric constant of the medium, a is the size of the nanoparticle, and n_i and z_i are the bulk concentration and valence of the i^{th} ion in the system, respectively. It is worth while to note that a positively charged surface results in a positive zeta potential in a dilute system. A high concentration of counter ions, however, can result in a zeta-potential of the opposite sign.

The mobility of a nanoparticle in a colloidal dispersion or a sol is dependent on the dielectric constant of the liquid medium, the zeta potential of the nanoparticle, and the viscosity of the fluid. Several forms for this relationship have been proposed, such as the Hückel equation[117]:

$$\mu = \frac{2\varepsilon_r \varepsilon_0 \zeta}{3\pi\eta} \qquad \textbf{Equation 1-3}$$

Electrophoretic deposition simply uses such an oriented motion of charged particles (shown in Figure 1-7) to grow films or monoliths by enriching the solid particles from a colloidal dispersion or a sol onto the surface of an electrode. If particles are positively charged (more precisely speaking, having a positive zeta potential), then the deposition of solid particles will occur at the cathode. Otherwise, deposition will be at the anode. At the electrodes, surface electrochemical reactions proceed to generate or receive electrons. The electrostatic double layers collapse upon deposition on the growth surface, and the particles coagulate. Relatively strong attractive forces, including the formation of chemical bonds between two particles, develop once the particles coagulate. The films or monoliths grown by electrophoretic deposition from colloidal

dispersions or sols are essentially a compaction of nanosized particles. Such films or monoliths are porous, i.e., there are voids inside. Typical packing densities, defined as the fraction of solid (also called green density) are less than 74%, which is the highest packing density for uniformly sized spherical particles[118]. The green density of films or monoliths by electrophoretic deposition is strongly dependent on the concentration of particles in sols or colloidal dispersions, zeta-potential, externally applied electric field and reaction kinetics between particle surfaces. Slow reaction and slow arrival of nanoparticles onto the surface would allow sufficient particle relaxation on the deposition surface, so that a high packing density is expected.

This electrophoretic motion can be used to fill the pores of a template in order to synthesize nanorods. Figure 1-8 shows a schematic of the growth of such nanorods as a function of time. Initially, positively charged sol particles are moving electrophoreticly towards the negative electrode, depositing at the bottom of the pore, while the negatively charged counter ions are moving in the opposite direction. With further deposition, the densely packed sol particles fill up more of the pore. Given enough time, the pores eventually become completely filled, yielding the desired oxide nanorods.

Many theories have been proposed to explain the processes at the deposition surface during electrophoretic deposition. Electrochemical processes at the deposition surface or electrodes are complex and vary from system to system. In general, however, a current exists during electrophoretic deposition, indicating reduction and oxidation reactions occur at electrodes and/or deposition surface. Many films or monoliths grown by electrophoretic deposition are electric insulators; however, the films or monoliths are porous and the surface of the pores would be electrically charged just like the nanoparticle surfaces, since surface charge is dependent on the solid material and the solution. Furthermore, the pores are filled with solvent or solution that contains counter-ions and charge-determining ions. The electrical conduction between the growth surface and the bottom electrode could proceed via either surface conduction or solution conduction.

Wang et al used electrophoretic deposition to from nanorods of ZnO from colloidal sols[119]. ZnO colloidal sol was prepared by hydrolyzing an alcoholic solution of zinc acetate with NaOH, with a small amount of zinc nitrate added to act as a binder. This solution was then deposited into the pores of anodic alumina membranes at

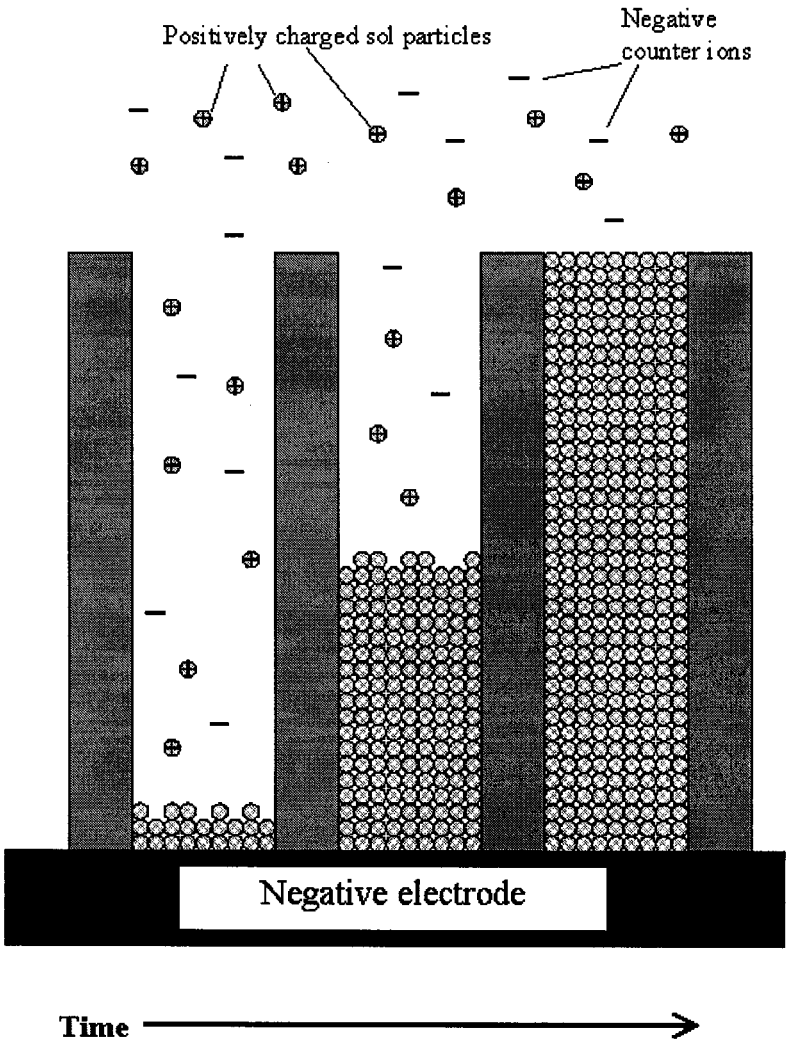

Figure 1-8 This schematic demonstrates the progression of nanorod growth by sol EPD. At the left, we see the beginning of the nanowire growth. Positively charged sol particles are moving electrophoreticly towards the negative electrode, depositing at the bottom of the pore, while the negatively charged counter ions are moving in the opposite direction. The center of the diagram shows a later time, as the densely packed sol particles fill up more of the pore. Lastly, the right side of the diagram shows a completely filled pore

voltages in the range of 10-400 V. It was found that lower voltages led to dense, solid nanorods, and higher voltages caused the formation of hollow tubules. The suggested mechanism is that the higher voltages cause dielectric breakdown of the anodic alumina, causing it to become charged similarly to the cathode. Electrostatic attraction between the ZnO nanoparticles and the pore walls then leads to tubule formation.

1.4 Motivation

Given all of the available methods for synthesizing oxide nanorods, one might wonder about the motivation for working on yet another processing technique for oxide nanorods. There are a number of points, however, which demonstrate that there is a need for a simpler and more general technique for the synthesis of nanorods.

For many of the techniques discussed above, there are limitations or difficulties of one sort or another that make them less than suitable as general techniques for the synthesis of oxide nanorods, particularly complex oxide nanorods. For any of the spontaneous growth techniques, there is the need for anisotropic growth, along with specific difficulties with each of the types of techniques. VS techniques may be inappropriate for many complex oxides, such as those that melt incongruently, or have a component that is much more volatile than the others are. In fact, other than the superconductor YBCO[9], few complex oxide nanorods have been reported via the VS technique.

VLS growth, though widely applied, also has difficulties that make it a less than ideal general technique. The first is the requirement of a catalyst that forms a eutectic melt with the oxide to be grown. This will limit the number of oxides that can be synthesized. A second problem is the possibility of catalyst incorporation into the grown nanorod. There will often be at least a minimal solid solubility of the catalyst in the grown oxide, leading to a material that is impure. Additionally, VLS growth has not been widely adapted for the growth of complex oxides.

Lastly, there is the more practical problem with VS and VLS growth methods, namely that they often require large and expensive vacuum equipment, vapor growth chambers or high-power lasers. This type of equipment is not readily available to all

researchers that may be interested in synthesizing nanorods. Similar concerns exist for lithographic techniques, in addition to their lack of wide applicability.

Template methods such as electrodeposition or melt filling are only available for a limited number of systems. Converting through chemical reactions is also limited in its scope. For example, oxidation of metal nanowires would likely be an unsuitable method for synthesizing complex oxide nanowires. Although it would be possible to synthesize metal nanowires containing the desired stoichiometric ratio of metals (for many, but not all metals), it would be difficult to guarantee that oxidizing this nanowires would yield nanowires of the desired oxide composition.

Direct filling of a template with a colloidal (sol gel) suspension is a method that overcomes many of the above problems. It is simple, low cost, and applicable to nearly any conceivable oxide material, including complex oxides. There are, however, some potential limitations to this technique. The main drawback is that capillary action is the only driving force to form nanorods from the sol. In addition, sols commonly have a low solids content (~5 vol%), so that even if the pores are filled with sol, the packing of solids in the pores is low. Increasing the concentration of the sol could help this somewhat, but raising the concentration too high would result in either a sol viscous enough that filling of the pores would be difficult, or destabilization of the sol. Thus, the packing of material within the pore is likely to be significantly less than the maximum possible density. This could potentially lead to cracking and defects caused by the large volume change upon drying as the solvent is removed. In addition, the degree of shrinkage will be high, leading to nanorods that do not have the shape and dimensions of the template used, or are hollow tubes.

In order to have the advantages supplied by sol filling of templates and overcome the limitations inherent in this method, it is useful to turn to a combination of templating with sol electrophoretic deposition. When used to form coatings, this method has been shown to yield films of greater thickness, density and quality than traditional sol-gel methods alone[120,121]. An additional advantage of the sol EPD technique is the potential to synthesize patterned arrays of oxide nanorods directly on a surface. Such unidirectional arrays of nanorods would have a number of potential applications.

Furthermore, template-based growth by sol electrophoretic deposition makes it possible to synthesize organic-inorganic hybrid nanorods as well as to incorporate biocomponents into oxide nanorods.

1.5 Scope

Following a general introduction and literature review of the growth of nanorods, and a brief outline of the rationale of our research in the present chapter, Chapter 2 presents and discusses the experimental results of the template-based growth of nanorods of several oxide ceramics, formed by means of a combination of sol-gel processing and electrophoretic deposition. Both single metal oxides (TiO_2, SiO_2) and complex oxides ($BaTiO_3$, $Sr_2Nb_2O_7$, and $Pb(Zr_{0.52}Ti_{0.48})O_3$) have been grown by this method. Uniformly sized nanorods of about 45-200 nm in diameter and 10 μm in length were grown over large areas with near unidirectional alignment. Desired stoichiometric chemical composition and crystal structure of the oxide nanorods was readily achieved by an appropriate procedure of sol preparation, with an appropriate heat treatment (e.g., 700 °C for 15 min for PZT) for crystallization and densification.

Chapter 3 examines selected properties of some of the nanorods. These include the conductivity of ITO nanorods, the electrochromic properties of V_2O_5 and TiO_2 nanorods, and the dielectric properties of PZT nanorods.

Chapter 4 examines the formation and properties of silica and titania nanorods encapsulated with a thin gold shell. Nanorods of silica and titania ~10 μm in length and with diameters ~100-200 nm are made by combining sol-gel electrophoresis with a suitable template. After removing the template at high temperature, the surface of the rods is re-hydrolyzed by heating in water. 3-Aminopropyltrimethoxysilane is then reacted with the surface hydroxyl groups, and self-assembling amine functionality on the surface of the rods. Finally, a thin layer of gold was formed on the surface by reacting with these groups, which act as anchoring sites. UV-Vis absorbance spectra of these core-shell nanorod samples are both recorded and calculated from Mie scattering theory to determine the relationships between shell thickness, core size, core material and properties.

Finally, Chapter 5 summarizes the work completed, and outlines areas of future work that could be pursued. These areas include valence control in materials synthesized, doping of oxide nanorods and synthesis of single-crystal nanorods and studies of nanorod properties.

Notes to Chapter 1

[1] Sun Y.; Gates, B.; Mayers, B.; Xia, Y *Nano Lett.* **2002**, *2*, 165.

[2] Wong, E.W; Sheehan, P.E.; Lieber, C.M. *Science* **1997**, *277,* 1971.

[3] Tan, Y.T.; Durrani; Z.A.K.; Ahmed, H. *J. Appl. Phys.* **2001**, *89*, 1262.

[4] Lieber, C.M. *Solid State Commun.* **1998**, *107,* 607.

[5] Masuda, H.; Ohya, M.; Nishio, K.; Asho, H.; Nakao, M.; Nohtomi, M.; Yokoo, A; Tamamura, T. *Jpn. J. Appl. Phys. 2* **2000**, *39*, L1039.

[6] Patzke, G.R.; Krumeich, F; Nesper, R. *Agnew. Chem. Int. Ed.* **2002**, *41*, 2446.

[7] Pan, Z.W.; Dai, Z.R.; Wang, Z.L. *Science* **2001**, *291*, 1947.

[8] Dai, Z.R.; Pan, Z.W.; Wang, Z.L. *Solid State Commun.* **2001**, *118*, 351.

[9] Zhang, Y.F.; Tang, Y.H.; Duan, X.F.; Zhang, Y.; Lee, C.S.; Wang, N.; Bello, I.; Lee, S.T. *Chem. Phys. Lett.* **2000**, *323*, 180.

[10] Gundian, G.; Govindaraj; A.; Rao, C.N.R. *Chem. Phys. Lett.* **2002**, *351*, 189.

[11] Jiang, X.; Herricks, T.; Xia, Y. *Nano. Lett.* **2002**, *2*, 1333.

[12] Peng, X.S.; Wang, Y.W.; Zhang, J.; Wang, X.F.; Zhao, L.X.; Meng, G.W.; Zhang, L.D. *Appl. Phys. A* **2002**, *74*, 437.

[13] Fu, Y.; Chen, J.; Zhang, H. *Chem. Phys. Lett.* **2001**, *350*, 491.

[14] Gu, G.; Zheng, B.; Han, W.Q.; Roth, S.; Liu, J. *Nano Lett.* **2002**, *2*, 849.

[15] Bai, Z.G.; Yu, D.P.; Zhang, H.Z.; Ding, Y.; Wang, Y.P.; Gai, X.Z.; Hang, Q.L.; Xiong, G.C.; Feng, S.Q. *Chem. Phys. Lett.* **1999**, *303*, 311.

[16] Yin, Y.; Zhang, G.; Xia, Y. *Adv. Funct. Mater.* **2002**, *12*, 293.

[17] Shen, Z.Q.; He, L.L.; Wu, E.D.; Fan, Y.Y.; He, J.F.; Cheng, H.M.; Li, D.X.; Ye, H.Q. *J. Mater. Res.* **2002**, *17*, 2761.

[18] Park, W.I.; Kim, D.H.; Jung, S.-W.; Yi, G.-C. *Appl. Phys. Lett.* **2002**, *80*, 4232.

[19] Wu, J.-J.; Yu, C.-C., *J. Phys. Chem. B.* **2004**, *108*, 3377.

[20] Vayssieres, L.; Beermann, N.; Lindquist, S.-E.; Hagfeldt, A. *Chem. Mater.* **2001**, *13*, 233.

[21] Ni, Y.; Ge, X.; Liu, H.; Zhang, Z.; Ye, Q.; Wang, F. *Mater. Lett.* **2001**, *49*, 185.

[22] Muster, J.; Kim, G.T.; Krstic, V.; Park, J.G.; Park, Y.W.; Roth, S.; Burghard, M. *Adv. Mater.* **2000**, *12*, 420.

[23] Govender, K.; Boyle, D.S.; O'Brien, P.; Binks, D.; West, D.; Coleman, D. *Adv. Mater.* **2002**, *14*, 1221.

[24] Tian, Z.R.; Voigt, J.A.; Liu, J.; Mckenzie B.; Mcdermott, M.J. *J. Am. Chem. Soc.* **2002**, *124*, 12954.

[25] Kumar, R.V.; Koltypin, Y.; Gedanken, A.; Felner, I. *J. Appl. Phys.* **2001**, *89*, 6324.

[26] Pol, V.G.; Palchik, O.; Gedanken, A.; Felner, I. *J. Phys. Chem. B* **2002**, *106*, 9737.

[27] Guo, L.; Wu, Z.; Liu, T.; Wang, W.; Zhu, H. *Chem. Phys. Lett.* **2000**, *318*, 49.

[28] Zhang, D.-F.; Sun, L.-D.; Yin, J.-L.; Yan, C.-H., *Adv. Mater.* **2003**, *15*, 1022.

[29] Urban, J.J.; Yun, W.S.; Gu, Q.; Park, H., *J. Am. Chem. Soc.* **2002**, *124*, 1186.

[30] Guo, L.; Cheng, J.X.; Li, X.-Y.; Yan, Y.J.; Yang, S.H.; Yang, C.L.; Wang, J.N.; Ge, W.K. *Mat. Sci. Eng. C* **2001**, *16*, 123.

[31] Wang, W.; Wang, G.; Wang, X.; Zhan, Y.; Liu, Y.; Zheng, C. *Adv. Mater.* **2002**, *14*, 67.

[32] Liao, H.W.; Wang, Y.F.; Liu, X.M.; Li, Y.D.; Qian, Y.T. *Chem. Mater.* **2000**, *12*, 2819.

[33] Chen, Q.; Zhou, W.; Du, G.; Peng, L.-M. *Adv. Mater.* **2002**, *14*, 1208.

[34] Wang, X.; Li, Y. *Chem. Comm.* **2002**, 764.

[35] Wang, X.; Li, Y. *J. Am. Chem. Soc.* **2002**, *124*, 2880.

[36] Zhang, J.; Sun, L.; Pan, H.; Liao, C.; Yan, C. *New J. Chem.* **2002**, *26*, 33.

[37] Patzke,G.R.; Michailovski, A.; Krumeich, F.; Nesper, R.; Grunwaldt, J.-D.; Baiker, A. *Chem. Mater.* **2004**, *16*, 1126.

[38] Pan, D.; Shuyuan, Z.; Chen, Y.; Hou, J.G. *J. Mater. Res.* **2002**, *17*, 1981.

[39] Zhang, H.T.; Gui, Z.; Fan, R.; Chen, X.H. *Inorg. Chem. Comm.* **2002**, *5*, 399.

[40] Zhu, D.; Zhu, H.; Zhang, Y. *Appl. Phys. Lett.* **2002**, *80*, 1634.

[41] Penn, R.L.; Banfield, J.F. *Geochim. Cosmochim. Ac.* **1999**, 63, 1549.

[42] Pacholski, C.; Kornowski, A.; Weller, H. *Angew. Chem. Int. Ed.* **2002**, *41*, 1188.

[43] Wang, W.; Xu, C.; Wang, G.; Liu, Y.; Zheng, C. *Adv. Mater.* **2002**, *14*, 837.

[44] Liu, Y.; Wang, G.; Xua, C.; Wang, W. *Chem. Comm.* **2002**, 1486.

[45] Liu, Y.; Yin, C.; Wang, W.; Zhan, Y.; Wang, G. *J. Mater. Sci. Lett.* **2002**, *21*, 137.

[46] Liu, Y.; Zheng, C.; Wang, W.; Yin, C.; Wang, G. *Adv. Mater.* **2001**, *13*, 1883.

[47] Wagner, R.S.; Ellis, W.C. *Appl. Phys. Lett.* **1964**, *4*, 89.

[48] Wagner, R.S.; Ellis, W.C.; Jackson, K.A.; Arnold, S.M. *J. Appl. Phys.* **1964**, *35*, 2993.

[49] Wagner, R.S.; In *Whisker Technology* (Levitt, A.P., Ed.), Wiley, New York, 1970.

[50] Huang, M.H.; Wu, Y.; Feick, H.; Tran, N.; Weber, E.; Yang, P. *Adv. Mater.* **2001**, *13*, 113.

[51] Yu, D.P.; Hang, Q.L.; Ding, Y.; Zhang, H.Z.; Bai, Z.G.; Wang, J.J.; Zou, Y.H.; Qian, W.; Xoing, G.C.; Feng, S.Q. *Appl. Phys. Lett.* **1998**, *73*, 3076.

[52] Liang, C. H.; Meng, G. W.; Wang, G. Z.; Wang, Y. W.; Zhang, L. D.; Zhang, S. Y. Appl. Phys. Lett. 2001, 78, 3202.

[53] Lao, J.; Huang, J.; Wang, D.; Ren, Z., *Adv. Mater.* **2004**, *16*, 65.

[54] Tang, C.; Bando, Y.; Sato, T. *J. Phys. Chem. B* **2002**, *106*, 7449.

[55] Gaskell, D.R. *Introduction to the Theromodynamics of Materials*, Taylor and Francis, Washington, D.C., 1995.

[56] Peng, X.S.; Meng, G.W.; Wang, X.F.; Wang, Y.W.; Zhang, J.; Liu, X.; Zhang, L.D. *Chem. Mater.* **2002**, *14*, 4490.

[57] Hanrath, T.; Korgel, B.A. *Adv. Mater.* **2003**, *15*, 437.

[58] Hanrath, T.; Korgel, B.A. *J. Am. Chem. Soc.* **2002**, *124*, 1424.

[59] Kan S.,; Mokari, T.; Rothenberg, E.; Banin, U. *Nature Mater.* **2003**, *2*, 155.

[60] Xiao, J.; Xie, Y.; Tang, R.; Qian, Y. *J. Solid State Chem.* **2001**, *161*, 179.

[61] Kurihara, K.; Iwadate, K.; Namatsu, H.; Nagase, M.; Murase, K. *J. Vac. Sci. Technol. B* **1995**, *13*, 2170.

[62] Liu, H.I.; Biegelsen, D.K.; Ponce, F.A.; Johnson, N.M.; Pease, R.F. *Appl. Phys. Lett.* **1994**, *64*, 1383.

[63] Hashimoto, M.; Koreeda, T.; Koshida, N.; Komuro, M.; Atoda, N. *J. Vac. Sci. Technol. B* **1998**, *16*, 2767.

[64] Xia, Y.; Rogers, J.A.; Paul, K.E.; Whitesides, G.M. *Chem. Rev.* **1999**, *99*, 1823.

[65] Li, D.; Xia, Y. *Nano. Lett.* **2003**, *3*, 555.

[66] Viswanathamurthi, P.; Bhattarai, N.; Kim, H.Y.; Lee, D.R. *Scripta Mater.* **2003**, *49*, 577.

[67] Viswanathamurthi, P.; Bhattarai, N.; Kim, H.Y.; Lee, D.R.; Kim, S.R.; Morris, M.A. *Chem. Phys. Lett.* **2003**, *374*, 79.

[68] Li, D.; Herricks, T.; Xia, Y. *Appl. Phys. Lett.* **2003**, *83*, 4586.

[69] Wang, Y.; Furlan, R.; Ramos, I.; Santiago-Aviles, J.J. *Appl. Phys. A* **2004**, *78*, 2004, 1043.

[70] Furneaux, R.C.; Rigby, W.R.; Davidson, A.P. *Nature* **1989**, *337*, 147.

[71] Fleisher, R.L.; Price, P.B.; Walker, R.M. *Nuclear Tracks in Solids*, University of California Press, Berkeley, CA, 1975.

[72] Tonucci, R.J.; Justus, B.L.; Campillo, A.J.; Ford, C.E. *Science* **1992**, *258*, 783.

[73] Possin, G.E. *Rev. Sci. Instrum.* **1970**, *41*, 772.

[74] Fan, S.; Chapline, M.G.; Franklin, N.R.; Tombler, T.W.; Cassell, A.M.; Dai, H. *Science* **1999**, *283*, 512.

[75] Wu, C.-G.; Bein, T. *Science* **1994**, 264, 1757.

[76] Enzel, P.; Zoller, J.J.; Bein, T. *Chem. Comm.* **1992**, 633.

[77] Guerret-Piecourt, C.; Le Bouar, Y.; Loiseau, A.; Pascard, H. *Nature* **1994**, *372*, 761.

[78] Zach, M.P.; Newberg, J.T.; Sierra, L.; Hemminger, J.C.; Penner, R.M., *J. Phys. Chem. B* **2003**, *107*, 5393.

[79] Li, Y.; Wan, J.; Gu, Z. *Mat. Sci. Eng. A* **2000**, *286*, 106.

[80] Lakshmi, B.B.; Dorhout, P.K.; Martin, C.R. *Chem. Mater.* **1997**, *9*, 857.

[81] Lakshmi, B.B.; Patrissi, C.J.; Martin, C.R. *Chem. Mater.* **1997**, *9*, 2544.

[82] Brinker, C.J.; Scherer, G.W. *Sol-Gel Science: the Physics and Chemistry of Sol-Gel Processing*, Academic Press, San Diego, CA, 1990.

[83] Cheng, B.; Samulski, E.T. *J. Mater. Chem.* **2001**, *11*, 2901.

[84] Zhang, M.; Bando, Y.; Wada, K.; Kurashima, K. *J. Mater. Sci. Lett.* **1999**, 18, 1911.

[85] Wang, Z.; Li, H.L. *Appl. Phys. A* **2002**, *74*, 201.

[86] Reed, J.S. *Introduction to Principles of Ceramic Processing*, Wiley, New York, 1988.

[87] Lei, Y.; Zhang, L.D.; Meng, G.W.; Li, G.H.; Zhang, X.Y.; Liang, C.H.; Chen, W.; Wang, S.X. *Appl. Phys. Lett.* **2001**, *78*, 1125.

[88] Zhou Y.; Li, H. *J. Mater. Sci* **2002**, *37*, 5261.

[89] Ma, X.; Zhang, H.; Xu, J.; Niu, J.; Yang, Q.; Sha, J.; Yang, D. *Chem. Phys. Lett.* **2002**, *363*, 579.

[90] Ajayan, P.M.; Iijima, S. *Nature* **1993**, *361*, 333.

[91] Ajayan, P.M. ; Ebbesen, T.W.; Ichihashi, T.; Iijima, S.; Tanigaki, K.; Hiura, H. *Nature* **1993**, *362*, 522.

[92] Ajayan, P.M.; Stephan, O.; Redlich, P.; Colliex, C. *Nature* **1995**, *375*, 564.

[93] Chen, Y.K.; Green, M.L.H.; Tsang, S. C. *Chem. Comm.* **1996**, 2489.

[94] Ryan, J.V.; Berry, A.D.; Anderson, M.L.; Long, J.W.; Stroud, R.M.; Cepak, V.M.; Browning, V.M.; Rolison, D.R.; Merzbacher, C.I. *Nature* **2000**, *406*, 169.

[95] Park, I.-S.; Jang, S.-R.; Hong, J.S.; Vittal, R.; Kim, K.-J. *Chem. Mater.* **2003**, *15*, 4633.

[96] Nishino, J.; Teekateerawej, S.; Nosaka, Y. *J. Mater. Sci. Lett.* **2003**, *22*, 1007.

[97] Kavan, L.; O'Regan, B.; Kay, A.; Grätzel, M. *J. Electroanal. Chem.* **1993**, *346*, 291.

[98] Lei, Y.; Zhang, L.D.; Fan, J.C. *Chem. Phys. Lett.* **2001**, *338*, 231.

[99] Zhang, X.; Yao, B.; Zhao, L.; Liang, C.; Zhang, L.; Mao, Y. *J. Electrochem. Soc.* **2001**, *148*, G398.

[100] Miao, Z.; Xu, D.; Ouyang, J.; Guo, G.; Zhao, X.; Tang, Y. *Nano Lett.* **2002**, *2*, 717.

[101] Natarajan, C.; Nogami, G. *J. Electrochem. Soc.* **1996**, *143*, 1547.

[102] Zheng, M.J.; Zhang, L.D.; Li, G.H.; Shen, W.Z. *Chem. Phys. Lett.* **2002**, *363*, 123.

[103] Kenane, S.; Piraux, L. *J. Mater. Res.* **2002**, *17*, 401.

[104] Huang, L.; Wang, H.; Wang, Z.; Mitra, A.; Zhao, D.; Yan, Y. *Chem. Mater.* **2002**, *14*, 876.

[105] Zhang, Y.; Zhu, J.; Zhang, Q.; Yan, Y.; Wang, N.; Zhang, X. *Chem. Phys. Lett.* **2000**, *317*, 504.

[106] Satishkumar, B. C.; Govindaraj, A.; Vogl, E.M.; Basumallick, L.; Rao, C.N.R. *J. Mater. Res.* **1997**, *12*, 604.

[107] Satishkumar, B. C., Govindaraj, A.; Natha, M.; Rao, C. N. R. *J. Mater. Chem.* **2000**, *10*, 2115.

[108] Wu, H.-Q.; Shao, M.-W.; Wei, X.-W.; Gu, J.-S.; Qu, M.-Z. *Chinese J. Chem.* **2002**, *20*, 610.

[109] Wang, Y.W.; Liang, C.H.; Wang, G.Z.; Gao, T.; Wang, S.X.; Fan, J.C.; Zhang, L.D. *J. Mater. Sci. Lett.* **2001**, *20*, 1687.

[110] Zheng, M.; Li, G.; Zhang, X.; Huang, S.; Lei, Y.; Zhang, L. *Chem. Mater.* **2001**, *13*, 3859.

[111] Zheng, M.; Zhang, L.; Zhang, X.; Zhang, J.; Li, G. *Chem. Phys. Lett.* **2001**, *334*, 298.

[112] Kolmakov, A.; Zhang, Y.; Cheng, G.; Moskovits, M., *Adv. Mater.* **2003**, *15*, 997.

[113] Li, Y.; Cheng, G.S.; Zhang, L.D. *J. Mater. Res.* **2000**, *15*, 2305.

[114] Min, Y.-S.; EBae, E.J.; Jeong, K.S.; Cho, Y.J.; Lee, J.-H.; Choi, W.B.; Park, G.-S., *Adv. Mater.* **2003**, *15*, 1019.

[115] Zhitomirsky, I. *Adv. Colloid Interf. Sci.* **2002**, *97*, 297.

[116] Reed, J.S. *Introduction to the Principles of Ceramic Processing*, John Wiley & Sons, New York, 1988.

[117] Hunter, R.J. *Zeta Potential in Colloid Science: Principles and Applications*, Academic Press, London, 1981.

[118] Callister, W.D. *Materials Science and Engineering: An Introduction*, John Wiley & Sons, New York, 1997.

[119] Wang, Y.C.; Leu, I.C.; Hon, M.H. *J. Cryst. Growth* **2002**, *237-239*, 564.

[120] Hasegawa, K.; Kunugi, S.; Tatsumisago, M.; Minami, T. *J. Sol-Gel Sci. Tech.* **1999**, *15*, 243.

[121] Shaw, L.; Abbaschian, R. *J. Am. Ceram. Soc.* **1995**, *78*, 3376.

2 Formation of oxide nanorods by sol gel electrophoresis

2.1 Introduction

Given the wide variety of available techniques for the synthesis of oxide nanostructures, what are the reasons for using sol-gel electrophoresis with template synthesis? Although there are some drawbacks to the technique, it does have a large number of advantages. The primary advantages stem from the flexibility and of sol gel processing. Sol gel processing can be used to synthesize almost any conceivable (both thermodynamically stable and metastable) oxide material, whereas other techniques are often limited in the number and type of oxides they can synthesize. For example, sol-gel methods can synthesize tetragonally stabilized ZrO_2, without Ca or Y doping[1]. Sol gel processing can easily synthesize oxides of the desired stoichiometric composition, such an in the formation of $Ti_{1-x}V_xO_2$ solid solutions where x can be arbitrarily tuned between 0 and 0.15[2]. Sol gel processing has the ability to incorporate organic (such as pH sensitive dyes[3]) and biological (such as proteins[4]) components.

In addition, the sol-gel template method is a relatively low-cost method, which requires no expensive specialized equipment. As was discussed in the previous chapter, the combination of electrophoresis with sol gel processing can lead to potentially denser, higher-quality solid nanorods than those synthesized without electrophoresis. Lastly, template methods (in general) are flexible, in that a wide variety of template pore diameters and lengths are possible. In addition, template methods are appropriate for synthesis of both free nanorods and arrays of parallel-aligned nanorods attached to a substrate. Thus, by combining the advantages of sol gel processing and electrophoresis with the ease of template methods, one has a simple, general technique for synthesizing nanorods of almost any conceivable oxide material.

2.2 Brief overview of sol-gel processing

Sol-gel processing is a solution chemical route to the synthesis of inorganic and organic-inorganic hybrid materials, which offers many advantages. Chief among them

are low processing temperatures (typically < 100 °C) and molecular level homogeneity. Sol-gel processing is particularly useful in making complex metal oxides and temperature sensitive organic-inorganic hybrid materials.

A typical sol-gel process consists of hydrolysis and condensation of precursors. Precursors can be either organic, such as metal alkoxides, or inorganic salts. Organic or aqueous solvents may used to dissolve the precursors, and catalysts are often added to promote and/or control both the hydrolysis and condensation reactions. There are two key steps in sol-gel processing: hydrolysis and condensation. Hydrolysis refers to the removal of ligands from the precursors, and the formation of metal hydroxides. Condensation reactions between hydroxide groups then lead to the –M-O-M- linkages that build up the sol nanoparticles.

Hydrolysis:

$$M(OR)_4 + x\,H_2O \rightarrow M(OR)_{4-x}(OH)_x + x\,ROH$$

Condensation:

$$M(OR)_{4-x}(OH)_x + M(OR)_{4-x}(OH)_x \rightarrow (OR)_{4-x}(OH)_{x-1}M - O - M(OR)_{4-x}(OH)_{x-1} + H_20$$

Both hydrolysis and condensation reactions are multi-step processes, which can proceed both sequentially and/or in parallel. Condensation results in the formation of nanoscale clusters of metal oxides and hydroxides, often with organic groups attached. These organic groups may be due to incomplete hydrolysis, or introduced as non-hydrolysable organic ligands. The size of these nanoscale clusters, along with the morphology and microstructure of the final product, can be tailored by controlling the hydrolysis and condensation reactions.

The ability to synthesize complex oxide is one of the chief strengths of the sol-gel method. It is not trivial, however, to obtain the desired multi-component oxide product. A major requirement is that the constituent materials are homogeneously mixed at the molecular level, with the desired stoichiometric ratio in each nanoscale cluster. To achieve this, one must carefully control the hydrolysis and condensation reactions of the various precursors. The reactivity of each precursor is likely different

from the other precursors present, meaning that it undergoes hydrolysis and condensation at a different rate. This can lead to homocondensation, that is, the precursors of a given metal M only condensing with other M precursors. For each metal, only nanoclusters of that single metal oxide would be present, and the sol would comprise a heterogeneous dispersion of various single metal oxides. The resulting product would be a mixture or a composite of multiple oxide phases, instead of a single-phase complex oxide.

There are several techniques for avoiding this homocondensation. Modification of precursors, the use of complex precursors, partial hydrolysis and multi-step hydrolysis and condensation are common techniques employed to achieve heterocondensation between the various precursors.

Another problem in making complex oxide sols is that the constituent precursors may exert a catalytic effect on one another. As a result, the hydrolysis and condensation reaction rates in combination may be significantly different from those when the precursors are processed separately.

By carefully controlling the sol chemistry, suspensions of nearly monodisperse nanoparticles of various oxides can be synthesized. The key issue is to promote simultaneous, homogeneous nucleation in a diffusion-limited system. The particle size can be varied by changing the concentration and aging time[5]. A typical sol comprises nanoclusters ranging from 1 to 100 nm in size.

In colloidal systems such as sols, gravity has a negligible influence, whereas Brownian motion plays an important role. Nanoparticles possess a huge surface area /volume ratio and thus a large surface energy. There is a strong tendency for such nanoscale clusters to agglomerate, and thus mechanisms are needed to provide stability to the sol. Two types of mechanisms are available: polymeric (or steric) stabilization, and electrostatic stabilization. Polymeric stabilization works by adsorbing polymeric molecules onto the nanocluster or nanoparticle surface; spatial exclusion then prevents two clusters from getting close enough to agglomerate. Electrostatic stabilization comes from the fact that surfaces in a polar solvent or electrolyte solution will develop a charge. This surface charge interacts with other charged species in the sol to form a

charged structure around the particle, leading to electrostatic repulsion between nanoparticles, preventing agglomeration. These two mechanisms can also be combined as electrosteric stabilization, where the electrostatic effect is due to either the charged nanoparticle surface, or an uneven charge distribution in the polymer molecules.

2.3 Experimental procedure

2.3.1 Sol preparation

Sol-gel electrophoresis can synthesize a wide variety of oxide nanorod materials. The only requirement is an electrostatically stabilized sol. For each of the various oxides prepared, a different sol preparation is required. A detailed description of the PZT sol provides an example of the steps involved in the sol gel processing. For all other oxides, outlines of the sol preparations follow. Table 2-1 summarizes the chemicals and conditions for the preparation of the various sols.

The chemicals used in making the sols are: titanium (IV) isopropoxide, zirconium n-propoxide (70% in propanol), tetraethyl orthosilicate, lead (II) acetate, barium acetate, niobium pentachloride, strontium nitrate, indium (III) chloride and tin (IV) chloride. Hydrochloric acid, glacial acetic acid, lactic acid, citric acid monohydrate, ethylene glycol, glycerol, ethanol and deionized (DI) water are also used.

The preparation of PZT sol follows the method outlined in Reference 6. First, lead (II) acetate is dissolved in glacial acetic acid, heating to 110° C for ~15 min. This heating dehydrates the lead acetate, so that there is only a minimal amount of water present in the sol. After heating, this lead-containing solution is cooled. Because of the volatility of PbO, an excess amount of lead (5 mol%) is used in the fabrication of this sol. This is in line with traditional processing of PZT, where 5-25% excess Pb is used[7]. In a separate beaker, titanium (IV) isopropoxide and zirconium (IV) n-propoxide are mixed together for ~10 min at room temperature. Because these precursors are highly reactive and moisture- sensitive (particularly the Ti isopropoxide), it is important to minimize the exposure of this mixture to the air. When the lead solution has cooled to

Table 2-1 Chemicals used for the synthesis of various nanorods.

Sol	Precursors	Solvents/Other chemicals	Approx. pH
$Pb(Zr,Ti)O_3$	Lead (II) acetate, titanium isopropoxide, zirconium n-propoxide	Glacial acetic acid, water, lactic acid, glycerol, ethylene glycol	~4
TiO_2	Titanium (IV) isopropoxide	Glacial acetic acid, water	~2
$BaTiO_3$	Titanium (IV) isopropoxide, barium acetate	Glacial acetic acid, ethylene glycol	~4
SiO_2	Tetraethyl orthosilicate	Ethanol, water, hydrochloric acid	~2
$SrNb_2O_6$	Strontium nitrate, niobium chloride	Ethylene glycol, ethanol, citric acid, water	~1
ITO	Indium chloride, tin (IV) chloride	Ethylene glycol, ethanol, citric acid, water	~1
Nb_2O_5	Niobium chloride	Ethylene glycol, ethanol, citric acid, water	~1

room temperature, it is combined with the Ti/Zr mixture under stirring. Because acetic acid acts as both a solvent and a chelating agent, the mixture is more stable, and the presence of atmospheric water does not detrimentally affect the sol. After the two solutions become well mixed, addition of DI water initiates and sustains hydrolysis and condensation reactions. Because the precursors are well mixed, it is possible for the hydrolyzed products to undergo heterocondensation reactions. That is, the different metal hydroxides condense with one another, forming a metal-oxygen-metal network that includes all three of the metals (Pb, Ti and Zr). About 15 min stirring at room temperature allows these reactions to proceed. Lastly, lactic acid, glycerol and ethylene glycol are added to adjust the viscosity and stability of the sol. Such prepared sols have a concentration of about 5 vol% PZT, and are stable for several weeks at room temperature. Figure 2-1 is a flow chart showing the steps in the PZT sol preparation.

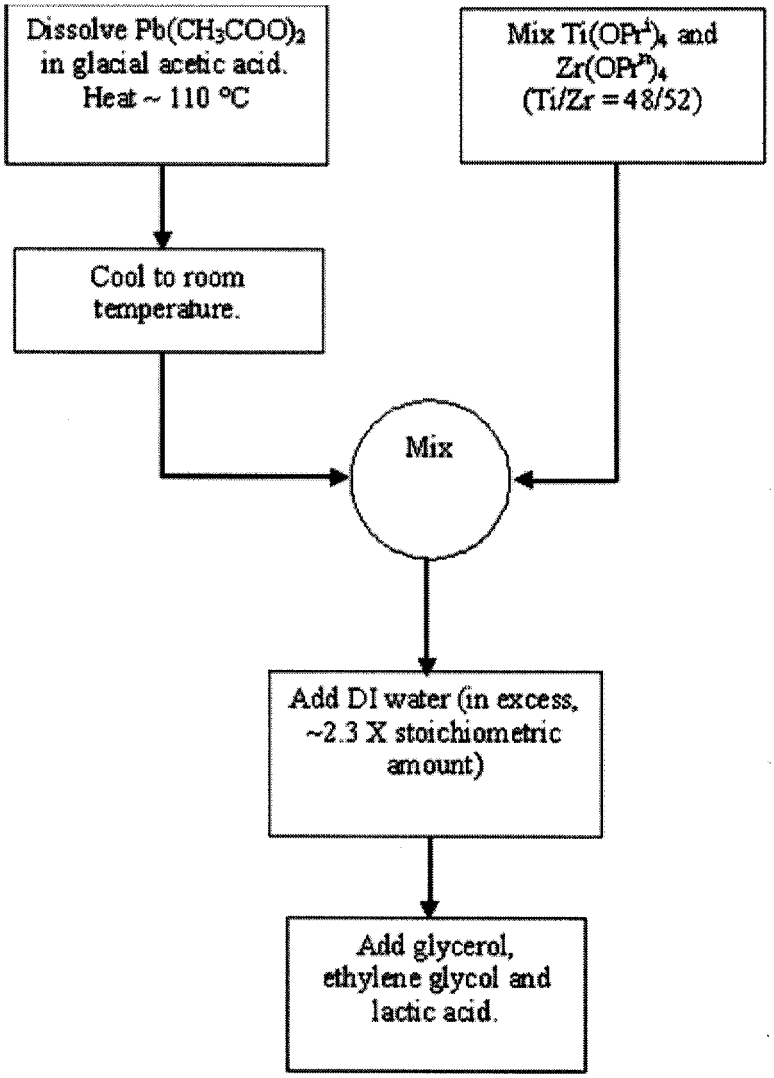

Figure 2-1 A flow chart of the PZT sol preparation.

The TiO_2 sol forms by dissolving titanium (IV) isopropoxide in glacial acetic acid, stirring for 30 min at room temperature. After addition of DI water, the sol is stirred for an additional 30 min. Upon addition of the water, a white precipitate instantaneously forms, which peptizes after the first 5 minutes of stirring, yielding a clear sol. The TiO_2 sol formed is stable at room temperature for about a week, and had a pH ~1.7. An estimate of the sol particle size is determined from the UV-Vis absorbance spectrum of the TiO_2 sol. This spectrum shows an absorbance feature attributable to the band-gap absorbance of amorphous TiO_2. The absorption coefficient near an indirect band-gap transition varies as[8]:

$$\alpha h\nu \propto \left(h\nu - E_g\right)^2 \qquad \textbf{Equation 2-1}$$

where α is the absorption coefficient, $h\nu$ is the incident photon energy and E_g is the optical band gap of the material. Figure 2-2 shows a plot of $(\alpha h\nu)^{1/2}$ vs. $h\nu$. Extrapolating the linear portion of this graph to the x-axis yields the observed energy gap of 2.96 eV. Amorphous TiO_2 has been reported to have a band gap energy of about 2.8 eV[9], which means that the particles in the TiO_2 sol have their band-gap shifted by about 0.16 eV from the bulk value. If we assume that this shift is from quantum confinement, then it is possible to determine the particle size that would give such a shift[10].

$$\Delta E_g = \frac{h^2}{8\mu R^2} - 1.8\frac{e^2}{\varepsilon R} \qquad \textbf{Equation 2-2}$$

In this equation, μ is the reduced effective mass of an exciton in the material ($1.63m_e$[10]), e is the electron charge, ε is the permittivity of the TiO_2 ($184\varepsilon_0$[10]) and R is the particle size. Solving for R and plugging in the known values yields a particle size of about 0.8 nm.

A new citric acid-based sol was developed for the ITO nanorods. This was necessary because existing sol recipes (such as that by Alam et al[11]) failed in the formation of nanorods. This method derives from the ethylene glycol thermal

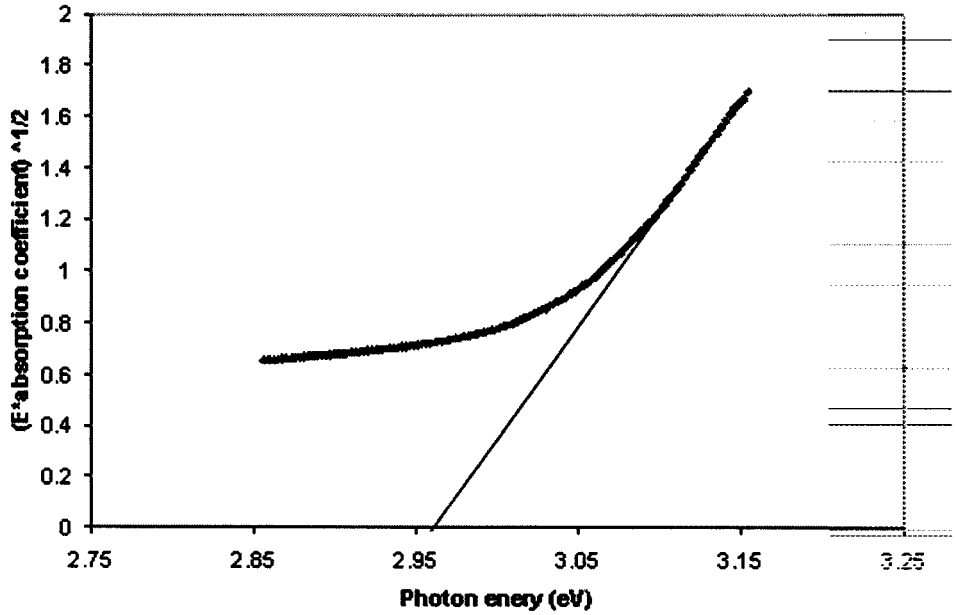

Figure 2-2 Band gap energy determination for TiO_2 sols.

decomposition method of Yamamoto et al[12] and the colloidal sol of Stoica et al[13]. Briefly, the technique consists of following. First, citric acid monohydrate is dissolved in a mixture of 3 parts ethanol and 2 parts ethylene glycol at 40 °C. The quantity of citric acid is such that the ratio of citric acid:(In+Sn) = 2:1. The desired amount of $SnCl_4$ is added to this solution under stirring. A Sn concentration of 10 at% was chosen to give good electrical conductivity, as reported by Alam et al[11]. Then, the $InCl_3$ is added to the solution, and this mixture is stirred for an additional 90 minutes. During the final half of this time, water is added to complete the hydrolysis of the precursors. The ratio of water:(In+Sn) is 3.1:1, including the water of hydration in the citric acid. At the end of the stirring, the sol is cooled to room temperature and vacuum filtered with ~1μm filter paper. The final concentration of ITO in the sol is about 0.12M.

$BaTiO_3$ sol is prepared as in Reference 14, by dissolving barium acetate in glacial acetic acid while stirring. This was done at room temperature, and the solution was stirred for about 30 min. To this solution, titanium (IV) isopropoxide was added, and the mixture was stirred for about 30 min. Lastly, ethylene glycol was added, and the

sol was stirred at 90 °C for 1 hr. The resultant sol was stable at room temperature for a period of months, and had a pH of ~4.

$Sr_2Nb_2O_7$ sol is prepared using the same procedure as reported in Reference 6. A mixture of ethanol and ethylene glycol is heated to 40 °C, followed by the addition of citric acid and strontium nitrate, and 150 min stirring. The niobium pentachloride is then added, and the solution stirred for another 90 min. During this time, water is slowly added to the mixture, forming the sol. The final concentration of this sol is about 0.6M, and it is stable over a period of months at room temperature. The pH of the $Sr_2Nb_2O_7$ sol is ~1.

The SiO_2 sol is made by dissolving tetraethyl orthosilicate in a mixture of ethanol and DI water. A small amount of hydrochloric acid is added to the sol to adjust the pH to ~2, and the sol is stirred for 2 hrs at room temperature. The silica sol thus formed is rather stable, taking several weeks to gel at room temperature.

Nb_2O_5 sols were synthesized by a method adapted from Seraji et al. for $Sr_2Nb_2O_7$ sols[6]. This citric-acid method begins by mixing ethanol and ethylene glycol together at 40 °C. Citric acid monohydrate (CA) was added to this mixture, in a ratio of 2 moles CA to 1 mol Nb. After additional stirring, $NbCl_5$ was added, and the sol stirred for another 90 minutes. During this stirring, de-ionized water was added, such that the final ratio of H_2O:Nb = 5:1 (including the water of hydration from the CA).

While the pH of aqueous solutions are well-defined, in organic solvents the correlation between what is measured with a pH meter and the actual $[H^+]$ or $a(H^+)$ may be more difficult. However, most of the sols in this study contain a fair amount of water, making the correlation much better. In mixed water-organic systems, the difference between thermodynamically calculated and effective (experimentally measured) pK_a values is quite small[15]. Looking at the TiO_2 sol as an example, we find a measured pH of about 1.7. Using a tabulated value for pK_a of acetic acid in water (value, reference), and assuming unit activity coefficients, we can calculate a value of $[H^+]$ □ 0.013 mol/L, or a pH of 1.9. Looking at tables of pK_a for acids in water-alcohol mixtures, one finds that the values in these situations are within about 10% of the pure aqueous value, provided the alcohol content is not too high. If we assume that pK_a for

acetic acid in the sol is 20% greater than the aqueous value, the calculated pH is about 2.4. This suggests that for many of the sols, the value of pH recorded by the pH meter is a reasonable approximation of the $[H^+]$ present in the sol.

2.3.2 Electrophoretic deposition

Several variations of the experimental setup were tested for the growth of nanorods by sol electrophoresis. The templates used were either PC (100 or 200 nm pores 10 μm thick, or 50 nm pores 6 μm thick) or AAM (200 nm pores, 60 μm thick). The fundamental concept for all of these setups is that the template is attached to/in contact with the working electrode. This electrode is placed in the sol opposite a counter electrode of Pt mesh. The three main configurations of the experimental setup are discussed below.

In the first configuration, the template (PC or AAM) is attached to the electrode with a piece of double-sided conductive (carbon) tape, to provide a conductive path from the membrane to the cathode. This electrode is placed on top of and just in contact with the sol, and the sol is drawn into the membrane pores by capillary action, as shown schematically in Figure 2-3. While this method was effective, it had a few difficulties.

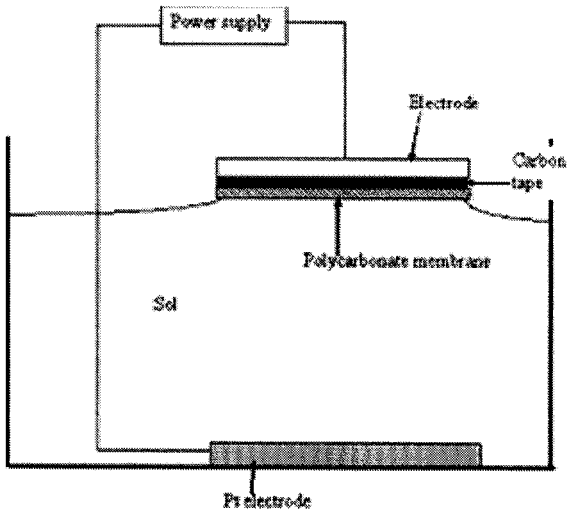

Figure 2-3 The initial experimental setup for the synthesis of nanorods.

First, the carbon tape used was very difficult to fully remove from the template, even after firing, leaving a black residue among the nanorod powder. Also, it was more difficult to control the distance (and thus field) with this setup, and there was concern that the high resistance of the carbon tape (~ 1 MΩ) might negatively influence the growth process. Thus a second, superior technique was developed.

The second method places the PC membrane and the working electrode in a polypropylene filter holder, held in place with a silicone gasket. This assembly contacts the sol. The Pt counter electrode is also placed in the sol, parallel to the working electrode. Figure 2-4 shows a schematic of the experimental setup. This is the preferred setup for growth in PC templates, but is not acceptable for AAM membranes, as screwing the working electrode into place tends to shatter the AAM. Thus, a third method was needed for growth in AAM templates.

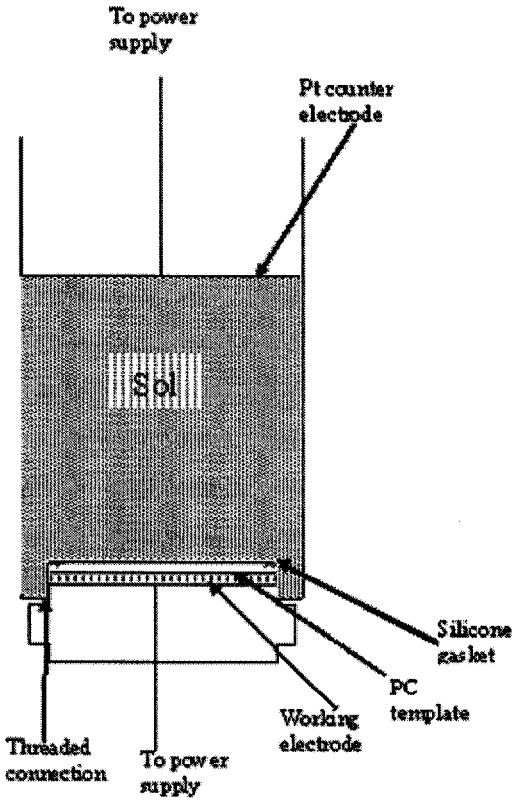

Figure 2-4 The revised experimental setup for use with PC templates.

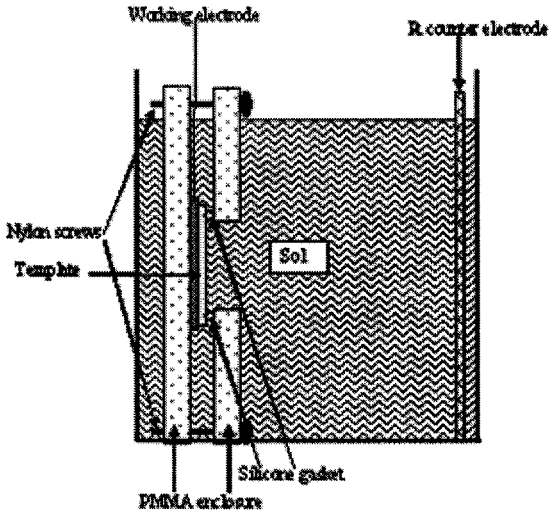

Figure 2-5 The revised experimental setup for use with AAM or PC templates

Lastly, nanorods can be grown in AAM templates by attaching the membrane to a working electrode, which is held parallel to the Pt counter electrode in a bath of the sol, shown in Figure 2-5. In all of the deposition setups, the counter electrode (whether anode or cathode) was Pt, but various working electrodes (Al, Ti, C) were tested. There was no apparent difference in the deposit with the different working electrodes.

For the electrophoretic growth, an appropriate potential is applied between the electrodes, which are typically separated by ~3 cm. The growth takes place over a period of ~20 min to ~3hrs, depending on the sol. After the electrophoretic deposition, excess sol is blotted off the membrane; the membrane is then transferred from the electrode to a crucible, and dried at ~100° C for several hours. Lastly, the dried samples are fired at a temperature between 500-700 °C for up to 60 min. This is to burn off the polycarbonate membranes, make the nanorods dense and crystallize the material (for all but SiO_2). The resulting material is a fine powder of the desired oxide nanorods.

2.3.3 Analysis

Several techniques were used to characterize the nanorods synthesized. More general analysis techniques (SEM, TEM and XRD) are discussed here; more specific

techniques (such as UV-Vis absorbance spectroscopy of gold-coated oxide nanorods) are discussed elsewhere.

2.3.3.1 SEM

Scanning electron microscopy (SEM, JEOL JSM-5200 and JEOL 840A) was used to study the morphology of the nanorods. Calcined nanorod powders were placed on an Al SEM stub coated with a conductive (carbon) tape, then sputter-coated with a thin Au/Pd layer prior to observation in the SEM.

2.3.3.2 XRD

For crystalline samples, (all except SiO_2), X-ray diffraction (XRD, Phillips PW1830) was used to determine the phases and crystal structures present, and to check for the presence of texture and degree of crystallinity. Samples of the calcined nanorod powders were placed on a glass slide and inserted into the diffractometer for analysis.

2.3.3.3 TEM

Some samples were analyzed with transmission electron microscopy (JEOL 2010 and Phillips EM420T) at accelerating voltages of 200 and 120 kV, respectively. Energy dispersive spectroscopy (EDS, Princeton Gamma Tech IMIX) was also done in the TEM for some samples. Samples were prepared for TEM analysis by suspending a portion of the calcined nanorods in acetone or ethanol. This suspension was dropped onto a Cu TEM grid and air-dried. Alternatively, some TEM samples were prepared by placing the nanorod powder directly in contact with the TEM grid. Lower magnification images were recorded to observe the entire structure of a nanorod; high-resolution images and electron diffraction were used to study the crystallinity and grain sizes of the nanorods.

2.4 Results and discussion

2.4.1 TiO_2 nanorods

Figure 2-6 shows SEM micrographs of TiO_2 nanorods grown in polycarbonate membranes. Growth was in templates with 50 - 200 nm diameter pores, and 5V was used for either 90 min (200 and 100 nm templates) or 60 min (50 nm template). All rods were fired at 500 °C for 60 min. These nanorods have a uniform diameter throughout their entire length, with a surface that is smooth over much or all of the length. Comparing the various rods, one can see that they all have roughly the same length and diameter. The image also shows that the rods arrange roughly parallel to one another over a broad area on the substrate. The diameter of the TiO_2 nanorods is estimated by measuring several tens of nanorods on each micrograph. The results of ~45 - 180 nm are approximately 10% smaller than the membrane pore diameter. This size difference is most likely from the volume shrinkage caused by densification during the heat treatment. Upon heating nanorod samples to 700 °C, the shrinkage in diameter increases to about 25%. Thus, the nanorods are not fully dense after heating to only 500 °C for 60 min; however, it is necessary to use a lower temperature if one wishes to have the anatase phase. Figure 2-6 also shows some broken rods, and it can be seen that these rods are solid and dense. Furthermore, Figure 2-6a shows that a thick layer was formed at one end of the nanorods (left-hand side), where the template contacted the sol during deposition. This sample was grown for a longer time, implying that the growth of the

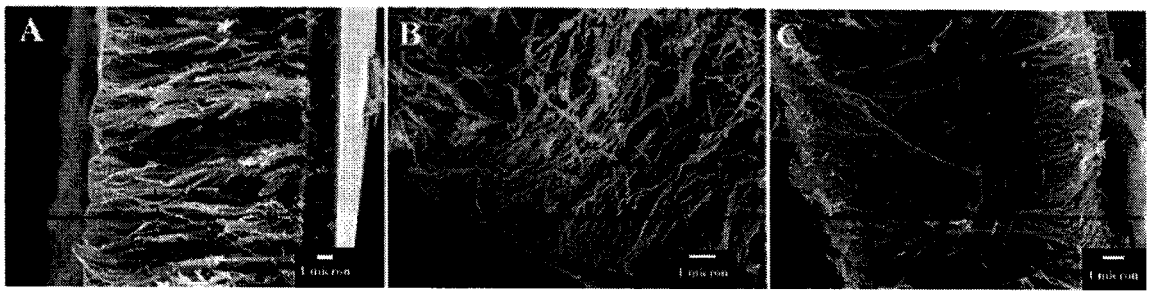

Figure 2-6 SEM micrographs of various TiO_2 nanorods. The length is ~10 μm, and the diameters are ~180 nm (A), ~90 nm (B) and ~45 nm (C). These correspond to about 10% lateral shrinkage from the original pore diameters. Samples were grown at 5 V for 90 min (a,b) or 60 min (c).

nanorods likely begins at the bottom of the pores, and proceeds from one side of the membrane to the other. For the TiO_2 rods grown in 50 nm templates, the drying time used exerts a strong influence on the fidelity of the nanorods. Samples dried at 100 °C for up to 24 hours showed no nanorods after firing at 500 °C. In samples dried for ~48 hours prior to firing, however, nanorods were observed. It is likely that this result is due to the increased degree of condensation that occurred in the sample dried for a longer time. By allowing the samples to undergo further condensation reactions, the rods formed were likely stronger, and thus better able to resist breakage upon firing.

Figure 2-7a shows a TEM micrograph of a TiO_2 nanorod grown in a 200 nm PC template at 1.67 V/cm for 30 min. The micrograph demonstrates that the nanorods are quite smooth and dense. Figure 2-7b shows a high-resolution TEM image and electron diffraction pattern, demonstrating that the nanorods are polycrystalline, with grains that are ~5 nm in size. This value is slightly smaller than the estimated size of the nanoparticles in the TiO_2 sol (~1 nm); however, the TiO_2 nanorod shown in this micrograph was fired at 700 °C, which would likely lead to larger grains.

XRD spectra of the TiO_2 rods are shown in Figure 2-8, along with the spectra for a powder formed from the same sol and fired at 500 °C for 60 min. From the powder XRD spectrum, it can be seen that the sample consists of the anatase phase. Note that there is a large amorphous background associated with the TiO_2 nanorods. This is owing to the small volume rods available for analysis, meaning that much of the X-ray beam was hitting the (amorphous) sample holder. XRD was also done on samples heated to 700 °C. In these nanorods (and powders), the TiO_2 was a mixture of the anatase and rutile phases (See Figure B-1, Appendix B). Higher sintering temperatures should lead to the formation of entirely rutile TiO_2 nanorods, although anatase has been found to be stable up to 800 °C in acetic acid-modified TiO_2 systems[16].

2.4.2 PZT nanorods

Figure 2-9 shows SEM images of the PZT nanorods grown from the PZT sol by means of electrophoretic deposition and fired at 700° C for 60 min in air. PZT nanorods grown in PC membranes with pore sizes of 50-200 nm show uniform size and near-

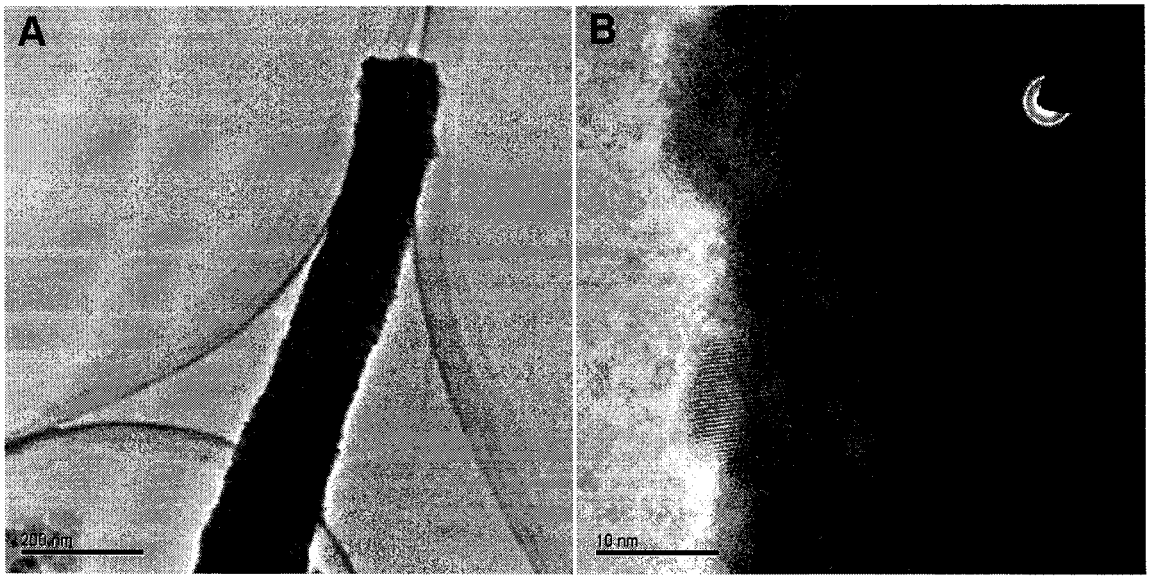

Figure 2-7 TEM micrographs of a TiO_2 nanorod grown in a 200 nm PC template at 1.67 V/cm for 30 min. Part A shows a single nanorod, demonstrating that the nanorods are quite smooth and dense. Part B shows a high-resolution TEM image and electron diffraction pattern, demonstrating that the nanorods are polycrystalline, with grains of ~5 nm in size

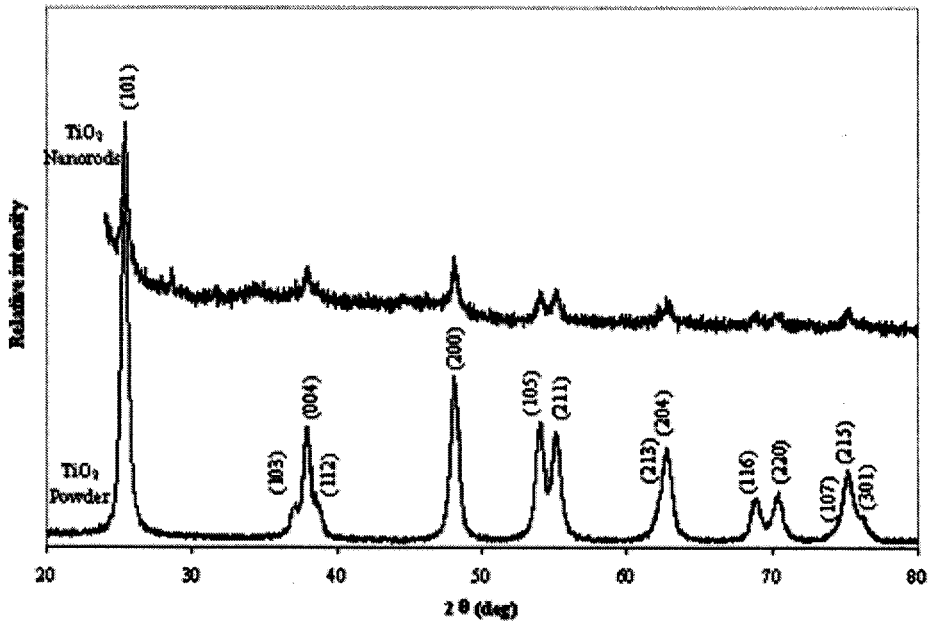

Figure 2-8 XRD spectra of both the grown TiO_2 nanorods and a powder derived from the same sol. Both samples consist of only the anatase phase, and there is no observed shift in the peak positions or relative intensities for the nanorod sample.

unidirectional alignment. The PZT nanorods grown in both the 100 nm and 200 nm membranes show a uniform diameter throughout the entire length Figure 2-9a,b), with a surface that is smooth over much or all of the length, where those grown in the 50 nm templates are less straight and parallel (Figure 2-9c). The PZT nanorods have diameters smaller than that of the pores in the template membranes, estimated by measuring several tens of nanorods on each micrograph. The PZT nanorods have a size of approximately 45 nm when grown in a PC membrane with pores of 50 nm, 70 nm when grown in a 100 nm template and 150 nm when grown in a membrane with 200 nm pores. The diameter difference of the grown nanorods and pores in the membranes could be attributed to the densification of nanorods when fired at 700 °C. However, it is not known why the samples grown in different templates show much different shrinkages, with about 25-30% shrinkage seen in the 100 and 200 nm templates, and about 10% shrinkage in the 50 nm template. The 100 and 200 nm samples shown were grown in the original experimental setup, while the 50 nm sample was grown in the revised setup, and thus the high resistance of the carbon tape working electrode may account for the lower deposit density in the earlier samples. It can be seen that all the nanorods grew through the membrane from one side to the other, and that the length of the nanorods (~ 10 μm) resembled the thickness of the membranes. Figure 2-9 also shows that PZT nanorods of uniform size and near-unidirectional alignment can be grown over a large area.

Figure 2-10 shows XRD spectra of the PZT nanorods and PZT powder prepared

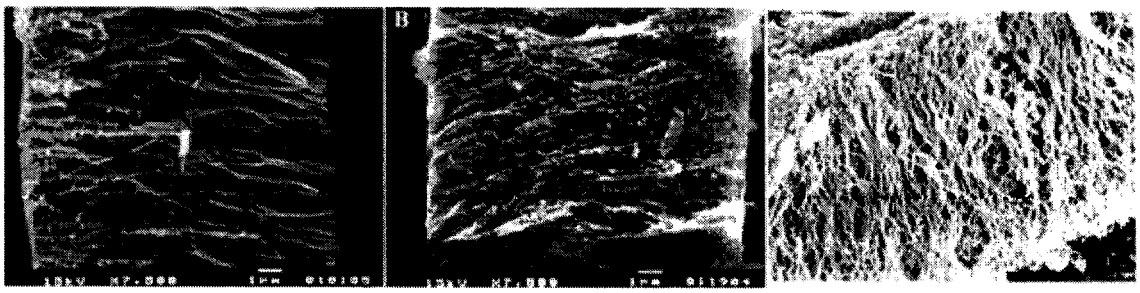

Figure 2-9 SEM micrographs of PZT nanorods. The lengths are ~10 μm, and the diameters are ~150 nm (A), ~70 nm (B) and ~45 nm (C).

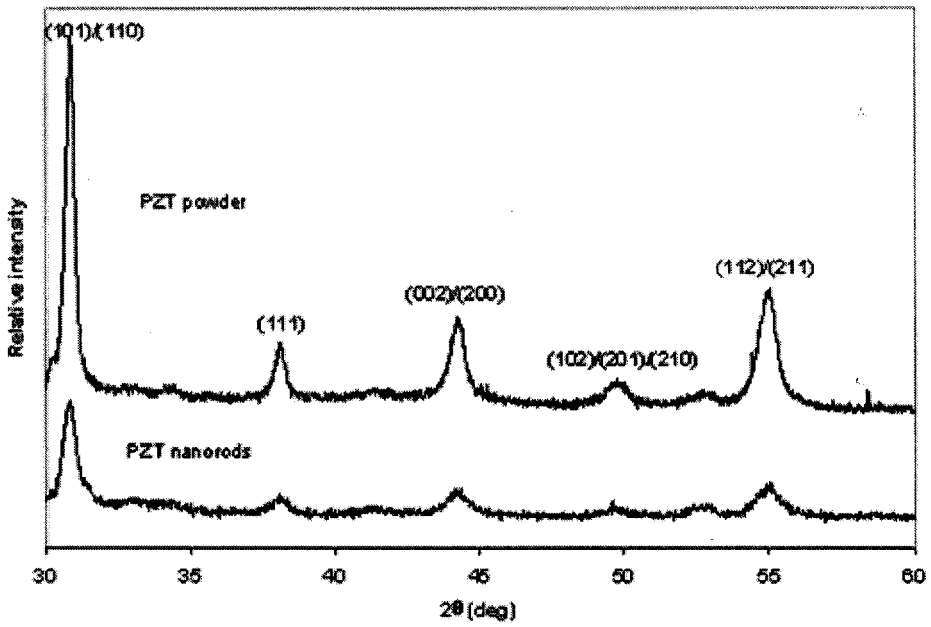

Figure 2-10 XRD spectra of both the grown PZT nanorods and a powder derived from the same sol. Both samples show only a single perovskite phase.

from the same sol by drying overnight at ~110 °C and firing at 700 °C for 1 hour; both PZT nanorods and powder consisted of only one crystalline phase, perovskite PZT without any detectable secondary phase. Comparison of the two spectra shows that there are identical peaks in both samples. Further, the peak positions are the same and the intensity ratios among various peaks are identical. The above XRD results indicate that the electrophoretic deposition has no detrimental influence on the stoichiometry and chemical compositional homogeneity that is achieved during the sol preparation. Furthermore, there is no preferred orientation of the crystals in the PZT nanorods.

2.4.3 ITO nanorods

Figure 2-11 shows SEM micrographs of ITO nanorods grown in 100 (A) and 200 (B) nm PC templates at 1.33 V/cm for 60 min, and fired at 600 °C for 1 hour. These samples show about 25-30% shrinkage in diameter compared to the original template

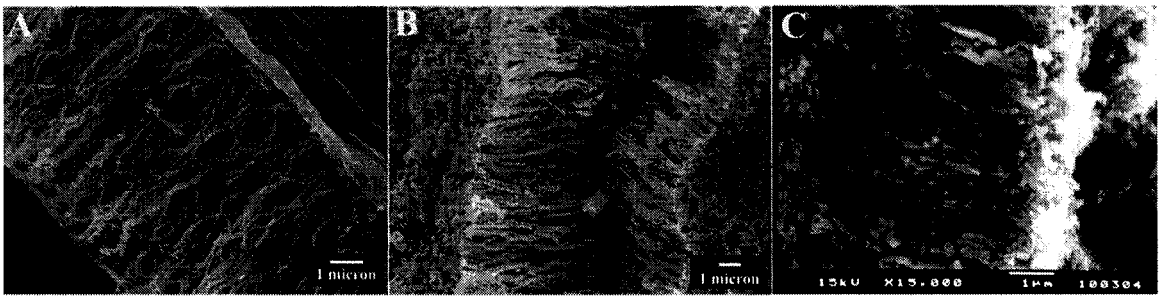

Figure 2-11 Parts A and B show SEM micrographs of nanorods of ITO grown in 100 nm (A) and 200 nm (B) templates at 1.33 V/cm for 60 min. Part C is an SEM micrograph of a sample where EPD was not used, showing poor quality nanorods.

diameter. The nanorods synthesized in this study are not straight, with a number of the nanorods exhibiting noticeable curvature. One possible explanation for this is the length of the drying step used prior to firing. It is believed that this step promotes further surface condensation reactions between the deposited nanoparticles, and is thus an important part of the nanorod synthesis. This can be seen, for example, in the growth of TiO_2 nanorods in 50 nm templates, where the morphology changes between samples dried for ~24 (discontinuous) and ~48 hrs (continuous) at 110 °C[17]. It is thus possible that a further drying time (or increase in drying temperature) could further the surface condensation, and thus yield straighter rods.

To understand the importance of EPD on the growth of the ITO nanorods, samples were also prepared without electrophoresis, by simply immersing the 200 nm PC template into the sol for the growth time of 1 hour. Figure 2-11C shows an SEM micrograph of such a sample. It can be seen in this image that the result of the growth without EPD is a low yield of short, broken hollow nanorods. This is expected, given the expected mechanism of growth when using sol EPD.

Figure 2-12 shows XRD spectra of ITO powder and ITO nanorods in an AAM template, prepared from the same sol. Both nanorods and powder comprise one crystalline phase, cubic In_2O_3. There is, however, a peak in the nanorod sample that does not belong to ITO, or any tin or indium oxides, but may be from the alumina template. Comparison of the two spectra shows that there are identical peaks in both samples. Similar to PZT, these XRD results indicate that the electrophoretic deposition

has no detrimental influence on the stoichiometry and chemical compositional homogeneity that is achieved during the sol preparation.

Figure 2-13A shows a bright-field TEM micrograph of a single ITO nanorod grown in 100 nm PC template at 1.33 V/cm for 1 hour. From this image, one can see that the nanorod has a mostly smooth surface, but that there are some small fluctuations on the sides of the rod. The selected area diffraction pattern (Figure 2-13B) of one nanorod shows a ring pattern typical of a polycrystalline nanorod. A dark-field TEM image (Figure 2-13C) shows the presence of very small crystallites, ~2-5 nm in size. This is somewhat smaller than the grain sizes determined from XRD line broadening, which show an average crystallite size of ~25 nm in the nanorods. This is not surprising, as ITO has been found with a "grain-subgrain structure", where the smaller subgrains are about twenty times smaller than the grains[18]. XRD line broadening is also

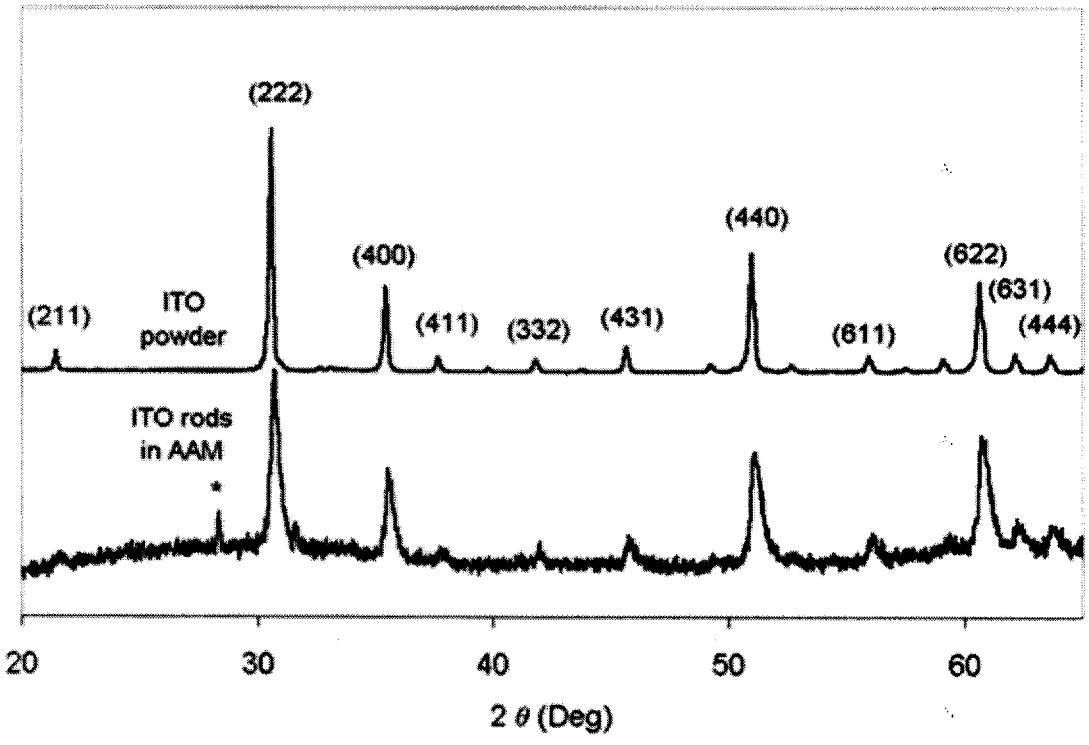

Figure 2-12 XRD patterns for ITO powders and nanorods (in AAM) fired in air at 700 °C for 1 hour. The peak marked * does not belong to ITO, or any tin or indium oxides, but may be from the alumina template.

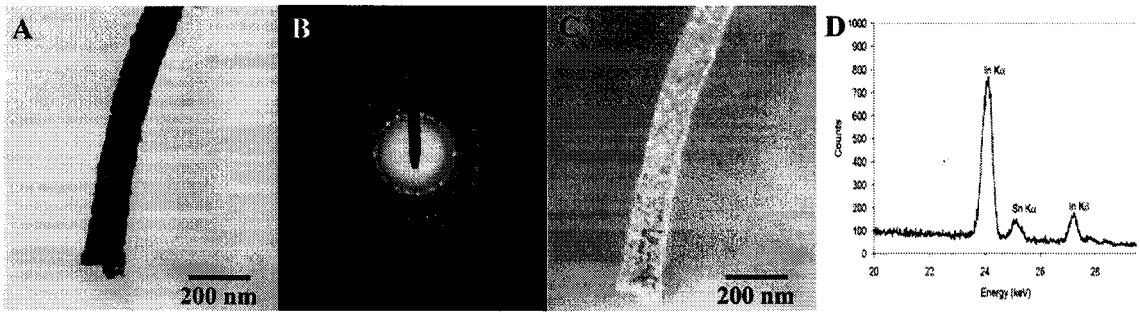

Figure 2-13 A single ITO nanorod grown in 100 nm PC template at 1.33 V/cm for 1 hour. Part A shows a bright-field TEM micrograph. Part B is an electron diffraction pattern from that rod. Part C is a dark-field TEM micrograph, demonstrating the small crystallite size. Part D shows the EDS spectrum of a single ITO nanorod.

of limited accuracy for very fine-grained compacts due to the presence of non-uniform strains[19]. Figure 2-13D shows the recorded EDS data from a single nanorod. Both the In (24.14 keV) and Sn (25.20 keV) K_α lines[20] are clearly present, with an intensity ratio that suggests ~8 at% Sn in the In_2O_3. Sn is present in the nanorods, showing that we have successfully produced the desired, doped phase of ITO.

2.4.4 Other nanorods

Figure 2-14 a-d shows SEM micrographs of SiO_2, $BaTiO_3$, $Sr_2Nb_2O_7$ and Nb_2O_5 nanorods grown by sol-gel electrophoresis. The SiO_2 nanorods have a diameter of ~200 nm, which is the same as the template pores. Under the acidic synthesis conditions used, the silica sol should be polymeric[82,21]. Such a polymeric sol would pack densely in the template pores, and the silica would thus contain only small pores. This makes it likely that the SiO_2 nanorods were unable to densify significantly at the temperature used (500 °C).

The $BaTiO_3$ nanorods have a diameter of about 150 nm, which is about 25% smaller than the template pores. The length of the $BaTiO_3$ rods is about 10 μm, similar to the thickness of the template membrane. The $Sr_2Nb_2O_7$ nanorods have diameters of ~125 nm. This corresponds to shrinkage of about 37%, suggesting that the $Sr_2Nb_2O_7$ packed less densely than the other materials. Similar to the TiO_2 and PZT nanorods,

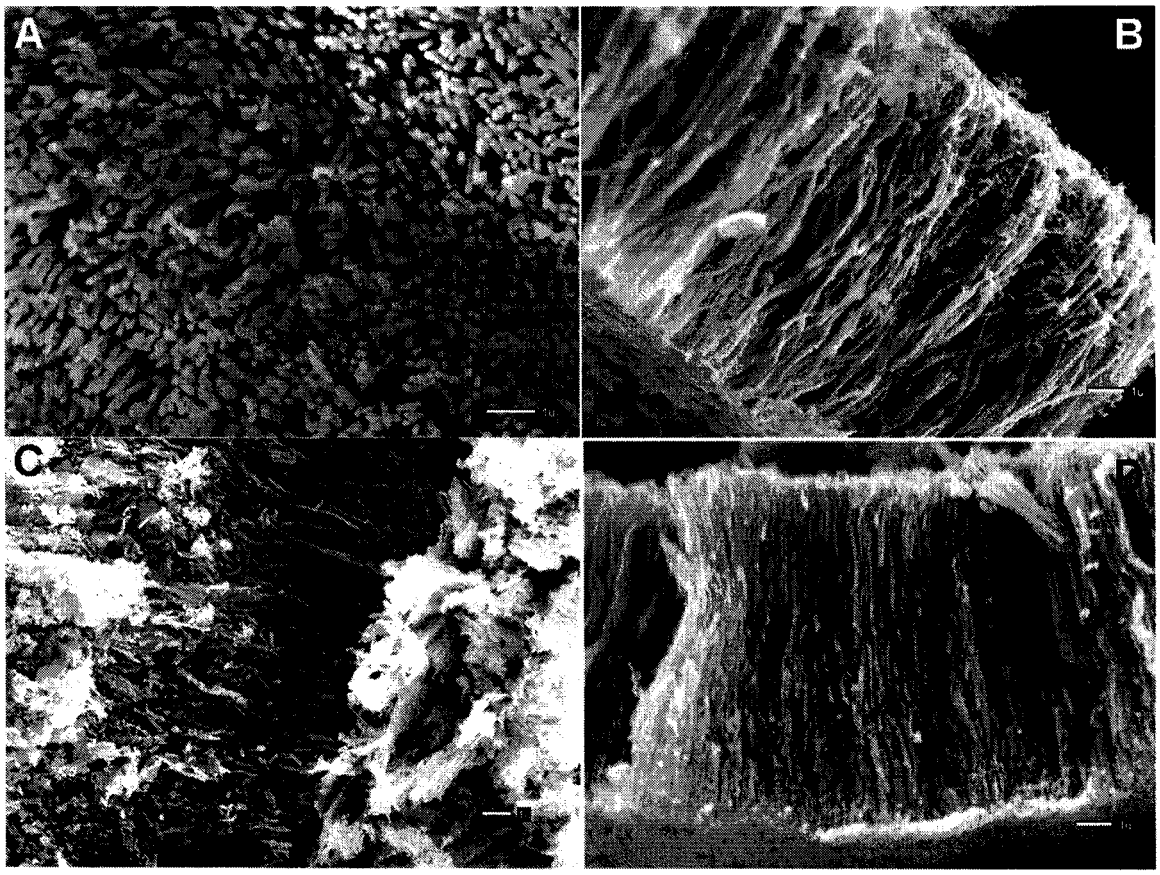

Figure 2-14 SEM micrographs of other oxide nanorods. A) SiO_2, B) $BaTiO_3$, C) $Sr_2Nb_2O_7$, D) Nb_2O_5

these nanorods all exhibit a uniform diameter throughout their entire length and have a relatively smooth surface. These images also show that the rods form over a broad area on the surface with roughly parallel alignment.

The nanorods of Nb_2O_5 that were synthesized in a 100 nm PC template were fired in air at 650 °C for 1 hour. Like the TiO_2 samples, these rods are well aligned, with a uniform orientation. Some of the nanorods appear broken, but overall the quality of this sample is quite good, and the samples show about 10% shrinkage in diameter relative to the template pores. XRD measurements on Nb_2O_5 powders made from this sol show the presence of a mixture of the orthorhombic T phase and the pseudo-hexagonal TT phase when fired at 650 °C. This is common for sol gel Nb_2O_5 samples treated at an intermediate temperature[22]. Both of these phases have attracted interest for

their electrochemical properties, with special interest in the TT phase for its electrochromic properties[23]. Powders fired at 500 °C show only the TT phase (See Figure B-2, Appendix B), and it is conceivable that nanorods fired at this temperature would also consist of only the desired TT phase.

2.4.5 Growth processes and parameters

There are a number of parameters that influence the growth of nanorods by sol EPD. Each of these must be carefully controlled in order to guarantee a successful synthesis. The main parameters discussed here include zeta potentials of the nanoparticles and the template walls, the deposition and condensation rates, and the presence of certain organic additives.

2.4.5.1 Particle zeta potential

As discussed in Chapter 1, the mobility of the sol particles is directly proportional to the particle zeta potential. Thus, it is desirable to have a sol where the pH is such that the zeta potential has a reasonably large value. If the zeta potential is too small, the rate at which the particles deposit will be too low, and the nanorod synthesis will take an inordinately long time. Additionally, the absolute sign of the zeta potential must be known, to determine on which electrode (anode or cathode) the deposition will occur.

Table 2-2 lists the approximate zeta potentials for a number of the sols used in this work. Since it is difficult to directly measure the zeta potential of such small particles, attempts were made to determine the values indirectly. Sols were allowed to gel, and the dried gels were ground into a powder. In the first method, this powder was then re-dispersed in the parent sol, and the zeta potential of these particles was determined by direct observation of the particle motion under an optical microscope. However, no motion of the particles was observed, making it impossible to determine a zeta potential. The explanation for this is uncertain, however the increased viscosity and

reduced dielectric constant of the sols (relative to water) may have reduced the particle velocity enough that they were not seen to move in the given amount of time.

In the second method, the sol powders were suspended in an aqueous solution, similar in pH and ionic strength to the parent sol. This method was successful for determining zeta potential values. Although these values are unlikely to be exactly equal to the zeta potentials of the sol nanoclusters, they are likely close enough to give good qualitative information about the behavior of the sols. It is unclear why the problem with the first method occurred. From Equation 1-3, one can see that the mobility is directly proportional to the solution dielectric constant, and inversely proportional to the viscosity. In the first method, the dielectric constant is somewhat lower, and the viscosity is somewhat higher, than for the second method. Both of these factors lead to a somewhat reduced mobility for the powders in the sol over that in aqueous solutions. It is not, however, enough to account for the total lack of motion observed.

For all the samples in this work, the zeta potentials were measured for powders in an aqueous solution, rather than in the sols themselves. While this will introduce some inaccuracies, it is not an unreasonable approximation. For instance, if one compares zeta potential data for PZT in both aqueous[24] and ethanol[25] suspensions, the same general trend is observed. In both cases, the IEP is at ~6.5-7, and the zeta potentials differ by less than 20% for most of pH range. For TiO_2, there is almost no difference in zeta potential for aqueous suspensions and mixtures of up to 30% alcohol/water[26]. Thus, while the measured zeta potentials may not exactly coincide with the actual values, they are likely close enough, and follow the same trends, to give very

Table 2-2 Zeta potentials of selected sols.

Sol	Measured zeta potential (mV)	pH
SiO_2	-8.14	3.05
TiO_2	18.85	2.07
PZT	7.63	4.08

useful information.

As the sol nanoparticles move down the template pores, they eventually approach the growth surface. While this surface is initially a second material (e.g., Al), after a short time the surface will be covered with the material being deposited. This surface is in contact with the sol, and will thus have a surface charge, just like that of the sol nanoclusters. This will lead to an electrostatic repulsion between the incoming nanoparticles and the growth surface. Additionally, there will be attractive, van der Waals forces between the particles and the growth surface. The total energy of interaction (V_t) can be thus be described as[27]:

$$V_t = V_R + V_A \qquad \textbf{Equation 2-3}$$

where V_R is the repulsive energy, and V_A is the attractive energy. One can model the energies in this system as the interaction between a sphere and a flat plate. One could also include the energy due to the constant electrophoretic force as an offset[28], making the total energy $V_t = V_R + V_A + V_{Electrophoretic}$. However, for ease of analysis, this last term will be considered separately.

Using the Hogg-Healy-Fuerstenau (HHF) formula for the interaction, and assuming that the nanoparticle and the surface have the same zeta potential, V_R can be calculated as[29]:

$$V_R(H) = 2\pi\pi_r\varepsilon_0 a\zeta^2\left\{\ln\left[\frac{1+\exp(-\kappa H)}{1-\exp(-\kappa H)}\right]+\ln[1-\exp(2\kappa H)]\right\} \qquad \textbf{Equation 2-4}$$

where H is the separation distance between the nanoparticle surface and the growth surface, $\varepsilon_r\varepsilon_0$ is the dielectric constant of the liquid medium, a is the nanoparticle radius, ζ is the zeta potential, and κ is the Debye-Hückel parameter (see Equation 1-2)[30]. Similarly, one can find the van der Waals interaction between a sphere and a plate as[31]:

$$V_A(h) = -\frac{A}{6}\left[\frac{1}{h} + \frac{1}{h+2} - \ln\left(\frac{h+2}{h}\right)\right] \qquad \textbf{Equation 2-5}$$

where h is the dimensionless separation distance ($h = H/a$) and A is Hamaker's constant. Where possible, reported values of the Hamaker constants were used (see references 32 and 33 for more information). For some of the data, however, exact values were unavailable, so that it was necessary to use approximate values. Additionally, the zeta potential values used to determine the repulsive energies are approximate values, determined by suspending the dry sol-gel powder in an aqueous solution at approximately the same pH and ionic strength. These approximations yield values of the energy barrier, which are not exact but are still helpful for suggesting the general scale of energies involved. Figure 2-15 shows a sample calculated energy barrier for the TiO_2 sol. This calculation assumes that the growing deposit has a zeta potential equal to that of the particles in the sol. This assumption is seen in the literature on electrophoretic deposition[28]. However, it is possible that due to surface conduction

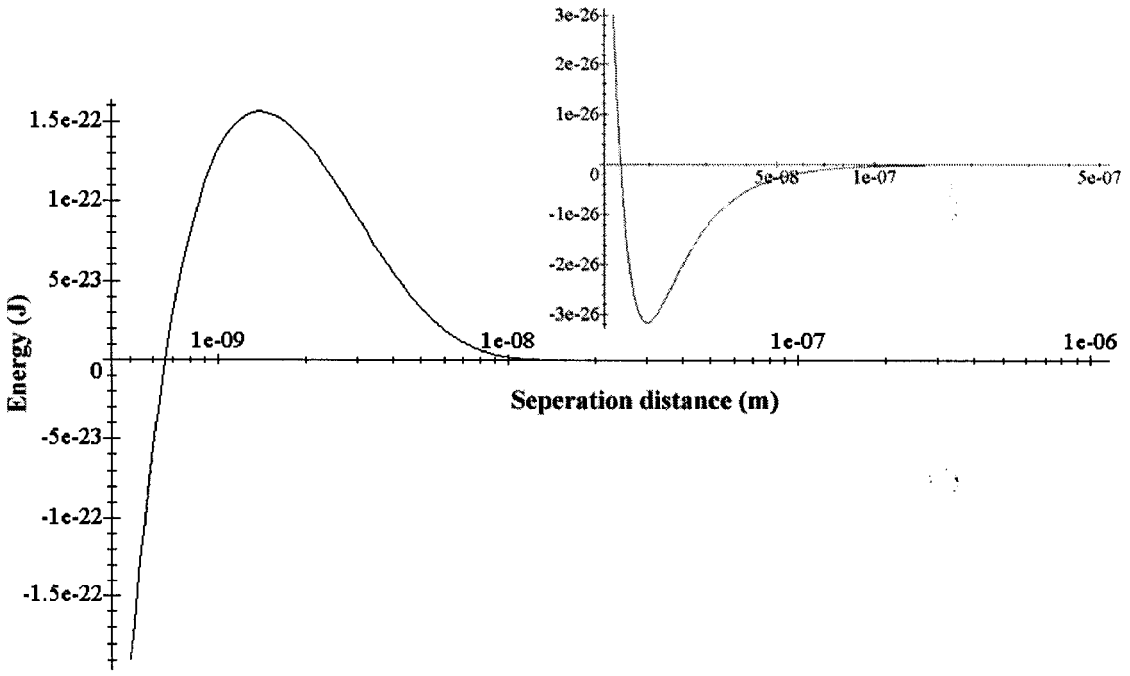

Figure 2-15 Energy barrier for TiO_2 sol particles depositing on a TiO_2 surface. Inset, magnification, showing secondary minimum.

of ions through the double layer of the porous deposit, that the effective potential of the growth surface may differ from that of the nanoparticles.

From the above equations, one can determine the height of the energy barrier for the deposition of sol nanoparticles on the growth surface. Table 2-3 lists Hamaker constants used in the energy calculations, along with approximate values of the barrier height for a number of the sols in this study. The magnitude of this value can be compared with the expected kinetic energy of the nanoparticles moving by electrophoresis. Remembering that the electrophoretic mobility of a particle is the electrophoretic velocity per unit field strength, v/E, one can see a simple explanation for this voltage dependence. Plugging the definition of μ into equation 1.3 yields:

$$v = \frac{2\varepsilon_r \varepsilon_0 \zeta E}{3\pi\eta} \qquad \textbf{Equation 2-6}$$

One can then use this velocity, along with the size and density of the nanoparticles, to determine the kinetic energy of the moving clusters. Values for a few representative sols are also listed in Table 2-3. The heights of the energy barriers are, in general, many orders of magnitudes larger than the kinetic energies of the nanoparticles. The values of barrier height are all smaller in magnitude than the thermal energy of the particles ($kT \approx 4.4 \times 10^{-20}$ J at room temperature). This is reasonable, given that the sols all will

Table 2-3 Hamaker constants and energies for selected sol systems.

Material	A_{11} (x 10^{-20}J) [source]	A_{33} (x 10^{-20}J) [source]	A (calculated) (x 10^{-20}J)	Height of Energy Barrier (x 10^{-22} J)	Kinetic Energy from Electrophoresis (x 10^{-38} J)
TiO_2	14.3 [32]	5[33][1]	1.29	1.56	7.54
SiO_2	6.50 [32]	5[33]1	0.053	0.63	0.69
PZT	15 [33][2]	5[33]1	1.45	0.71	1.93

[1] This is an average value for organic solvents

[2] This is an average value for oxides

eventually gel at room temperature, so the thermal energy at room temperature must be sufficient for the particles to overcome the barrier eventually. If not for the viscous drag of the fluid, the charged particle would have kinetic energy on the order of the energy barrier due to the field. The drag, however, slows down the particles significantly. This suggests, then, that the real effect of electrophoresis is not to directly overcome the energy barrier, but to simply enrich the growth species near the deposition surface (since the electric field can bring the particles to within a few tens of nanometers of the surface), where thermal energy brings the particles together.

Zeta potential also give a potential explanation for some of the failed nanorod systems, in that the sols in question were stable at a pH value that was very near the sol's IEP. In a typical colloid, the charge on the particles is quite small near the IEP. Since particle charge directly effects the mobility (as shown in equation 1.3), there would be low sol mobility near the IEP, thus making it difficult to form nanorods, due to the very slow rate at which the particles would move to the growth surface. This is especially likely for WO_3 sols, as WO_3 has an IEP of about pH = 0.3-0.5[34,35]. All the WO_3 sols studied were highly acidic, with a pH below 1, but they were likely not acidic enough to give a sufficiently large zeta potential. Similar effects were seen in selected Nb_2O_5, V_2O_5 and ZnO sols, all of which were stable near the IEP (pH = 4.1[35], 2[36] and 9-10[35] respectively) and did not form nanorods. Not all sols with a pH near the IEP fail to yield nanorods, however. For the SiO_2 sol, the pH is only slightly above the typical reported IEP of silica. However, the particles still seem to have a zeta potential of about 8 mV, which would likely be large enough for successful formation of nanorods.

2.4.5.2 Template zeta potential

In all of the discussion of thus far of the electrophoretic growth process, there has been no mention of the possibility of an influence on the growth due to the template. The template has been treated as a simple (neutral) physical barrier. Just as the sol particle will develop a surface charge when in contact with the polar solvent, however, so can the templates have an associated surface charge. It is possible that the sign and magnitude of this surface charge could have an influence on the growth of the oxide

nanorods. Wang et al[37] suggested that having a template surface charge of the same sign as the particle charge is necessary for the formation of solid nanorods over hollow nanotubes. Martin et al[80] have observed the preferential formation of TiO_2 nanotubes under conditions where the TiO_2 particles are positively charged and the pore walls are assumed to be negatively charged. It is assumed that electrostatic attraction between the oppositely charged species leads to an initiation of gelation at the pore walls.

This may explain some of the difficulties that have been experienced in synthesizing nanorods. The PC membranes used in synthesizing nanorods have their isoelectic point (IEP) at about pH ~4[38,39], and thus have a positive surface charge at pHs below this value. Since all of the sols discussed above have pHs at or below 4, it is expected that growth will proceed as Wang et al proposed[37]. Attempts thus far to grow nanorods from sols with higher pHs have, however, been unsuccessful. Specifically, ZnO nanorods have been attempted from sols with pH's around 9. In these circumstances, the ZnO particles are positive, but the PC pore walls are negative. A possible explanation for the failure to grow nanorods under these conditions is that electrostatic attraction between the ZnO particles and the pore walls caused the pore openings to become blocked, preventing nanorod growth. Two possible ways to overcome this are to 1) try increasing the voltage to overcome this attraction; or 2) to use a ZnO sol with a slightly higher pH, so that the ZnO particles will also be negatively charged. This also does not account for the ability to grow SiO_2 nanorods, since the particles in that sol are negatively charged.

Figure 2-16 shows SEM micrographs of SiO_2 nanorods grown in 200 nm PC templates with the working electrode as either the cathode or the anode, or with no applied voltage at all. What one sees is that placing the template on the anode leads to formation of solid nanorods. This is understandable, as the SiO_2 particles are negatively charged at the pH used. When the template is placed in the sol without an applied voltage, hollow SiO_2 nanotubes are formed. This is likely from the electrostatic attraction between the negative SiO_2 particles and the positively charged pore walls, similar to the TiO_2 nanotubes seen by Martin et al[80]. Lastly, if the template is placed on the cathode, hollow tubes are seen, similar to those without an applied voltage. This is

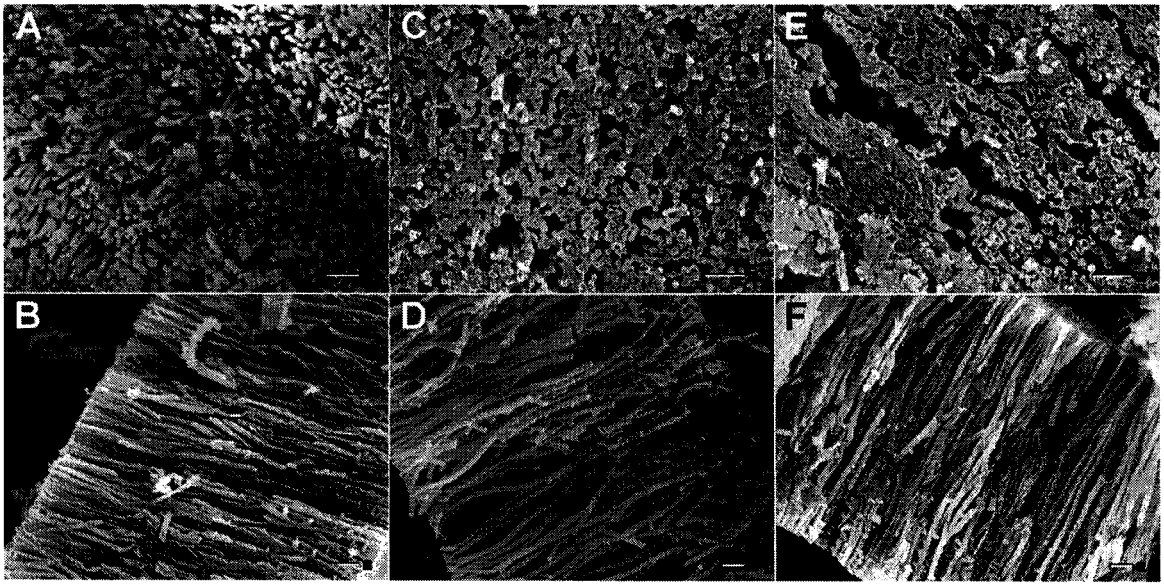

Figure 2-16 SiO_2 nanorods grown at the anode (A, B); without applied voltage (C,D) and at the cathode (E,F). The nanorods grown at the anode are solid, while the other two are hollow. All samples were grown for 1 hr in 200 nm templates.

somewhat surprising, as it would be expected that the negative sol particles would move away from the cathode under an applied voltage. Although theses two samples appear identical in cross-section, when viewed along their length one observes that those grown without applied voltage are longer and more regular than those grown at the cathode are. To look at this effect, the zeta potentials of the templates were estimated as in the proceeding section.

Table 2-4 lists the approximate zeta potentials for two types of membranes (200 nm PC, and AAM), each in three different sols. These values were measured by chopping/crushing the membranes and dispersing them in the sols, then observing the velocities of the membrane particles under an applied field with an optical microscope. Strictly speaking, this method measures the zeta potential of the outside surface of the membrane, not that of the pore walls. Although it is possible that these values differ, streaming potential measurements with PC membranes show that the two values are typically quite similar[39], at least for membranes with 100-200 nm pores. The data measured for AAM samples show reasonable agreement with reports from the

Table 2-4 Selected template zeta potentials.

Membrane	Zeta potential (mV) at pH = 2.0	Zeta potential (mV) at pH = 3.0	Zeta potential (mV) at pH = 4.0
PC	21.90	17.74	-7.12
AAM	33.70	28.57	16.61

literature[40], shown in Figure 2-17. The literature values in this figure are an average for AAM samples formed at several different current densities, in two different electrolytes. While these values do not exactly correlate with those measured, they do show the same general trend and order of magnitude. Thus, the measured values for AAM zeta potential are likely quite close to the actual values. Similarly, the PC values are also quite close to those reported in the literature[39].

In most cases, the templates used have a positive surface charge, except for PZT grown in PC. For all successful sols except SiO_2 and PZT in PC, this means that there would be an electrostatic repulsion between the positively charged nanoparticles and the pore walls, which should aid the formation of solid nanorods. For SiO_2, the

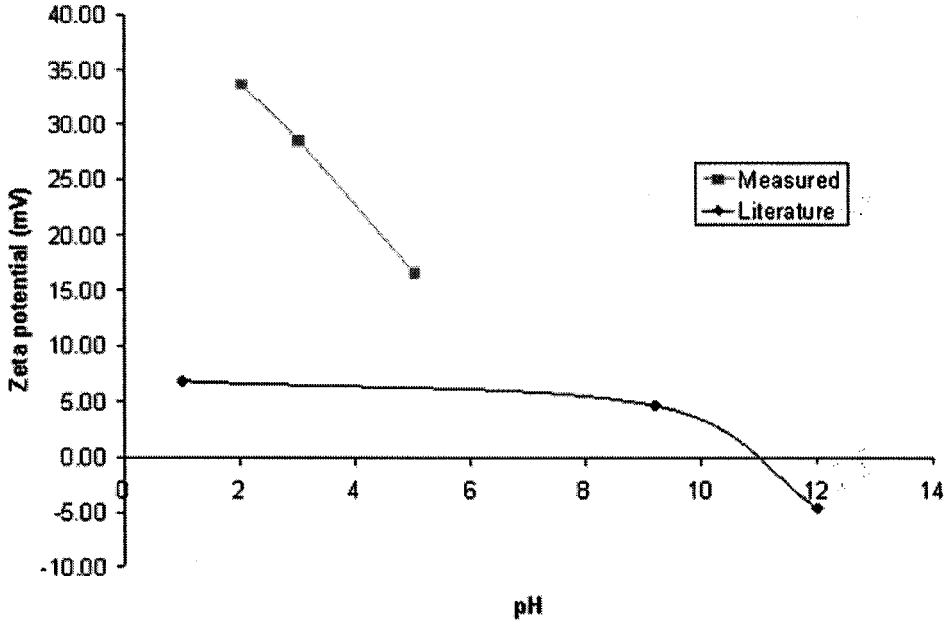

Figure 2-17 Measured vs. reported zeta potentials

nanoparticles are negatively charged and attracted to the pore walls, explaining the hollow rods observed when no electric field is applied. When the appropriate field is applied, however, solid rods are obtained in both SiO_2 and PZT, showing the effectiveness of EPD for formation of dense deposits.

2.4.5.3 Deposition rate

For the growth of the oxide nanorods by electrophoresis, one would expect that the applied voltage for growth will have a significant influence on the product synthesized. According to Equation 2-6, the velocity of the particles (and thus the deposition rate) is proportional to the electric field. Thus, at smaller applied voltages, one would expect slower growth rates, and at higher voltages, the particles may be moving too quickly to form high-quality nanorods.

There are three competing processes that can affect the quality of the deposited nanorods: 1) rate of arrival of nanoparticles at the growth surface; 2) the re-arrangement of the particles to positions of lower free energy; and 3) the rate of condensation reactions between the particles (described in detail in the next section). As the moving nanoparticles arrive at the growth surface, they need some finite time to transport to a location of lower energy. If the applied filed is too high, then the nanoparticles arrive at a faster rate than they re-arrange on the surface, causing them to become locked into position and reducing the quality of the deposit.

Another possibility is the separation by size of nanoparticles under the applied field. If there is a distribution is nanoparticles sizes present in the sol, then there will be a distribution in the velocities of the particles, according to Equation 2-6. This effect would become more pronounced at higher fields, leading to greater differences in deposition rate for small vs. large particles. The influence of field can be seen, for example, in the growth of PZT nanorods in 50 nm templates, shown in Figure 2-18.

When the rods were grown at with 5 V applied voltage (Figure 2-18a, also Figure 2-9c), the nanorods formed were continuous. Upon increasing the voltage to 7 V,

however, (Figure 2-18b) the products are no longer solid nanorods, but strings of small, spherical particles.

Further understanding of the effects of deposition rate on the density and quality of the nanorods comes from analyzing samples of TiO_2 formed at a number of field strengths. In both the 100 and 200 nm templates, the size of the sintered nanorods seems to increase slightly with increasing deposition field, but the overall effect is slight. This is demonstrated in Figure 2-19. However, the quality of the rods is seen to vary. For TiO_2 rods formed at 1.84 V/cm in 100 nm templates, the result is a mat of short broken rods, rather than the nice parallel array seen at higher fields. This same behavior occurs in 200 nm templates without EPD and at a field of 0.17 V/cm. Additionally, the yield of rods under no applied field is very low. Thus, we find that if the deposition rate is slow with respect to the condensation rate, then increasing field increases the deposit density. However, if the deposition is faster than the condensation rate, one would expect a less dense deposit.

2.4.5.4 Condensation rate

When sol particles come within close contact, there are two important forces to consider. First, there is a van der Waals attraction between the two particles, holding them in close proximity. This attraction only holds the two particles in physical contact; it does not prevent re-arrangement of the relative positions of the two particles. Thus, even after two particles touch, they may still be able to re-arrange their relative positions to minimize the free energy of the system. Secondly, there is the possibility of condensation reactions occurring between the two nanoclusters. As exposed –OH groups on the nanoclusters surfaces come in contact, these reactions will generate covalent bonds between the two nanoparticles, locking them in place. The rate of these condensation reactions is an important consideration in the synthesis of nanorods. It is necessary to have enough condensation to hold the shape of the nanorods, but a slow enough rate that the particles can re-arrange themselves rather than just sticking wherever they land.

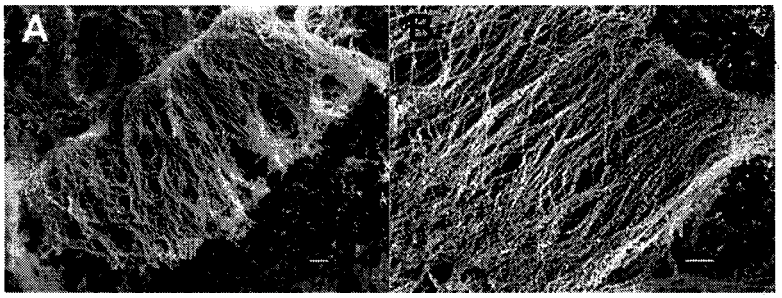

Figure 2-18 PZT nanorods grown at lower (A) and higher (B) voltages. At the higher voltage, the rods become discontinuous.

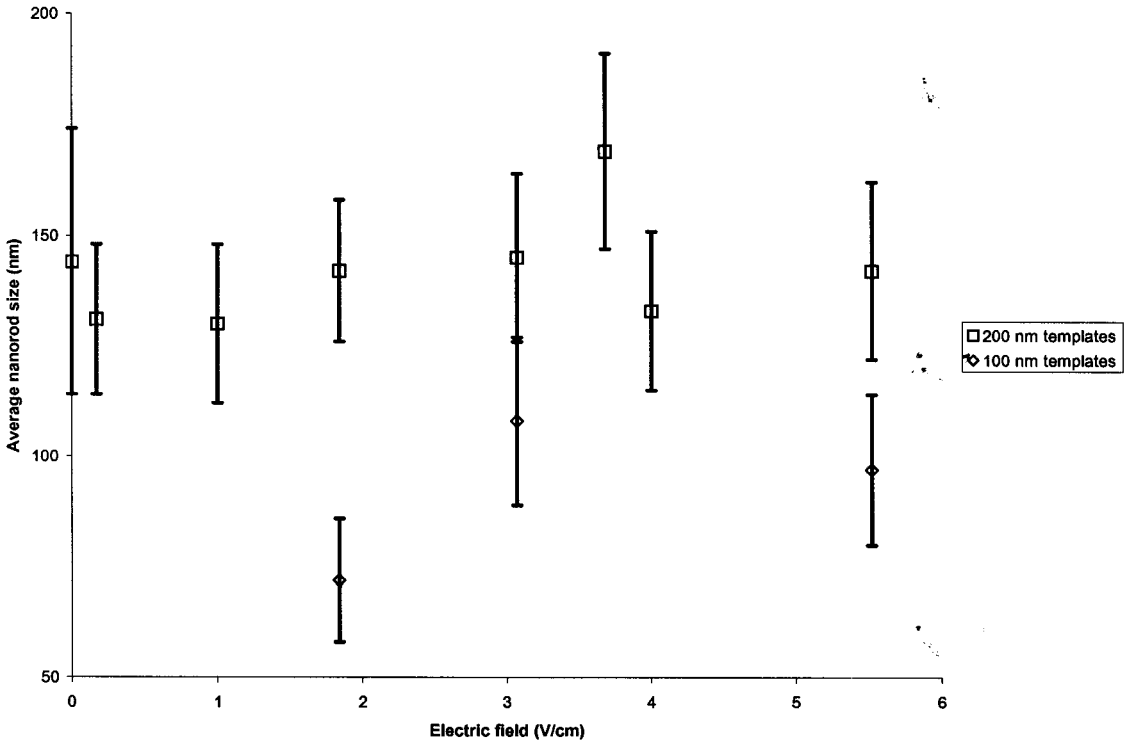

Figure 2-19 TiO_2 nanorod diameter vs. electric field.

In order to observe the effects of condensation rate on the synthesis of nanorods, TiO_2 sols were prepared with a variety of pHs. First, TiO_2 sol was synthesized as discussed previously. After the stable sol was formed, the pH was adjusted by the addition of concentrated nitric acid. This was done after a stable sol was formed, so as to have a minimal impact on the hydrolysis and formation of initial nanoparticles. To demonstrate the effect that pH adjustments have on the sols, and since gelation time is a good indicator of the condensation rate, gelation times were measured for a number of pHs. Figure 2-20 shows the approximate gelation time of the TiO_2 sols as a function of the pH. From this, one can see that the gelation kinetics are clearly influenced by the sol pH, especially at very low pH values. TiO_2 nanorods were synthesized from varied pH sols, as described above. Figure 2-21 shows samples of TiO_2 rods grown from sols with a pH of 0.3 and 1.67. The nanorods grown from the sol with pH = 0.3 have a much rougher surface morphology, and a large number of broken

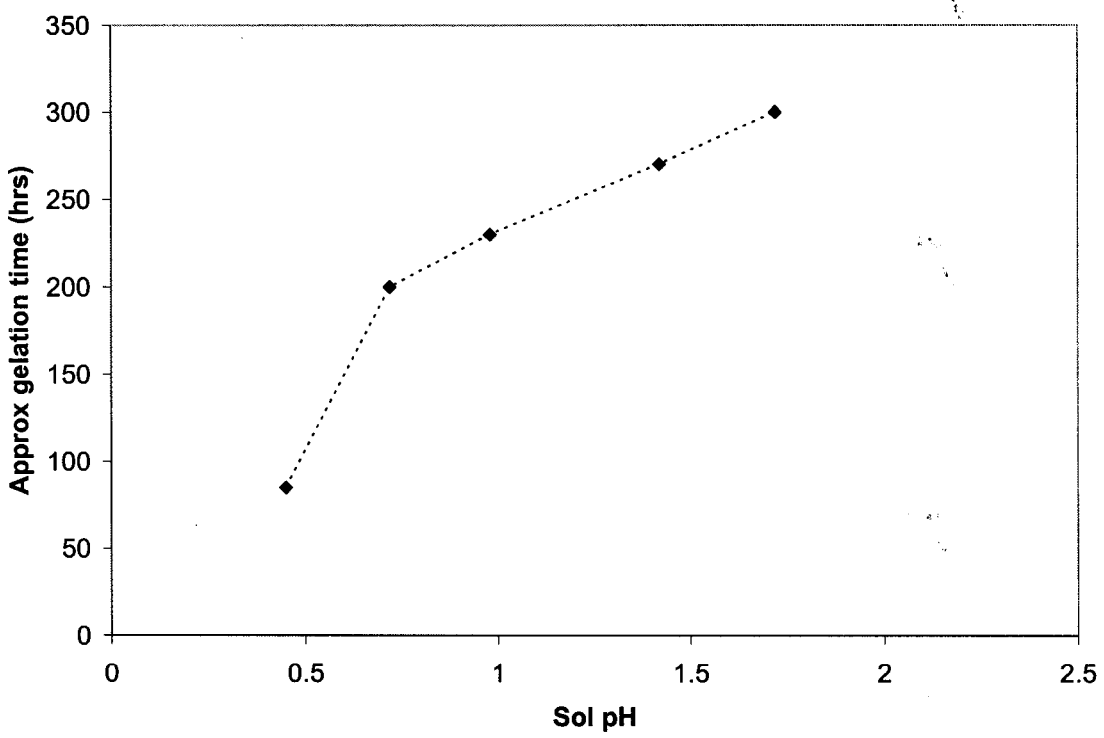

Figure 2-20 Gelation time vs. sol pH for TiO_2 sols.

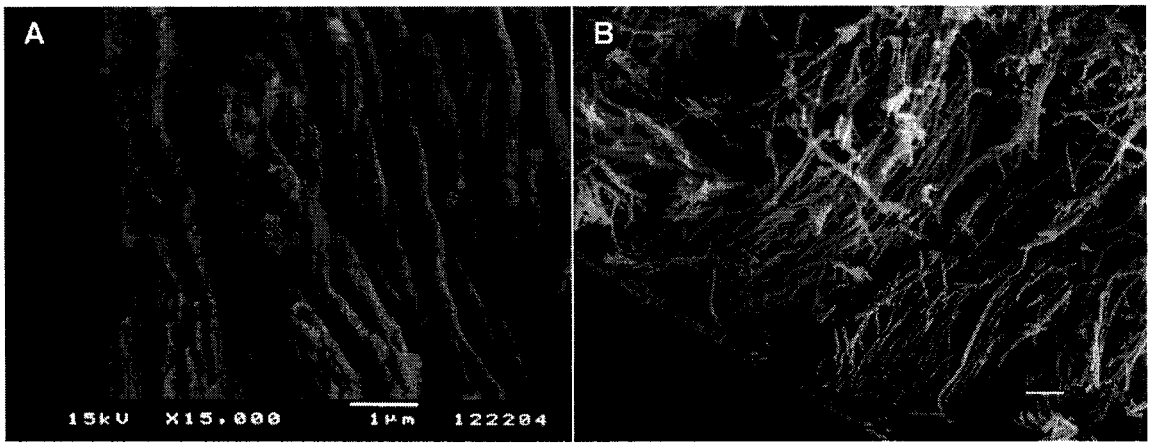

Figure 2-21 TiO_2 nanorods grown from sols with a pH of 0.3 (A) and 1.67(B).

rods this could be explained by the increased condensation rate of the lower pH sol. As the depositing nanoparticles arrive at the growth surface, a faster condensation rate causes the particles to be incorporated into the deposit much more quickly, without time to rearrange into a more favorable position. This could cause greater variations in the morphology, and lead to pores that would cause the rods to crack upon firing. However, the influence of pH is not strictly limited to effects on condensation rate. The sol pH also changes the zeta potential of the sol nanoparticles, and thus their mobility. That is, lowering pH leads to an increase in both deposition rate and condensation rate. Since the relative strength of these two factors is not known for this sol, it is difficult to say with certainty which factor of this combined influence dominates.

2.4.5.5 Chemical additives

The use of various organic additives to increase the stability of sols is well known, and these types of additives have become ubiquitous in sol preparation. In general, they work by binding to the precursors or nanoclusters in such a way as to slow down or prevent condensation reactions[41]. This is highly advantageous, and leads to the ability, for instance, to form stable sols even from highly reactive precursors. An

example is the use of glacial acetic acid to stabilize TiO_2 sols. Direct addition of water to titanium alkoxides generally forms precipitates, but the use of acetic acid in this system leads to stable sols[42].

Such a slowed or stopped rate of condensation reactions is undesirable in the formation of nanorods. Surface condensation reactions are believed to be critical to the formation nanorods, by forming a stronger green body prior to firing. This has been seen, for example, in TiO_2 rods grown in a 50 nm template. It is believed that this effect is behind the inability of certain tested sols to form nanorods. Table 2-5 shows a number of the sol compositions that failed to succeed in forming nanorods, along with the possible reason.

2,4-pentanedione (also known as acetylacetone, or AcAc) is a very common additive in sol processing, and has long been used to prevent precipitation of undesired phases from highly reactive precursors[43], control crystal structure[44], and aid in the formation of single-phase complex oxides[45]. It is also present in a number of the sols that failed to yield nanorods.

Table 2-5 Systems in which nanorods were not synthesized

Sol	Observation	Possible reason(s)
Nb_2O_5 (1)	No rods	pH near IEP. Acetic acid
Nb_2O_5 (2)	No rods	Acetic Acid
Nb_2O_5 (3)	No rods	Acetylacetone
V_2O_5	No rods	pH near IEP. Acetylacetone in some sols.
ITO	No rods	Acetylacetone is the main solvent
ZrO_2	Hollow (w and w/o EPD)	Uncertain
ZnO (1)	No rods	pH near IEP. DEA
ZnO (2)	No rods	Acetic acid
ZnO (3)	No rods	Uncertain, colloid pH well below IEP
WO_3 (1)	No rods	pH near IEP. Acetylacetone
WO_3 (2)	No rods	pH near IEP. Acetic acid

It is quite likely that the use of AcAc is responsible for this failure. It is widely known that AcAc binds strongly to a number of sol-gel precursors, such as $Ti(OPr^i)_4$[41,46] and $Zr(OPr^n)_4$[47,48], and is often incompletely hydrolyzed even in the presence of a large excess of water. This in turn inhibits condensation reactions and greatly slows the formation of a complete gel network. As mentioned above, this would likely inhibit the formation of nanorods from such as sol.

To demonstrate that AcAc can inhibit nanorod formation, the following two experiments were performed. A sol that does yield nanorods (TiO_2) was modified in one of two ways, by either adding AcAc (in a ratio of Ti:AcAc = 1:1) before hydrolysis (TiO_2-AcAc1) or well after hydrolysis to the final stable sol (TiO_2-AcAc2). Both sols were then used in the template EPD setup as previously described. In both cases, only a few isolated shorter nanorods were observed, as seen in Figure 2-22. This is contrasted with the large arrays of nanorods seen when AcAc is omitted (as in Figure 2-6). This suggests that AcAc inhibits nanorod formation. A possible explanation of the failure to form nanorods may be related to the observed suppression of gelation in AcAc modified TiO_2 sols. As discussed above, the standard TiO_2 sol used in this work gels after about 300 hours at room temperature. However, both TiO_2-AcAc1 and TiO_2-AcAc2 sols are stable at room temperature for over 6 months, suggesting that the AcAc addition has a strong effect on the condensation rate of the sol.

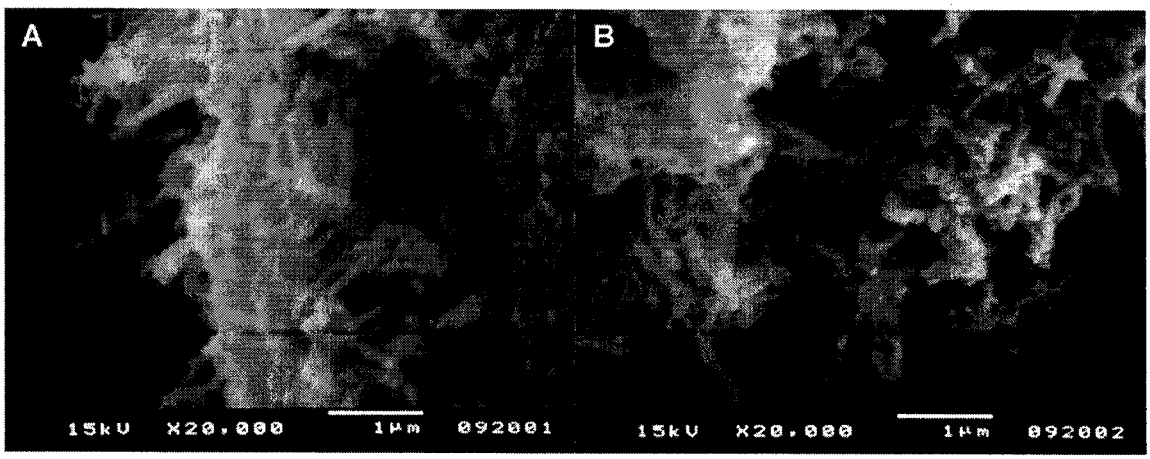

Figure 2-22 TiO_2 nanorods grown with AcAc added to the sol before (A) and after (B) hydrolysis.

While the evidence supports the idea that AcAc is detrimental to the formation of nanorods by sol EPD, further evidence would be useful. Such evidence could come from knowledge of the molecular structures present after AcAc addition, hydrolysis, or condensation. One could go about obtaining such information two ways. One way is through calculation, using the partial charge model[49] to determine the most likely molecular structure.

The partial charge model is based on the idea that within a molecule, the electronegativities of atoms will tend to equalize[49]. In order for this to happen, the atoms in the molecule will develop partial charges, represented as $\delta(G)$, where G is the unit on which the partial charge resides (metal atom, ligand, etc.). By calculating the partial charges for the various possible transition states and products of reactions, one can determine which groups will be removed (typically those with the largest positive partial charge).

However, these calculations can be quite difficult for multi-component systems, so a simplified example is presented. Titanium isopropoxide ($Ti(OPr^i)_4$) is very reactive towards chemical modification by both glacial acetic acid (HOAc) and acetylacetone (AcAcH). When mixed with either reactant, an isoporopanol group is easily liberated ($\delta(Pr^iOH) = 0.12, 0.11$ for reactions with HOAc and AcAcH, respectively). A second isopropoxy group can also be easily replaced, yielding precursors such as $Ti(OPr^i)_2(OAc)_2$ and $Ti(OPr^i)_2(OAc)(AcAc)$. Beyond two substituents, further chemical modification generally does not take place[48,50], leaving $Ti(OPr^i)_2(OAc)(AcAc)$ as the likely precursor in sol TiO_2-AcAc1. Table 2-6 lists calculated charge distributions for some titanium precursor modification, hydrolysis and condensation reactions.

Upon hydrolysis of the $Ti(OPri)_2(OAc)(AcAc)$ precursor, isopropanol is again easily removed ($\delta(PriOH) = 0.38$). Such $Ti(OPri)(OAc)(AcAc)(OH)$ molecules are likely to undergo condensation reactions not by the elimination of water, but by elimination of isopropanol ($\delta(PriOH) = 0.52$, $\delta(HOAc) = -0.43$, $\delta(AcAcH) = -0.04$, $\delta(H_2O) = -0.16$). This suggests that condensation reactions between the formed nanoparticles will be limited, since there is only one isopropoxy group per precursor.

Table 2-6 Selected partial charge calculations for modified TiO_2 sols.

Species	δ(Ti)	δ(Pr^iOH)	δ(HOAc)	δ(AcAcH)	δ(H_2O)
$Ti(OPr^i)_4$·(HOAc)	0.63	0.12	-0.69		
$Ti(OPr^i)_4$· (HAcAc)	0.63	0.11		-0.54	
$Ti(OPr^i)_3(OAc)$· (HOAc)	0.66	0.32	-0.56		
$Ti(OPr^i)_3(OAc)$· (HAcAc)	0.65	0.26	-0.60	-0.35	
$Ti(OPr^i)_3(AcAc)$· (HOAc)	0.65	0.26	-0.60	-0.35	
$Ti(OPr^i)_2(OAc)_2$· (HOAc)	0.68				
$Ti(OPr^i)_2(OAc)_2$· (HAcAc)	0.67				
$Ti(OPr^i)_2(OAc)(AcAc)$· (HOAc)	0.66				
$Ti(OPr^i)_2(OAc)_2$· (H_2O)	0.67	0.48	-0.46		-0.17
$Ti(OPr^i)_2(OAc)(AcAc)$· (H_2O)	0.66	0.38	-0.52	-0.20	-0.19
2 $Ti(OPr^i)(OAc)(AcAc)(OH)$	0.68	0.52	-0.43	-0.04	-0.16

These limited condensation reactions could be the reason that nanorods were not successfully formed in the AcAc-containing solutions.

Results from UV-vis absorbance spectra also give information about the effect of AcAc in the TiO_2 sol. Figure 2-23 shows absorbance spectra of both the standard TiO_2 sol, along with the two different AcAc-modified sols (TiO_2-AcAc1 and TiO_2-AcAc2). In the standard sol, there is an absorbance peak at about ~388 nm, likely due to the band-gap of the semi-crystalline TiO_2 nanoparticles in the sol. In the AcAc-modified sols, however, there is a strong absorbance band in the visible, at about ~475 nm. This is not surprising, as transition metals chelated with acetylacetone typically show a strong visible or UV absorbance peak. Depending on the solvent and the exact ion chelated, the absorbance maximum can be anywhere from ~240-810 nm[51,52,53]. For example, V^{4+} chelates (in the form of $VO(acac)_2$) have three absorption bands, with the primary feature ~400 nm[53,54,55]. While there is no data available in the literature about the absorbance of Ti^{4+}-acac chelates, it is not unreasonable to expect that they, like the other transition ions mentioned, would have a strong visible absorbance. This is likely the

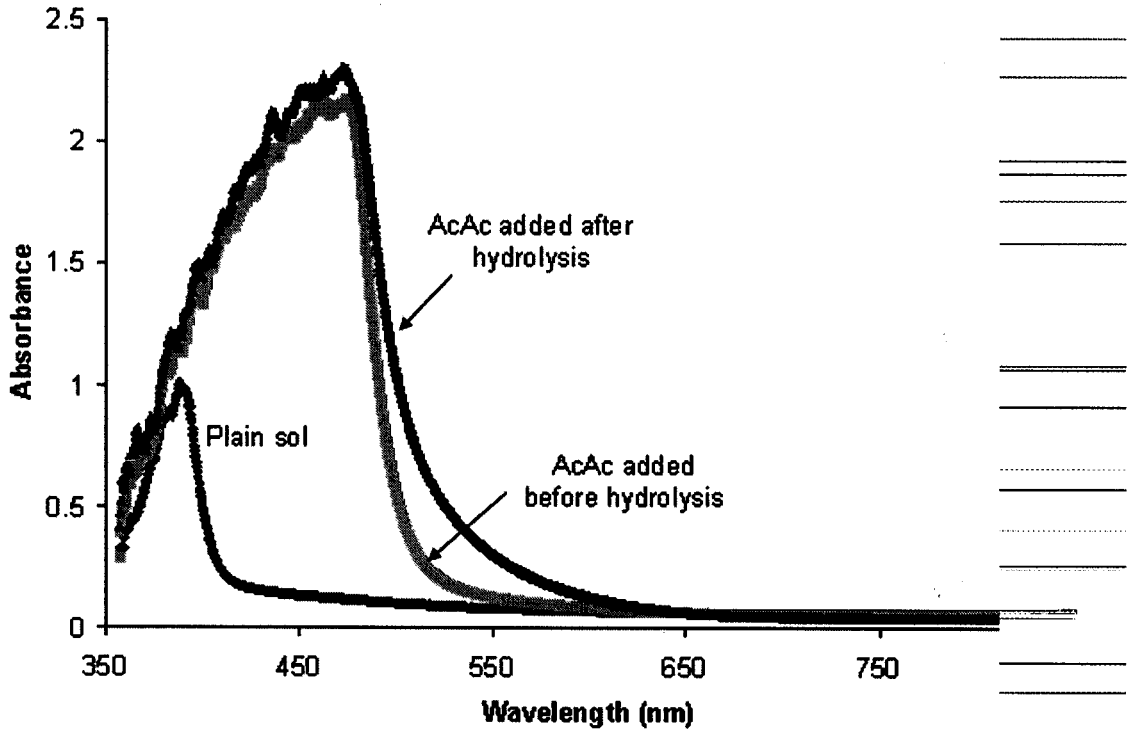

Figure 2-23 UV-Vis absorbance of plain and acac-modified TiO_2 sols

source of the feature seen in Figure 2-23. Thus, the AcAc remains strongly bound to the Ti species, even after hydrolysis.

A final method to observe the influence of AcAc in the TiO_2 sol is FTIR spectroscopy. A drop of each of the two AcAc modified TiO_2 sols was placed between two KBr windows for measurement, and transmission spectra were recorded between 4000 and 200 cm^{-1}. Figure 2-24 shows a sample spectrum recorded for sol TiO_2-AcAc1. By comparing the peaks observed with reports in the literature, we can determine the species present in the sol, and in some cases, their configuration. The spectrum is quite complex, due to the large number of species present in the sol. However, there are a few features of particular interest. The peaks at 1590 (ν(C-O)) and 1534 (ν(C-C)) cm^{-1} are indicative of metal-acac complexes[56], showing that the AcAc is not fully hydrolyzed. Similar results were observed for the other sol.

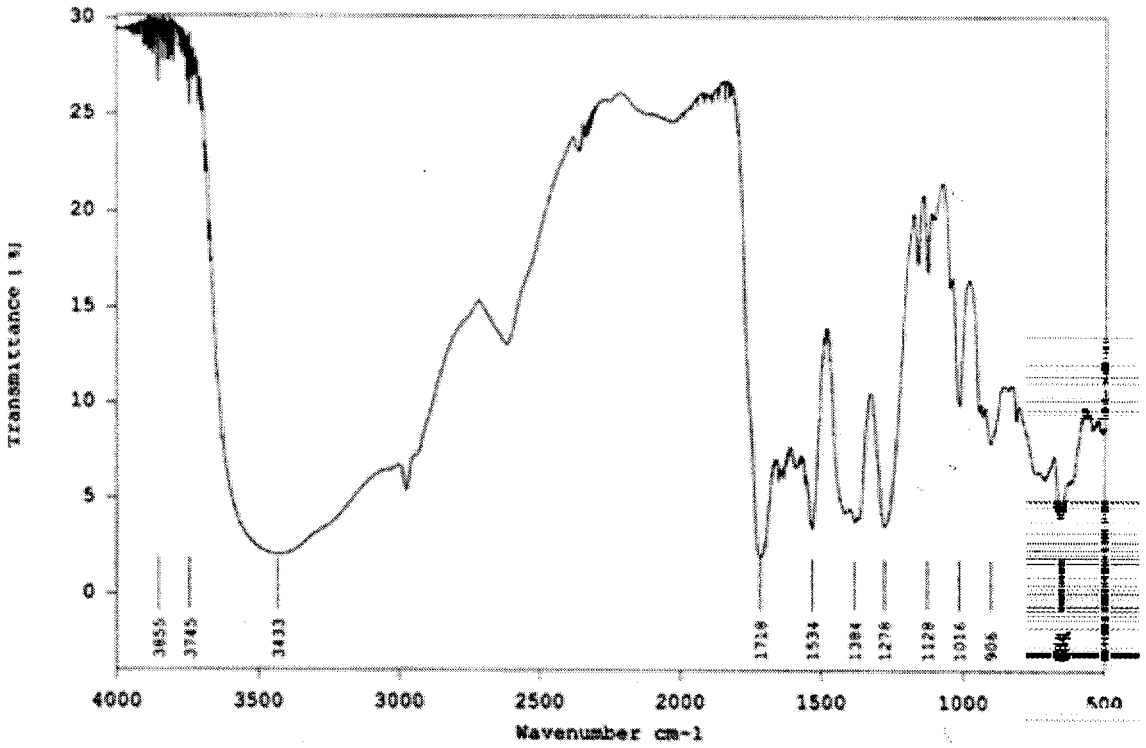

Figure 2-24 FTIR spectra of sol TiO_2-AcAc1

Besides AcAc, there are two other additives seen in sols that failed to yield nanorods, glacial acetic acid and diethanolamine (DEA). Both of these additives are known to form complexes with metal alkoxides, in which the added group is difficult to hydrolyze, therefore leading to slower condensation reactions[41,57]. This is likely the reason that the sol with DEA, as well as some of the sols with glacial acetic acid, was unsuccessful. Glacial acetic acid, however, does not always prevent nanorod formation, as seen in the TiO_2 and PZT sols. Its effect likely depends on the relative strength of the metal-acetate bond to hydrolysis, with some metals having relatively stronger bonding, and thus decreased condensation rates and lower probability of nanorod formation. Although there is, at present, no direct proof of this, it could likely be illustrated through partial charge calculations, along with FTIR experiments, as discussed above.

2.4.5.6 Sol concentration effects

The sol concentration can also play an important part in the growth of nanorods. If the concentration is low, the electrophoretic deposition process could severely deplete the concentration of nanoparticles in the sol during growth, and in some instances, the concentration could be so low that full-length nanorods could not be synthesized. Additionally, lower concentrations can increase the necessary deposition time. Although the concentration may not directly affect the individual particle velocity, the deposition rate (in particles deposited/unit area/unit time) is proportional to the particle velocity times the volume concentration of particles. Thus, there would be a direct link between concentration and growth rate.

Additionally, if the sol is diluted with a solvent (or mixture of solvents) which differs from the original sol composition, the particle mobility may change. This could be caused by changes in the solvent viscosity and or dielectric constant. For example, dilution with water would likely increase the dielectric constant significantly, leading to a possibly larger mobility.

Preparation of sols with a controlled concentration without modifying the chemistry of the sol nanoparticles can be a difficult task. For example, in the TiO_2 additional acetic acid may alter the number of functional groups attached to the sol clusters. If the acid is added prior to hydrolysis, stable sol formation is often not possible, due to reactions between the acid and titanium alkoxide. Without hydrolysis, mixtures with a $AcOH/Ti(OPr^i)_4$ ratio (R) greater than 1 are found to yield precipitates of $TiO(OAc)_2$, with a speed that increases with increasing R[59]. In the standard TiO_2 sol used here, $R \approx 10$ and the sol is hydrolyzed before precipitation can occur. However, when sols were attempted with an $R > 25$, precipitation was instantaneous upon alkoxide addition, and a very large excess of water was needed to dissolve the precipitate and form a clear sol, in agreement with published reports[59].

When dilution was attempted with one of the products of the sol formation (isopropanol), the sols destabilized. This may have been due to water, generated in-situ through esterification reactions between the acid and the alcohol[58]. Alternatively, it may have stemmed from changes in the electrostatic stabilization, through changes in ion

concentration, pH, and/or dielectric constant. Dilution of the sol by additional water may further hydrolysis. While acetic acid groups typically difficult to hydrolyze[59], changes in the hydrolysis ratio may affect their removal somewhat. For these reasons, stable sols were diluted with acetic acid after hydrolysis, and immediately used to synthesize nanorods. No precipitate or clouding of the sol was observed upon dilution, or after the growth period.

Figure 2-25 shows an SEM micrograph of TiO_2 nanorods grown in a 200 nm template at 1.67 V/cm from a dilute sol (0.17 M vs. 0.85 M for the standard sol). There does not appear to be any significant difference between these rods and ones grown from the standard sol under similar conditions. The morphology of this sample is similar to what is observed in other cases, and the average diameter is in the same range as for the concentrated sol. Accurate determination of the length of the nanorods from such SEM images is difficult, owing to uncertainties in the angles and initial template thickness. However, these rods do not appear to be significantly shorter than those from the more concentrated sol are.

2.4.6 Current measurements

Figure 2-26 is a sample of the recorded current as a function of growth time for TiO_2 nanorods grown in a 100 nm template, with 5 V applied potential, and a spacing of

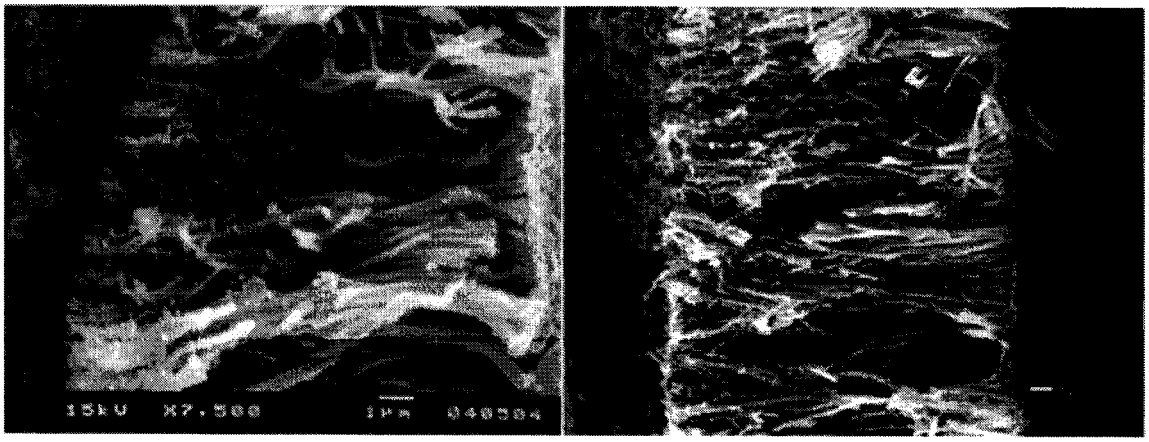

Figure 2-25 TiO_2 nanorods grown in 200 nm PC templates at 1.67 V/cm from 0.17 M (left) and 0.85 M (right) sols.

3 cm between the electrodes. From this data, one can see that the current rises quickly in the beginning of growth, and follows with a gradual increase after ~1500 seconds. It is postulated that the initial sharp current rise corresponds to the filling of the template pores from the bottom through the template. As the template pores are being filled with TiO_2 nanoparticles or clusters, the distance that charged species, either ions or TiO_2 nanoclusters, must move through the small template pores decreases. This results in a drop in total resistance, increasing the current. Another possible mechanism leading to an increase in current is the formation of a conductive path through the deposited TiO_2. Anatase is a wide band-gap semiconductor, and thus may conduct some of the current. It is possible that the resistivity of the deposited anatase is less than that of the anatase clusters moving in the sol, raising the current as the nanorods grow. After the pores are completely filled, the current rise with time is more gradual. This corresponds to the formation of a film of TiO_2 on top of the template.

Other current measurement have been made (Figure 2-27), showing the effect of changing the pore size, sol concentration, and applied field. It was found that the overall current increases with increasing applied field, and that time to reach a plateau in the current decreases (Figure 2-27B). Similarly, decreasing sol concentration decreased the current, and slightly increased the time until the current plateau (Figure 2-27A). Lastly, the effect of pore size was more difficult to explain. As expected, the total current decreases as the pore size decreases from 100 nm to 50 nm to 10 nm. For the 200 nm pores, the current is smaller than that for 100 nm pores, and lies about midway between that of 50 nm and 10 nm pores (Figure 2-27C). One partial explanation for this may have to do with the pore densities of the various templates. The rated pore densities are $6x10^8$ pores/cm^2 for all templates except the 200 nm, which have $4.5x10^8$ pores/cm^2. This would lower the expected current, but not enough to account for the measured value. Based on these values for the templates, the following relative currents are calculated. For 50 nm templates, the current should be 0.25 times that of the 100 nm templates. For 10 nm templates, the current should be 0.01 times that of the 100 nm templates. For 200 nm templates, the current should be 3 times that of the 100 nm templates. It is not know what caused this drastically reduced current value.

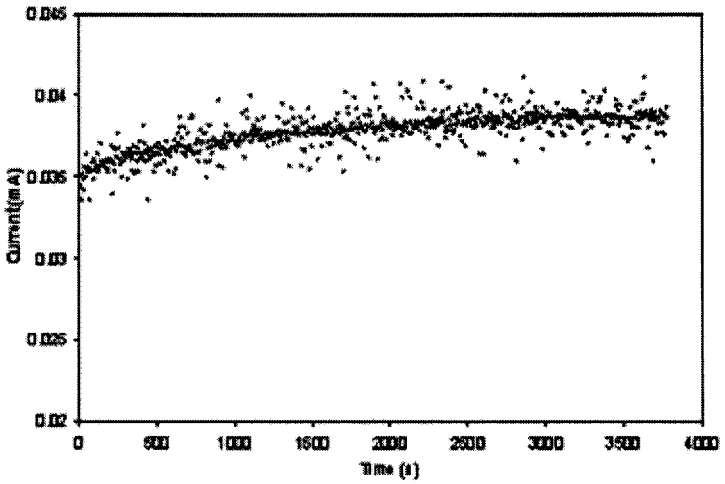

Figure 2-26 The recorded current as a function of time for TiO_2 nanorods grown in a 100 nm template at ~ 1.67 V/cm applied field.

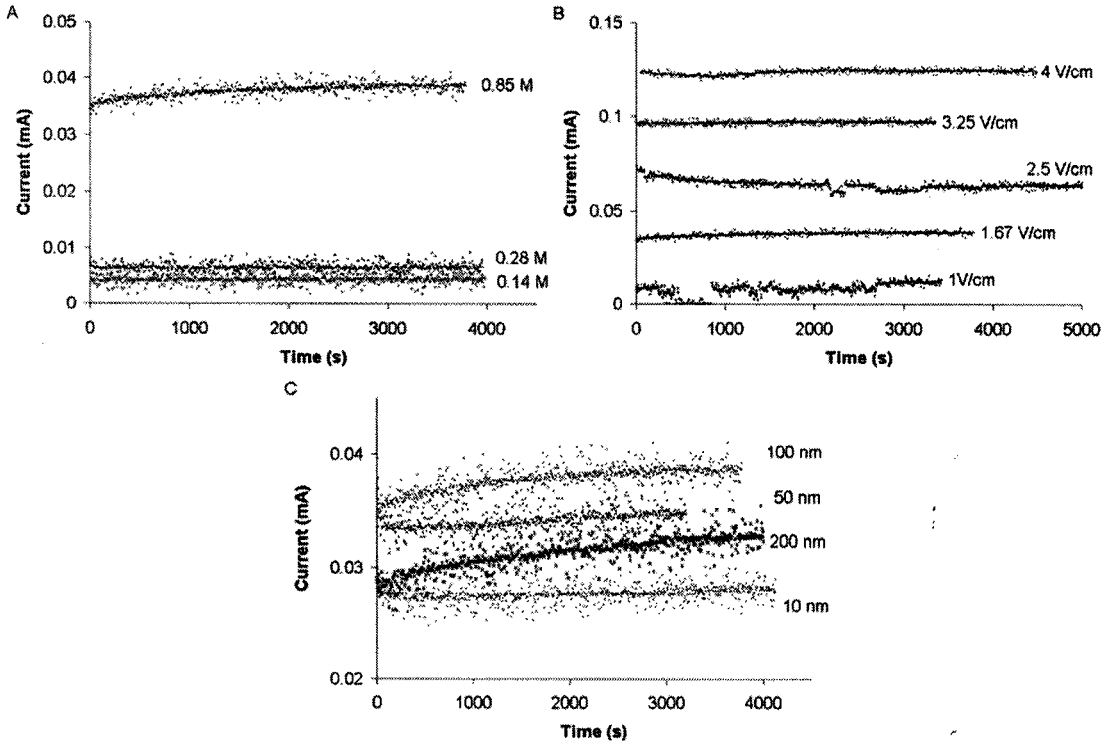

Figure 2-27 Recorded currents during nanorod growth for A) various sol concentration in 100 nm templates at 1.67 V/cm; B) various fields for standard concentration in 100 nm templates; and C) various templates at standard concentration of electric field.

2.4.6.1 Current model (1)

Since measurable current flows during the electrophoretic deposition, it was of interest to see if a model of the current vs. time could yield any information about the growth process. The current was calculated using a method similar to that used by Vandeperre and van der Biest[60], where the current path was broken into three sections, as shown in Figure 2-28a. In each section, the resistance of the circuit is considered to consist of two parallel components. In section 1, they are counter-ions diffusing through the pores of TiO_2 deposit and conduction of TiO_2 deposit. In sections 2 and 3, they are TiO_2 nanoparticles and counter-ions diffusing in the sol. Figure 2-28b shows the equivalent circuit used to calculate the current. The resistances are:

$$R_{1,sol} = \frac{\rho_{sol} d_1}{A_p N_p}$$ **Equation 2-7**

$$R_{1,p} = \frac{\rho_{TiO2} d_1}{A_p N_p}$$ **Equation 2-8**

$$R_{2,sol} = \frac{\rho_{sol} (s - d_1)}{A_p N_p}$$ **Equation 2-9**

$$R_{2,p} = \frac{d - d_1}{A_p N_p \mu Qc}$$ **Equation 2-10**

$$R_{3,sol} = \frac{\rho_{sol} (d - s)}{A_c}$$ **Equation 2-11**

$$R_{3,p} = \frac{d - d_1}{A_c \mu Qc}$$ **Equation 2-12**

where s is the thickness of the template, d_l is the thickness of the deposit, d is the distance between electrodes, A_p is the cross-sectional area per template pore, N_p is the total number of pores and A_c is the cross-sectional area of the growth cell. In the resistances, ρ_{sol} is the ionic resistivity of the sol, ρ_{TiO2} is the resistivity of the TiO_2 deposit, μ is the mobility of the TiO_2 nanoparticles, Q is the effective charge per unit mass of the TiO_2 nanoparticles and c is the concentration of the sol. Because of the small volume of TiO_2 depleted from the sol (approximately ~ 1%) by nanorod growth, the concentration of the sol is assumed to remain constant. In this circuit, the resistances due to the electrodes and the interface reactions are neglected, as they are likely to be constant with time.

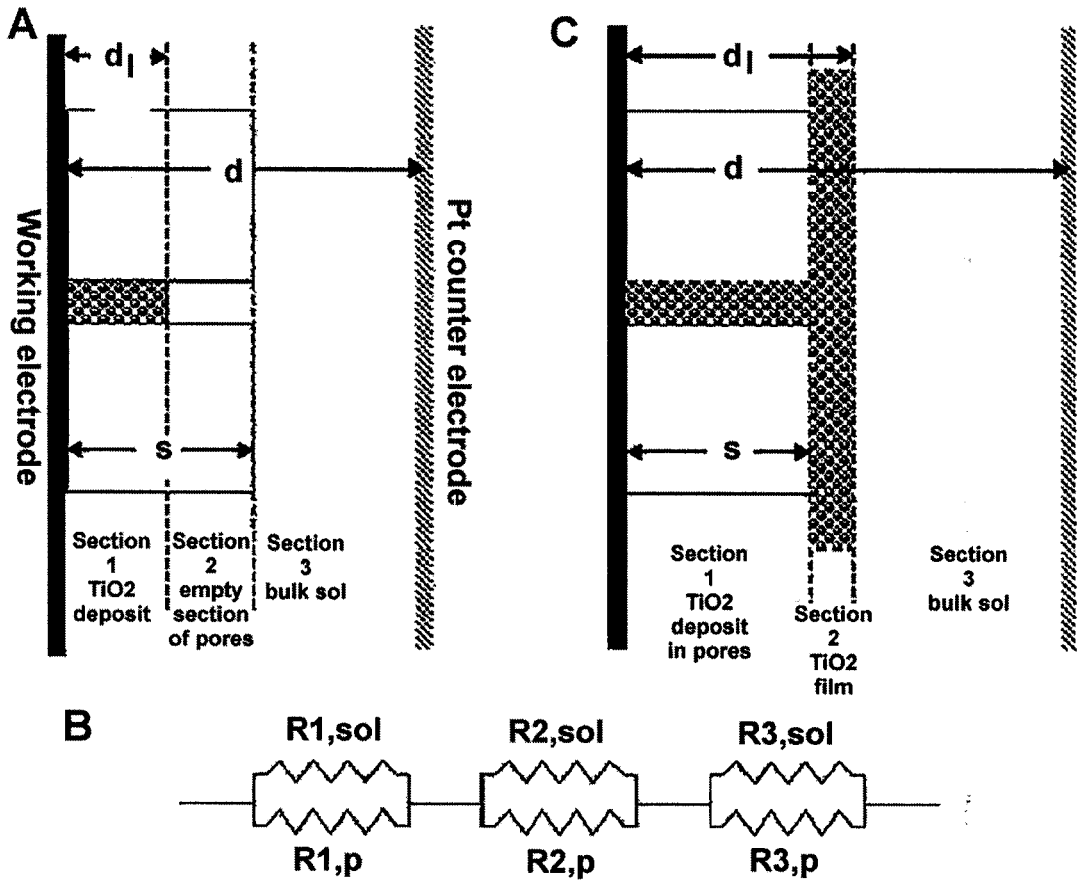

Figure 2-28 The models used in the current calculations: A) the three sections of the growth process, for $d_l < s$; B) the equivalent circuit for part A); and C) the three sections of the growth process for $d_l > s$.

This circuit only applies for times up to the moment when the template pores are completely filled; after that, the system consists of three different sections as shown in Figure 2-28c. For this circuit, the resistances in sections 1 and 3 are similar to those above, modified for $d_l > s$. In section 2, however, the resistances are similar to those in section 1, with A_pN_p replaced by A_c. Equations 2.7-2.12 give the current as a function of the grown thickness, d_l, through Ohm's law. In order to compare the calculated currents to the observed values, it is necessary to have the current as a function of time. If the concentration is constant with time, the rate of mass deposition due to electrophoresis is[61]:

$$\frac{dM_{deposit}}{dt} = \rho_{deposit}\frac{dV_{deposit}}{dt} = \mu E A_{deposit} c \qquad \textbf{Equation 2-13}$$

where $M_{deposit}$ is the total mass deposited, $\rho_{deposit}$ is the density of the deposit, $V_{deposit}$ is the total deposited volume, $V_{deposit}$ is the area for deposition (A_pN_p or A_c, depending on deposit thickness) and E is a function of time. For all times where $d_l < s$, the volume of the deposit is can be calculated from the area of the template pores and the thickness of the deposit. An approximate solution of this equation gives:

$$t = \frac{\rho_{deposit}\left[d^2 - (d - d_l)^2\right]}{2\mu Vc} \qquad \textbf{Equation 2-14}$$

where V is the voltage drop across sections 1 and 2, and can be calculated from the applied voltage (V_a) and current as:

$$V = V_a - I\left(\frac{1}{R_{1,sol}} - \frac{1}{R_{1,p}}\right)^{-1} \qquad \textbf{Equation 2-15}$$

A similar expression can be derived for $d_l > s$. Using these equations, one can calculate I and t as functions of d_l, and combine these to plot I as a function of t. A sample of such a calculation is shown in Figure 2-29, for TiO_2 grown in 100 nm templates at 5 V and 3 cm separating the electrodes. Although the currents calculated by this method are much larger than those measured are, they show the identical

qualitative trend. That is, the current increases sharply up to the time when the template pores are completely filled, and then increases more gradually as a film of TiO_2 forms over the entire template. The calculated currents also show a qualitative agreement with measured values under different experimental conditions, such as changes in sol concentration or applied voltage.

It was observed experimentally that samples grown for longer times have a thick film attached to the nanorods, where those grown for shorter times have little or no film. Both experimental results and calculation strongly supports the proposed model, for the growth of non-conductive oxide nanorods by electrophoresis that nanorod growth proceeds via motion of the nanoparticles to the bottom of the template pores, filling them up as time proceeds. Similar calculations have been performed for the various sol concentrations, applied fields and template sizes, showing the same type of agreement in all cases, except that (as mentioned above), the relative value of the current in 200 nm templates is calculated much higher than the measured value (See Figure B-3, Appendix B).

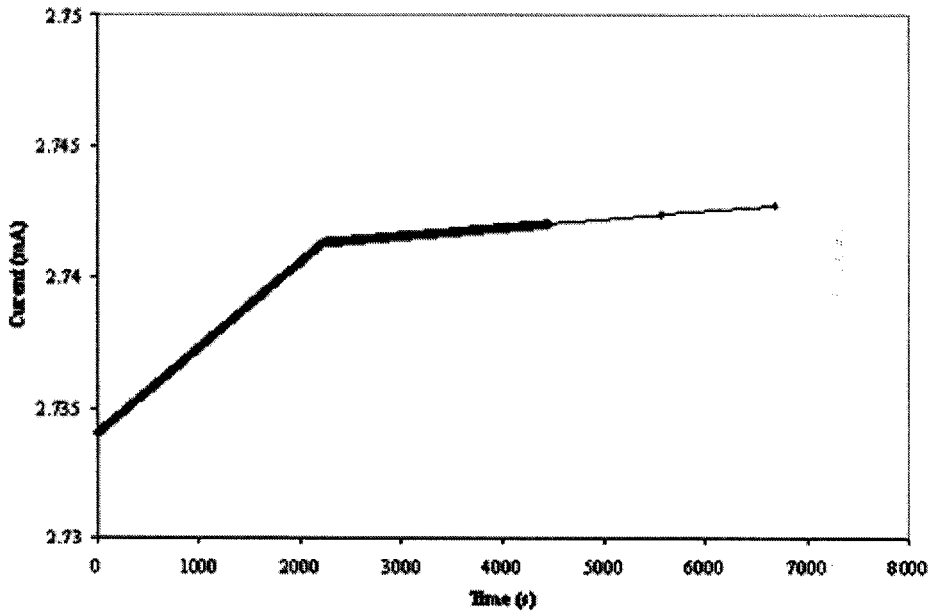

Figure 2-29 Calculated currents for growth of TiO_2 nanorods grown in a 100 nm template at ~ 1.67 V/cm applied field.

2.4.6.2 Current/growth model (2)

While the previous model shows a general qualitative agreement with measured results, the overall magnitude of the calculated current was off by almost two orders of magnitude. Since the first model is clearly inadequate, a second model was developed. For this model, the conductance of the sol was assumed due solely to the ionic species present. To test this approximation, a solution was made which approximates the liquid phase of the TiO_2 sol, without the sol nanoparticles, by mixing 2 parts glacial acetic acid, 1 part water, and 1 part isopropanol (which would be produced by the hydrolysis os the $Ti(OPr^i)_4$ in the sol). When the current was recorded for this solution in a 100 nm PC template, the magnitude of the current was almost identical to that of the sol (see Figure B-4, Appendix B).

First, the conductivity of the sol was directly measured rather than calculated from the molar conductivities of the species, as in the previous method. To do this, the cell constant for the growth cell was determined by measuring its resistance when filled with 0.1 M KCl. Since the molar conductivity of aqueous KCl is well known (129 S cm^2 mol^{-1})[62], one can use the measured resistance (63 kΩ) to calculate a cell constant of 812.7. This constant, divided by the measured sol resistance (1.1 MΩ) yields the sol resistivity value of 7.39×10^{-4} S cm^{-1}.

The deposition model used was derived from that in Reference 63, however similar results were obtained from the method outlined in Reference 28. In both cases, the simplifying assumption of no depletion of nanoparticles was made, as discussed above. The deposition with time is described through the following equation:

$$\delta = \frac{2\varepsilon_L \zeta \varphi_s V_a t}{3\eta\varphi_c d} \qquad \textbf{Equation 2-16}$$

where δ is the deposit thickness at time t, ε_L is the dielectric constant of the liquid, ζ is the zeta potential of the particles in the sol, V_a is the applied voltage, φ_s is the volume concentration of particles in the suspension, φ_c is the cast packing factor (one minus porosity), η is the sol viscosity and d is distance between the electrodes.

The particles in the sol experience a field that changes with time as the deposit grows according to:

$$E_S = \frac{V_a}{\left(\frac{\varepsilon_L}{\varepsilon_c} - 1\right)\delta + d} \qquad \textbf{Equation 2-17}$$

where ε_c is the effective permittivity of the deposited material. Combining this electric field with the measured conductivity of the sol and the known cross-sectional area of the nanopore array, one can calculate the current vs. time flowing in the growth cell. This is accomplished by applying Ohm's law with the field E_s, the sol conductivity, and the conductivity of the deposit. Figure 2-30 shows the calculated current vs. time for some of the experimental parameters used. These currents are fairly close to the overall trend of the measured currents, although they do not quite capture some of the fluctuations at short times. While the values appear to be constant in this figure, they actually show a

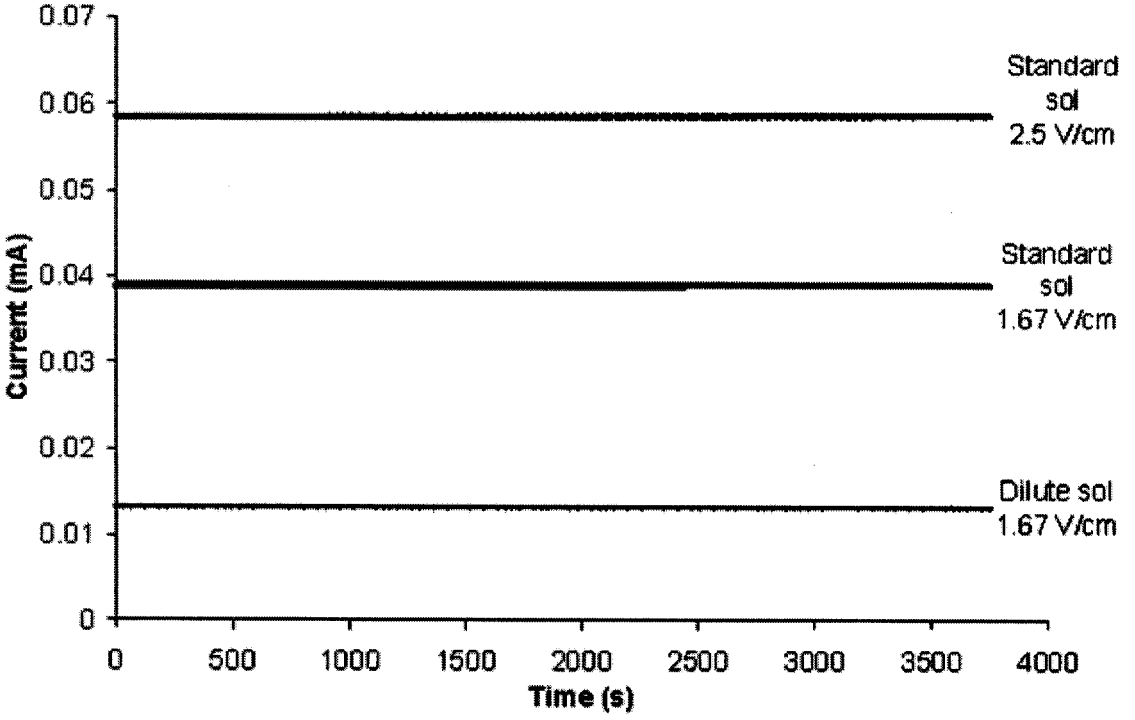

Figure 2-30 Calculated currents for the growth of TiO_2 nanorods in 100 nm templates.

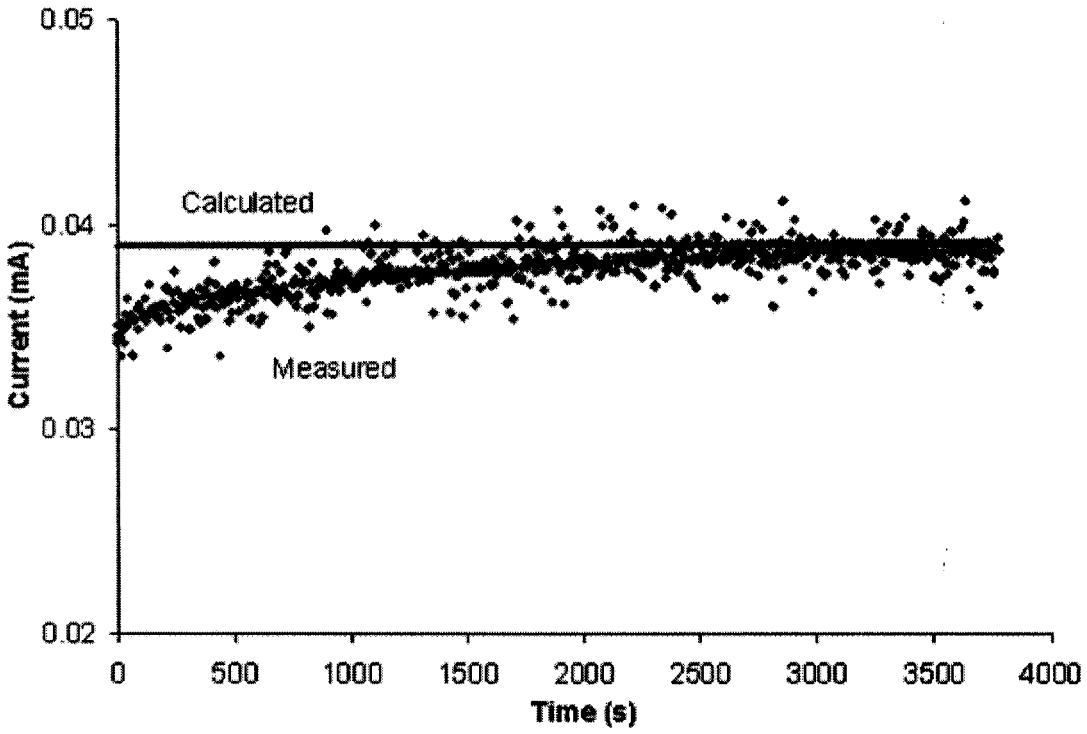

Figure 2-31 Calculated and measured currents for TiO_2 growth in 100 nm templates at 1.67 V/cm.

slight increase with time, as the distance to the growth surface decreases. For example, Figure 2-31 shows a comparison of the measured and calculated values for growth of TiO_2 nanorods in 100 nm templates at 1.67 V/cm. While the initial behavior differs, the general agreement between the two is quite good. Similar behavior is seen when comparing TiO_2 nanorods grown in 100 nm templates at 2.5 V/cm, and at 1.67 V/cm from a dilute sol.

Overall, this model captures the magnitude of the current during nanorod growth far better than the original model. However, the initial transients in the current are unexplained in this version. It is likely that neither model completely captures the behavior of this system. Other potentially important effects may influence the evolution of current during EPD. For example, there may be effects due to electroosmosis. In this effect, the surface charge on the pore walls causes liquid to flow through the pores under an applied field. This would alter the velocity of the ions and nanoparticles, changing

the current. Additionally, as deposition proceeds, the pores become blocked, which would further complicate the fluid flow.

2.4.6.3 Other conclusions from the current measurements

To better understand the current distributions in the growth cell, a cyclic voltammogram was recorded in the TiO_2 sol, using the actual growth electrode as the working electrode, with a Pt mesh counter electrode and saturated calomel (SCE) reference electrode. The overpotential (total potential minus equilibrium potential) was scanned in a narrow range around equilibrium, so that the cure was in the linear regime. From this data, one can determine the Wagner number (W_a) [64]:

$$W_a = \frac{\kappa}{l}\left(\frac{d\eta}{dj}\right) \qquad \textbf{Equation 2-18}$$

where κ is the sol conductivity, ($d\eta/dj$) is the slope of the current density-overpotential curve in the linear region, and l is a characteristic length (namely, the radius of the working electrode). The Wager number is a dimensionless quantity that characterizes the current distribution around an electrode. Small values represent very fast reaction kinetics, while larger values occur for more sluggish reactions. Small values also correspond to a more non-uniform current distribution around the working electrode. That is, more current flows at the edges of the electrode than in the middle. The data for this system yields a value for $W_a \approx 1$, showing that the reaction kinetics are not too slow. This also shows that the deposit is likely to be fairly uniform over the surface of the working electrode. That is, the template will be more evenly filled, rather than having a large preferential growth at the edges.

2.5 Conclusions

The applicability of sol-gel electrophoresis to the creation of various simple and complex oxide nanorods has been demonstrated. Oxide nanorods with a diameter ~125-

200 nm and a length of about 10 μm were grown in polycarbonate membranes using sol-gel electrophoresis. This technique offers several advantages, including the ability to growing large areas of uniformly sized and nearly unidirectional aligned nanorods of various oxides. It is also believed to yield a more dense oxide nanorod prior to sintering than sol-gel without electrophoresis. Appropriate sol preparation can easily lead to formation of the desired stoichiometric chemical composition, which would be preserved during the electrophoretic growth of nanorods. Dense single-phase crystalline oxide nanorods can be readily achieved by firing at elevated temperatures.

Not every oxide system attempted has been successful. For instance, numerous sol preparation techniques for $BaTiO_3$ were attempted before finding one that was successful. Similarly, to date nanorods ZnO have not been successfully synthesized. There are a few possible reasons for the inability to synthesize certain materials.

First, the sols particle generated in a given recipe may have insufficient mobility to fill the templates in a reasonable time. This may explain the results from one of the ZnO sols used, which had a pH close to the isoelectric point of ZnO, and thus a small zeta potential and mobility. This could be overcome by selecting a different sol that has a higher mobility (for example, one that is stable at a pH far removed from the IEP).

A second possibility is that electrostatic attraction between the charged particles and (oppositely) charged template walls leads to blockage of the template pore opening, preventing the growth of nanorods. This could possibly be over come by using a higher applied electric field, so that the attraction to the working electrode is significantly higher than the attraction to the pore walls. Alternatively, one could change the template used or the sol conditions so that the particles are not strongly attracted to the pore walls.

A third possibility is that the applied field, sol concentration, or some other parameter of the growth has simply not been optimized. By attempting variation of the relevant parameters, it should be possible to find the proper set of growth conditions for the synthesis of the desired oxide nanorod.

Notes to Chapter 2

[1] Del Monte, F.; Larsen, W.; Mackenzie, J.D. *J. Am. Ceram. Soc.* **2000**, *83*, 1506.

[2] Zhao, G.; Han, G.; Takahashi, M.;Yoko, T. *Thin Solid Films* **2002**, *410*, 14.

[3] Villegas, M.A.; Pascual, L. *Thin Solid Films* **1999**, *351*, 103.

[4] Bhatia, R.B.; Brinker, C.J.; Gupta, A.K.; Singh, A.K. *Chem. Mater.* **2000**, *12*, 2434.

[5] Brinker, C.J.; Scherer, G.W. *Sol-gel science : the physics and chemistry of sol-gel processing*, Academic Press, Boston, 1990.

[6] Seraji, S.; Wu, Y.; Jewell-Larson, N.E.; Forbess, M.J.; Limmer, S.J.; Chou, T.P.; Cao, G.Z. *Adv. Mater.* **2000**, *12*, 1421.

[7] Lefevre, M.J.; Speck, J.S.; Schwartz, R.W.; Dimos, D.; Lockwood, S.J. *J. Mater. Res.* **1996**, *11*, 2076.

[8] Ting, C.-C.; Chen, S.-Y.; Liu, D.-M. *J. Appl. Phys.* **2000**, *88*, 4628.

[9] Forouhi, A.R.; Bloomer, I. *Phys. Rev. B* **1986**, *34*, 7018.

[10] Zhang, Q.; Gao, L.; Guo, J. *J. Eur. Ceram. Soc.* **2000**, *20*, 2153.

[11] Alam, M.J.; Cameron, D.C. *Thin Solid Films* **2000**, *377-378*, 455.

[12] Yamamoto, O.; Sasamoto, T. *J. Mater. Res.* **1992**, *7*, 2488.

[13] Stoica, T.F.; Stoica, T.A.; Vanca, V.; Lakatos, E.; Zaharescu, M. *Thin Solid Films* **1999**, *348*, 273.

[14] Tahan, D.M.; Safari, A.; Klein, L.C. *J. Am. Ceram. Soc.* **1996**, *79*, 1593.

[15] Sarmini, K.; Kenndler, E. *J. Biochem. Biophys. Methods* **1999**, *38*, 123.

[16] Kumar, S.R.; Suresh, C.; Vasudevan, A.K.; Perumal, P.; Warrier, K.G.K. *Trans. Indian Ceram. Soc.* **1999**, *58*, 118.

[17] Limmer, S.J.; Cao, G.Z. *Adv. Mater.* **2003**, *15*, 427.

[18] Kamei, M.; Shigesato, Y.; Takaki, S. *Thin Solid Films* **1995**, *259*, 38.

[19] Cullity, B.D. *Elements of X-Ray Diffraction*, 2nd edition, Addison-Wesley, Reading, MA, 1978.

[20] Feldman, L.C.; Mayer, J.W. *Fundamentals of Surface and Thin Film Analysis, Elsevier Science Publishing Co., Inc.*, New York, NY, 1986.

[21] Chan, C.M.; Cao, G.Z.; Fong, H.; Sarikaya, M.; Robinson, T.; Nelson, L. *J. Mater. Res.* **2000**, *15*, 148.

[22] Orel, B.; Maček, M.; Grdadolnik, J.; Meden, A. *J. Solid State Electr.* **1998**, *2*, 221.

[23] Aegerter, M.A. *Sol. Energ. Mat. Sol. C.* **2001**, *68*, 401.

[24] Navarro, A.; Alcock, J.R.;. Whatmore, R.W. *J. Eur. Ceram. Soc.* **2004**, *24*, 1073.

[25] Ma, J.; Zhang, R.; Liang,, C.H.; Weng, L. *Mater. Lett.* **2003**, *57*, 4648.

[26] Kosmulski, M.; Matijević, E. *Colloid. Surface.* **1992**, *64*, 57.

[27] Shaw, D.J. *Introduction to Colloid and Surface Chemistry,* 4th edition, Butterworth-Heinemann Ltd., Oxford, 1992.

[28] Sarkar, P.; Nicholson, P.S., *J. Am. Ceram. Soc.* **1996**, *79*, 1987.

[29] Gu, Y. *J. Colloid Interf. Sci* **2000**, *231*, 199.

[30] Hunter, R.J. *Zeta Potential in Colloid Science*, Academic Press, London, 1981.

[31] Gu, Y.; Li, D. *J. Colloid Interf. Sci.* **1999**, *217*, 60.

[32] Bergström, L. *Advan. Colloid Interface Sci.* **1997**, *70*, 125.

[33] Visser, J. *Advan. Colloid Interface Sci.* **1972**, *3*, 331.

[34] Parks, G.A. *Chem. Rev.* **1965**, *65*, 177.

[35] Kosmulski, M. *Langmuir* **1997**, *13*, 6315.

[36] Bruyère, V.I.E.; Morando, P.J.; Blesa, M.A. *J. Colloid Interf. Sci.* **1999**, *209*, 207.

[37] Wang, Y.C.; Leu, I.C.; Hon, M.H. *J. Mater. Chem.* **2002**, *12*, 2439.

[38] Kim, K.J.; Fane, A.G.; Nyström, M.; Pihlajamaki, A. *J. Membrane Sci.* **1997**, *134*, 199.

[39] Lettmann, C.; Möckel, D.; Staude, E. *J. Membrane Sci.* **1999**, *159*, 243.

[40] Seshadri, K.S.; Kesavamoorthy, R.; Srinivasan, M.P.; Varatharajan, K.; Ahmed, J.; Krishnasamy, V. *B. Electrochem.* **1998**, *14*, 16.

[41] Sanchez, C.; Livage, J.; Henry, M.; Babonneau, F. *J. Non-Cryst. Solids* **1988**, *100*, 65.

[42] Barboux-Doeuff, S.; Sanchez, C. *Mat. Res. Bull.* **1994**, *29*, 1.

[43] Nass, R.; Schmidt, H. *J. Non-Cryst. Solids* **1990**, *121*, 329.

[44] Nishide, T.; Mizukami, F. *Thin Solid Films* **1995**, *259*, 212.

[45] Tohge, N.; Fujii, E.; Minami, T. *J. Mater. Sci.-Mater. El.* **1994**, *5*, 356.

[46] Leaustic, A.; Babonneau, F.; Livage, J. *Chem. Mater.* **1989**, *1*, 248.

[47] Papet, P.; Le Bars, N.; Baumard, J.F.; Lecomte, A.; Dauger, A. *J. Mater. Sci.* **1989**, **24**, 3850.

[48] Sedlar, M.; Sayer, M. *J. Sol-Gel Sci. Techn.* **1995**, *5*, 27.

[49] Livage, J.; Henry, M. In *Ultrastructure Processing of Advanced Ceramics*, John Wiley & Sons, New York, NY,1988.

[50] Doeuff, S.; Henry, M.; Livage, J. *Mat. Res. Bull.* **1990**, *25*, 1519.

[51] Basu, S.; Chatterji, K.K. *Z. Phys. Chem. (Leipzig)* **1958**, *209*, 360.

[52] Yamasaki, K.; Sone, K. *Nature* **1950**, *166*, 998.

[53] Selbin, J. *Chem. Rev.* **1965**, *65*, 153.

[54] Basu, G.; Yeranos, W.; Belford, R.L. *Inorg. Chem.* **1964**, *3*, 929.

[55] Bernal, I.; Rieger, P.H. *Inorg. Chem.* **1963**, *2*, 256.

[56] Nakamoto, K. *Infrared and Raman Spectra of Inorganic and Coordination Compounds*, 3rd ed., John Wiley & Sons, New York, 1978

[57] Yoda, S.; Ohshima, S.; Kamiya, K.; Kawai, A.; Uchida, K.; Gotoh, A.; Ikazaki, F. *J. Non-cryst solids* **1996**, *208*, 191.

[58] Ivanda, M.; Musić, S.; Popović, S.; Gotić, M., *J. Mol. Struct.* **1999**, *480-481*, 645.

[59] Doeuff, S.; Henry, M.; Sanchez, C.; Livage, J., *J. Non-Cryst. Solids* **1987**, *89*, 206.

[60] Vandeperre, L.J.; van der Biest, O.O. In *Innovative Processing and Synthesis of Ceramics, Glasses, and Composites 1997*, American Ceramic Society, Westerville, Ohio, 1997.

[61] Simone, A.; Spinelli, P. *Mater. Eng.* **2002**, *13*, 33.

[62] Atkins, P., *Physical Chemistry*, 5th Ed., Oxford University Press, Oxford, 1994.

[63] González-Cuenca, M.; Biesheuvel, P.M.; Verweij, H., *AIChE J.* **2000**, *46*, 626.

[64] McNaught, A.D.; Wilkinson, A., Eds, *Compendium of chemical terminology: IUPAC recommendations*, Blackwell Science, Oxford, 1997

3 Properties of oxide nanorods

3.1 Introduction

Many materials show interesting changes in properties as their size diminishes[1], and this fact is one of the driving forces for the interest in nanotechnology research. There are wide varieties of causes for this size dependence, from quantum confinement effects to surface energy considerations. For the types of oxide materials synthesized in this research, there are a few important considerations about size and properties.

The relation between size and electrical properties is complex, since there are numerous mechanisms that may be important. These mechanisms can be grouped into four categories: surface scattering[2] (including grain boundary scattering), quantized conduction[3], band gap widening[4] and changes in microstructure[1]. For the conductive nanorods here, the size is far too large for quantized conduction or band gap effects to be important, and the morphology of these polycrystalline nanorods is likely of little importance. This leaves scattering effects as a potentially important consideration.

In nanowires and thin films, the electron scattering at surfaces reduces the electronic conductivity. When the critical dimension of thin films and nanowires is smaller than the electron mean-free path, the motion of electrons will be altered by collisions with the surface. The electrons undergo either elastic or inelastic scattering. In elastic scattering, the electron does not lose energy, and its momentum along the direction parallel to the surface is conserved. Thus, elastic scattering has no size-dependant effect on the electrical conductivity. If, however, the scattering is inelastic, the scattered electron loses its velocity along the direction parallel to the surface or the conduction direction, and the electrical conductivity decreases. The smaller the characteristic dimension in relation to the electron mean free path, the more often these inelastic scattering events will occur, and the smaller the conductivity will be.

The effect of size on the properties of ferroelectric materials is complex, with different effects being observed in different systems. In some systems, the effects are tied to the chemistry of that particular system. In others, the effects include grain boundaries, defects and stress.

Many ferroelectrics show a first an increase, and then a decrease in dielectric constant with decreasing grain size. Size effects on ferroelectric and dielectric properties of bulk and thin film ferroelectrics have been summarized in several review articles[5,6]. In some classes of ferroelectric, it has been suggested that these materials contain a small layer of a low k substance at the grain boundaries[7,8]. The thickness of this boundary layer has been observed to increase with decreasing grain size. This gives a decreasing value of the dielectric constant as the grains decrease in size. Another explanation for this behavior is related to the observation that phase transition temperatures reduce with the particle size. In the case of ferroelectric materials, this could lead to a reduction of the Curie temperature (ferroelectric-paraelectric phase transition temperature) to below room temperature for small enough particles of some ferroelectrics. This would lead to a loss of observable ferroelectric behavior for small enough particles.

Lattice defects affect the dielectric constant through the suppression of domain formation. Thus, the dielectric constant decreases as the number of defects increases (smaller grains). Stress effects have also been long proposed to account for the variation of dielectric properties with grain size in materials such as $Pb_{0.9}La_{0.1}TiO_3$ (PLT)[9] and $BaTiO_3$ [9]. It is suggested that increased internal stress leads to an increased dielectric constant, perhaps by stabilizing the ferroelectric state at smaller sizes[10,11].

Electrochromism in transition metal oxides is seen upon the intercalation of ions such as Li^+. This intercalation behavior is key to the properties of electrochromic oxides, and is influenced by size in many cases. Decrease in particle size has been shown to lead to improved electrochromic properties (such as switching rate and contrast ratio). This effect has been attributed to effects from grain boundary phases[12,13], high surface areas enabling facile ion transport[13] and short diffusion lengths through nanostructures[14]. Improved ion intercalation/deintercalation kinetics[15] and electronic conduction[16] are also observed in nanostructured electrochromic oxides.

Although the focus of this research is primarily on the development of a novel method for the synthesis of oxide nanorods, it is of interest to observe the variations in physical properties that can occur as the dimensions of a material are reduced. More

specifically, we have conducted some preliminary studies on the electrical, dielectric and electrochromic properties of nanorod arrays synthesized via sol EPD.

3.2 Electrical and optical properties of ITO nanorods

First, it was necessary to determine if the new sol produces the desired ITO phase. Powder XRD, shown in Figure 2-12, demonstrates that the desired phase has already appeared after heating to 400 °C, with the crystallinity improving upon further heating up to 700 °C. Only peaks corresponding to the desired cubic In_2O_3 phase were observed in the powder.

To test the properties of the sol, thin films were prepared on glass slides by spin coating. First, a thin silica buffer layer was spun on using a polymeric silica sol[17], to minimize diffusion of Na from the glass into the film[18]. The final ITO film consists of five coats, with a two-step drying (110 and 300 °C) between coats. The films were then given a final firing at 400-700 °C for 1 hour in air.

All fired films are transparent, with a transmission greater than 80% between 450-750 nm, as seen in Figure 3-2. The decrease in transmission at higher firing temperatures may be due to increased grain growth. The films are all conductive, as well, with a resistivity dependent on the firing temperature, as seen in Figure 3-1. The samples fired at 700 °C have the best properties, with a resistivity of ~1.44×10^{-2} Ω-cm. This value falls roughly in the middle of the range reported in the literature (~1.5×10^{-3} Ω-cm[19] to ~ 2.0×10^{-2} Ω-cm[20]) for sol-gel ITO films fired in air.

To determine the approximate resistivity of the ITO nanorods, samples were grown in an AAM template for 6 hours, and then dried. Since a temperature of 700 °C was determined to give the best properties in films, the samples in AAMs were also fired at 700 °C for 1 hour. This yields a composite of ITO nanorods embedded in the AAM membrane. Electrodes were placed on each side of the composite membrane using silver paste, and wires were attached. The resistance of this setup was then measured, and found to be 2.61 Ω after subtracting the contribution from the wires and silver electrodes. This data was used to calculate an approximate resistivity for the

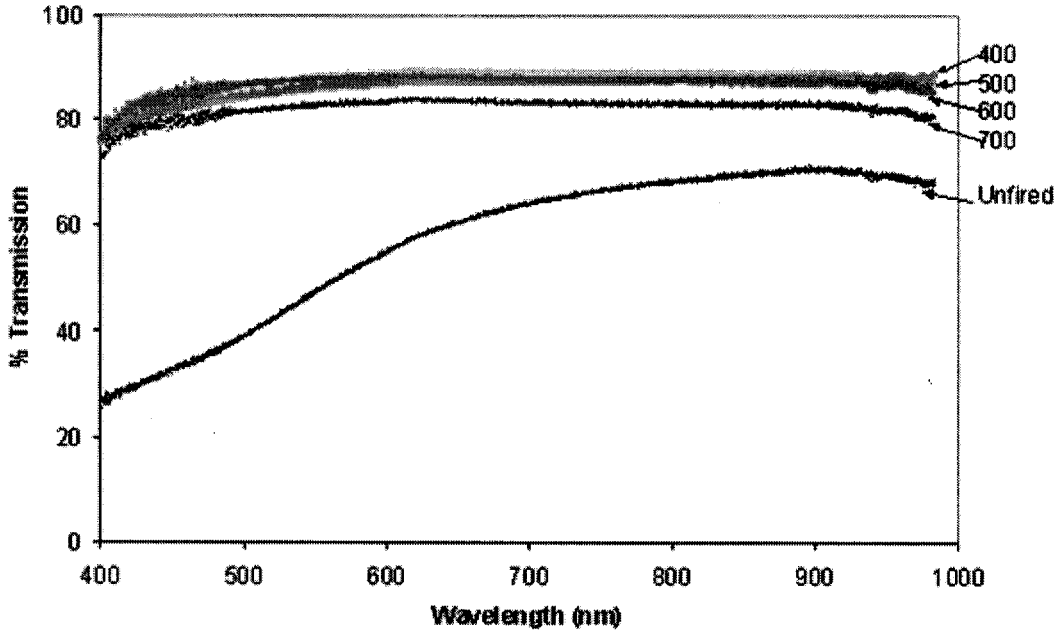

Figure 3-1 Resistvity of ITO films vs. firing temperature.

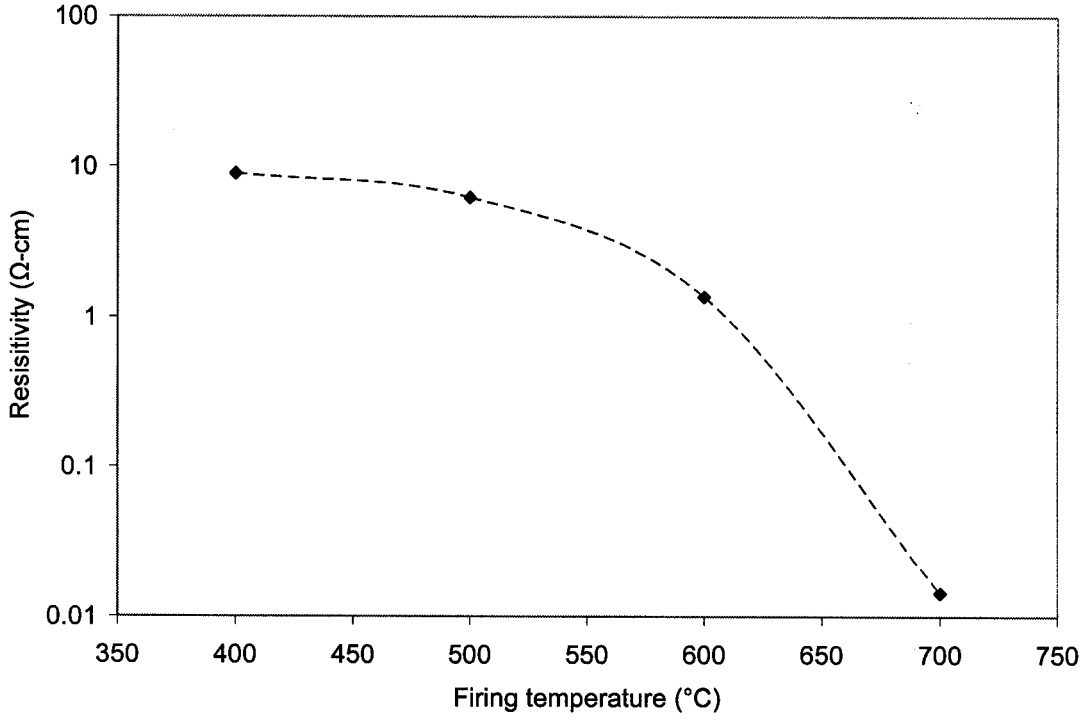

Figure 3-2 Transmission of ITO films fired at various temperatures.

nanorods, based on the electrode area (~ 0.08 cm^2), the number density of nanorods ($10^9/cm^2$), and the length and diameter of the nanorods (60 μm and ~140 nm, respectively). This gives a value of ~ 5 Ω-cm for the bulk resistivity of the nanorods. Obviously, this is a very crude method to determine the resistivity of the nanorods, which is, in part, why the value obtained is so much larger than those typically reported in the literature are.

One possible explanation for the large resistivity recorded would be scattering at the grain boundaries or nanorod walls. Using a typical value of carrier concentration ($n \approx 10^{20}/cm^2$)[21] and the resistivity measured from ITO films (of the same sol), one can calculate an electron mean free path of about 3 nm[21]. Thus, grain boundary scattering may have a detrimental effect on the nanorod resistivity. Additionally, very poor conductivity ($\rho \approx 800$ Ω-cm) has been found previously in mesoporous ITO[22]. The authors suggest that the low conductivity is due to residual organic components, grain-boundary effects in the powder and defects in the wall structure.

It is also possible that not all of the ITO nanorods embedded in the template contribute to the electrical conductivity. Figure 2-11a and Figure 2-11b suggest that a certain fraction of the ITO nanorods break during or after firing. The additional constraints imposed when sintering samples in the rigid AAM template may lead to an even greater number of broken ITO nanorods. Furthermore, it is possible that not all channels of the AAM are filled. Both of these effects would reduce the effective cross-sectional area, leading to a calculated resistivity higher than the actual value. Another possibility is that the nanorods are shorter than imagined, but still contact both electrodes. In this case, the reduced length would lead to a calculated resistivity lower than the actual value. Additionally, conductivity in In_2O_3 is very sensitive to local environment[23], so the behavior of ITO nanorods embedded in alumina may differ from films or freestanding nanorods. A final possibility is changes in the composition, due to inter-diffusion between the alumina membrane and the ITO during firing. This may have altered the conductivity of samples prepared in the AAM relative to films or those in the PC templates.

3.3 Dielectric properties of PZT nanorods

Experiments to determine the dielectric and ferroelelectric properties of PZT nanorods are currently underway. This section presents some of the preliminary results obtained so far. To determine the dielectric properties of PZT nanorods, samples were grown in an AAM for 4 hours at ~1.67 V/cm, then dried at ~110 °C. Dried samples were then fired at 700 °C for 1 hour. Electrodes were pained on both sides of the sample with silver paste, and Pt wires were attached to the electrodes. The dielectric constant vs. frequency was recorded at room temperature, followed by dielectric constant vs. temperature for three distinct frequencies (1, 10 and 100 kHz). The recorded dielectric constant is for the composite Al_2O_3/PZT, so the values are smaller than one would expect for PZT alone.

Figure 3-3A shows the measured dielectric constant vs. frequency at room temperature, while Figure 3-3B is the dielectric constant as a function of temperature for three different frequencies. From the capacitance vs. temperature data, one can see a peak at ~520 °C, which is significantly larger than the Curie temperature for PZT. Values for the transition temperature of PZT are typically intermediate between those for $PbTiO_3$ (~490 °C[24]) and $PbZrO_3$ (~230 °C[25]). This result is likely not a size effect, as the transition temperatures for $PbTiO_3$ and $PbZrO_3$ decrease with decreasing size[26]. However, $PbTiO_3$ is known to show an increased Curie temperature under compressive stresses[27]. It is possible that due to thermal expansion differences between the PZT and the AAM, the nanorods are stressed enough to shift the Curie temperature to the observed value. However, this seems unlikely, as a stress of ~1 GPa is required to shift the Curie temperature by ~100 °C[28], and such a stress would likely crumble the fragile AAM template. Additionally, there could be some degree of phase separation, as a weak shoulder exists at ~400 °C.

3.4 Electrochromic properties of nanorods

The electrochromic response of the nanorods was determined by suspending nanorods in ethanol, and depositing this suspension onto an ITO glass substrate. An

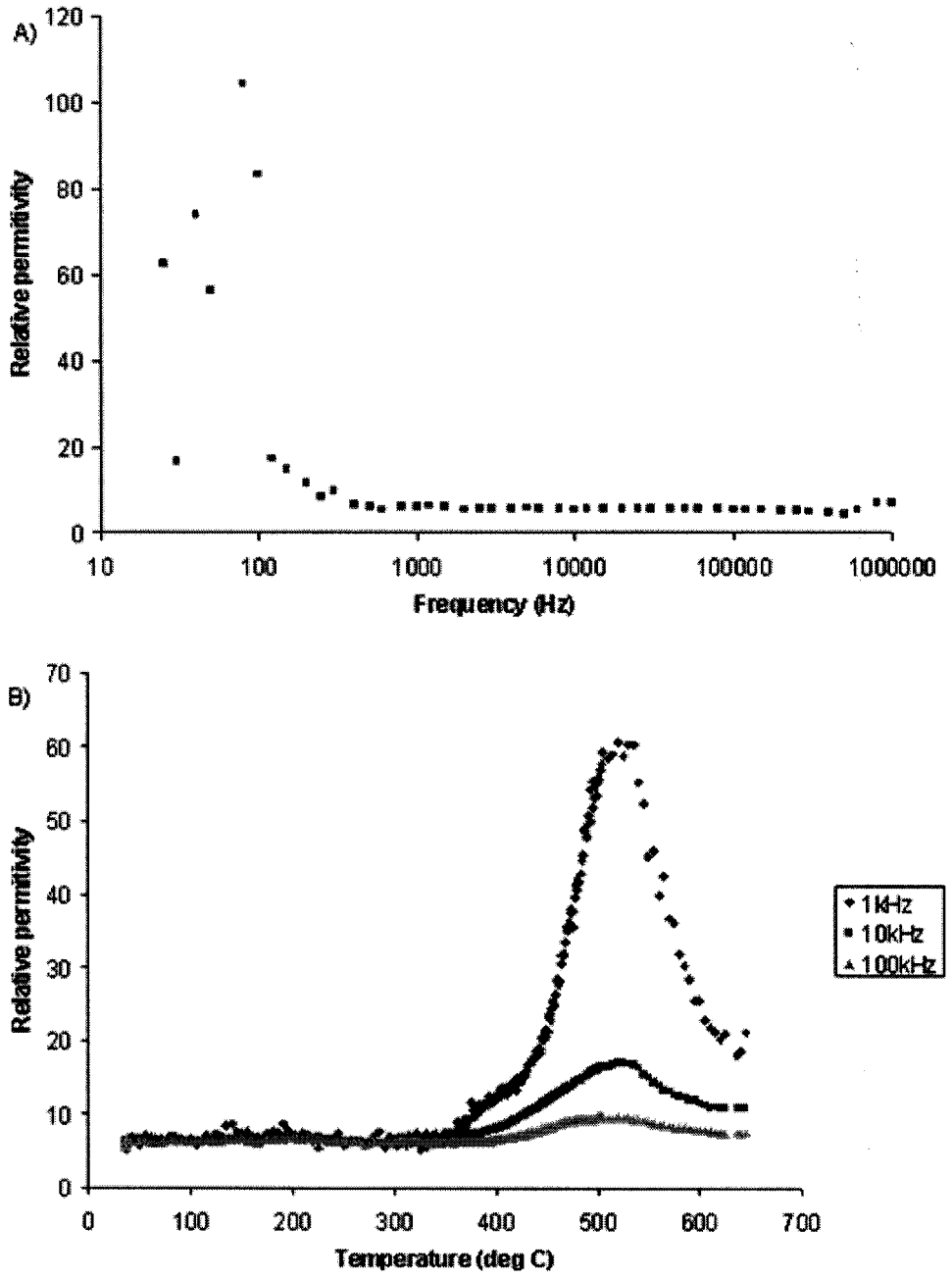

Figure 3-3 Dielectric properties of the PZT nanorod/AAM composite. Permittivity vs. frequency at room temperature is shown in part A, and permittivity vs. temperature is shown in part B.

elastomeric poly(dimethyl siloxane) (PDMS) dam was used to hold the suspension over a localized area of the substrate. The sample was then heated at ~110 °C to evaporate the ethanol, and this was repeated until all of the nanorods were placed on the substrate. This film sample was placed in a cuvette, along with a Pt counter electrode and a 1M solution of $LiClO_4$ in propylene carbonate. Absorbance spectra of the samples were recorded with an Ocean Optics PC-2000 spectrometer, with voltages applied by an HP 6541A DC power supply such that the ITO glass was the cathode.

Figure 3-4 and Figure 3-5 show the electrochromism of 90 nm TiO_2 and 100 nm V_2O_5 nanorods on an ITO glass substrate. For each applied voltage, the sample was held for ~2 min before recording the absorbance. Figure 3-4a shows the optical absorbance of the TiO_2 at three different voltages. Figure 3-4b shows the variation in absorbance (at four different wavelengths) as a function of the applied voltage. From this figure, one can see that the absorbance does not change significantly below a value of 2.8 V, but increases above this point. This figure also shows that the coloration is strongest at a wavelength of 400 nm, and the amount of increase in absorbance decreases with increasing wavelength. Sol-derived TiO_2 films are reported to color either grey or blue, depending on the sol used[29]. The samples here showed a grey coloration, as can be seen in the increases in absorbance across the entire visible spectrum. Although other groups using acetic-acid modified sols have reported a blue coloration, those samples are typically amorphous xerogel films[30]. Since the different (blue) color is from the modified ligand field around Ti, it is unsurprising that a sintered sample (from which the acetate groups are largely removed) would behave differently than the xerogel.

Unlike TiO_2, V_2O_5 nanorods showed a slight decrease in absorbance upon Li^+ ion insertion. Figure 3-5a shows the optical absorbance of V_2O_5 at three different voltages. In Figure 3-5b, one can see the evolution of absorbance in the V_2O_5 sample as a function of applied voltage. V_2O_5 films have a much more complex electrochromic behavior, with reported colorations including yellow↔green or red↔yellow↔green[29], and yellow↔green↔blue[31]. In fact, V_2O_5 can show both anodic and cathodic coloration behavior at some wavelengths upon Li^+ ion intercalation, depending on the

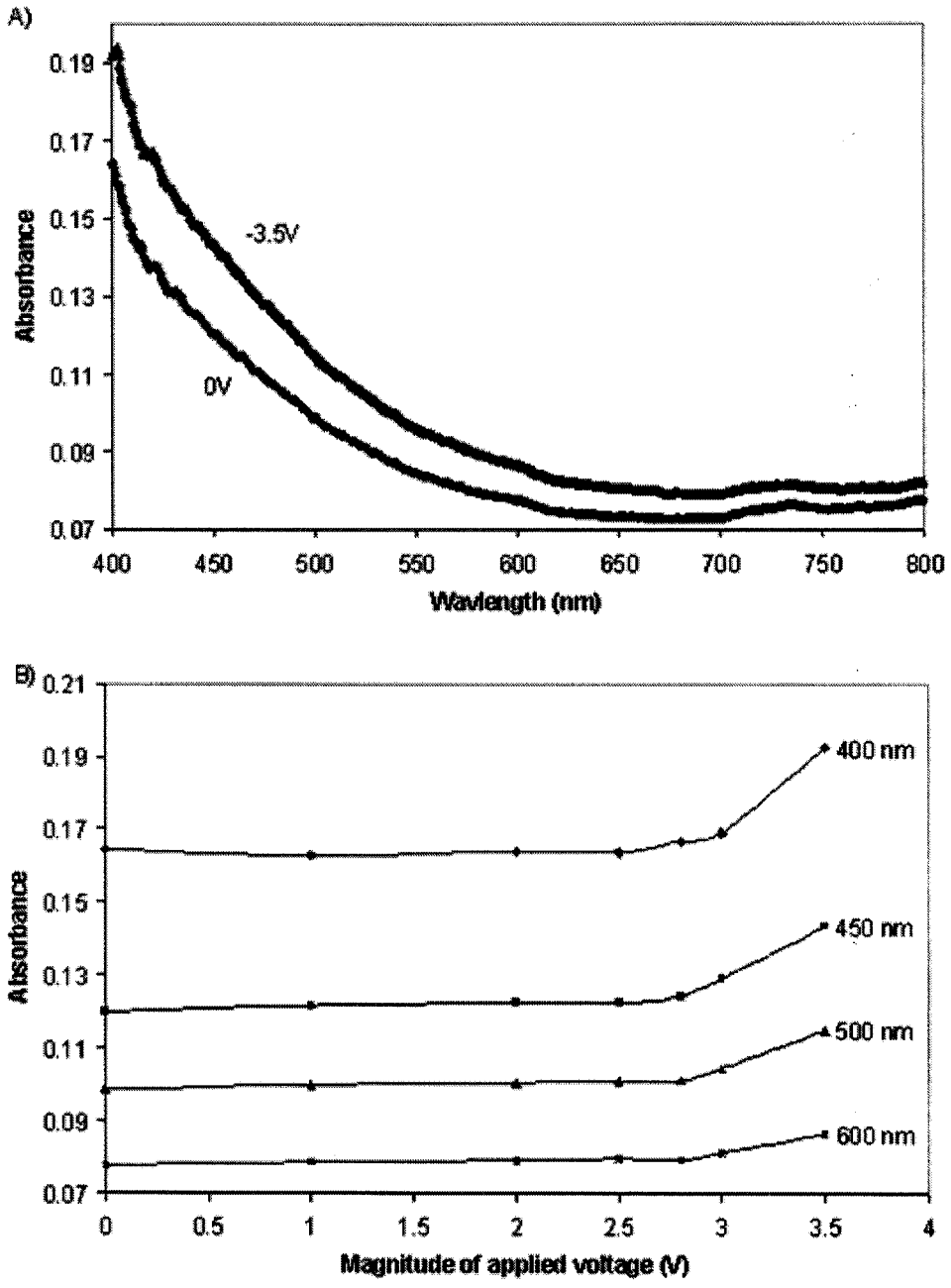

Figure 3-4 Electrochromism of TiO_2 nanorods. Part A shows the optical absorbance of TiO2 under no voltage and -3.5V. Part B shows the variation in absorbance (at four different wavelengths) for TiO2 as a function of applied voltage.

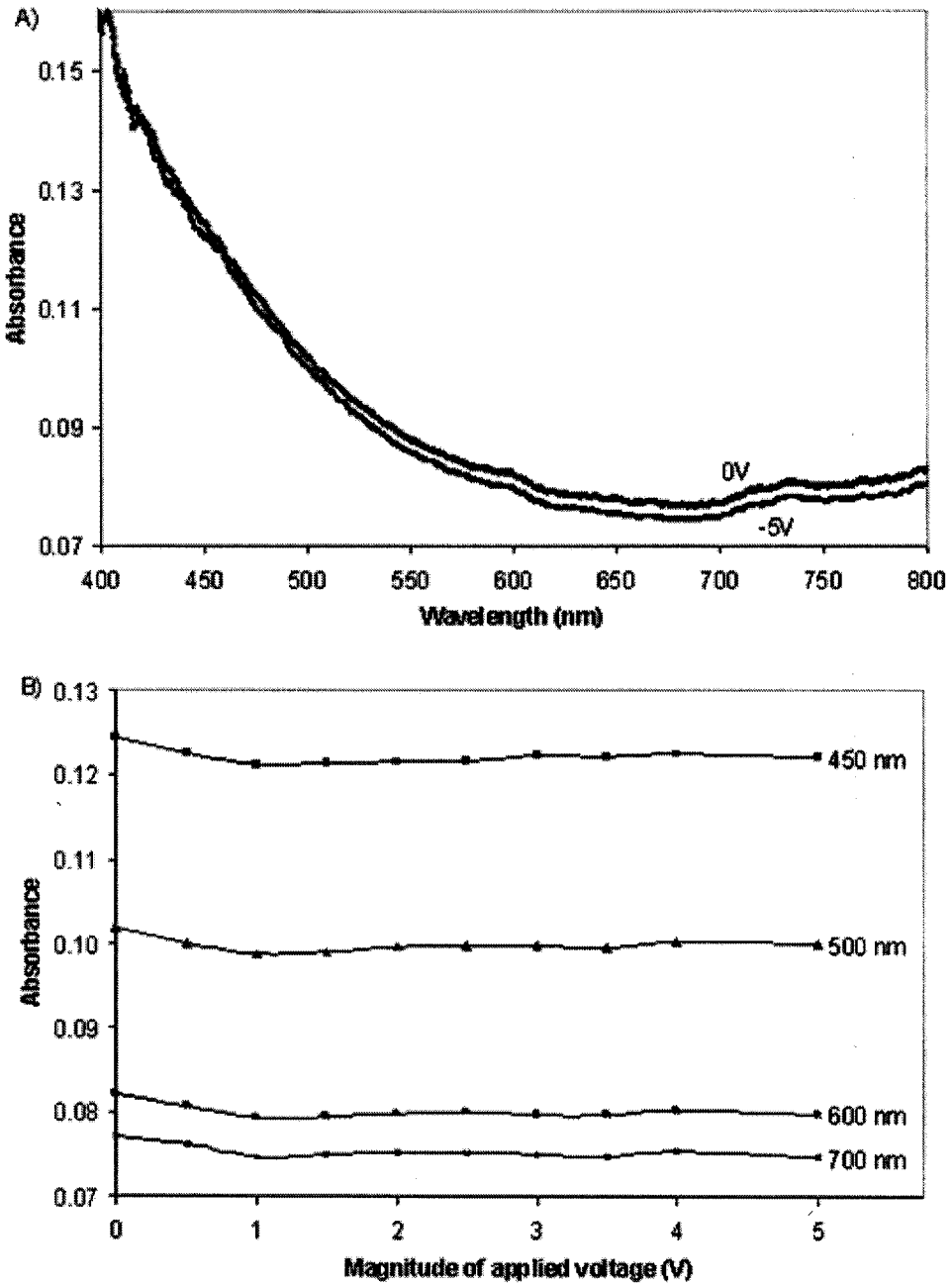

Figure 3-5 Electrochromism of V_2O_5 nanorods. Part A shows the optical absorbance of V2O5 under no voltage and -5V. Part B shows the variation in absorbance (at four different wavelengths) for V2O5 as a function of applied voltage.

degree of intercalation[31]. These facts make it more difficult to understand the results observed, and further study is needed.

3.5 Summary

Research in nanomaterials is driven, in part, by the properties of nanomaterials for two reasons. First is the pure science interest in the novel properties observed at the nanoscale. Second is the potential for applications based on such novel properties. Both of these factors led to the study of selected properties of the nanorods synthesized in this work.

Due to their size, however, individual nanorods are difficult to characterize. As such, some of the properties measured took advantage of the large-area arrays of parallel nanorods synthesized by the sol EPD technique. Large numbers of nanorods still embedded in their template are easily handled, and measurement of the properties of such composites gives valuable insights into the behavior of the nanorods themselves.

From this work, we have determined that ITO nanorods with an apparent conductivity of ~ 5 Ω-cm can be easily synthesized. We have also determined an apparent Curie temperature from PZT nanorod/AAM composites. Lastly, electrochromic behavior has been observed in nanorods of TiO_2 and V_2O_5.

Notes to Chapter 3

[1] Cao, G.Z. In *Nanostructures and Nanomaterials: Synthesis, Properties, and Applications*, Imperial College Press, London, 2004.

[2] Barati, M.; Sadeghi, E. *Nanotechnology* **2001**, *12*, 277.

[3] Pascual, J.I.; Méndez, J.; Gómez-Herrero, J.; Baró, A.M.; Garcia, N.; Landman, U.; Luedtke, W.D.; Bogachek, E.N.; Cheng, H.-P. *Science* **1995**, *267*, 1793.

[4] Zhang, Z.; Sun, X.; Dresselhaus, M.S.; Ying, J.Y.; Heremans, J. *Phys. Rev. B* **2000**, *61*, 4850.

[5] Shaw, T.M.; Trolier-McKinstry, S.; McIntyre, P.C. *Annu. Rev. Mater. Sci.* **2000**, *30*, 263.

[6] Newnham, R.E.; Udayakumar, K.R.; Trolier-McKinstry, S. In *Chemical Processing of Advanced Materials* (Hench, L.L.; West, J.K., Ed.), John Wiley and Sons, New York, 1992.

[7] Prasad, K.V.R.; Raju, A.R.; Varma, K.B.R. *J. Mater. Sci.* **1994**, *29*, 2691.

[8] Shantha, K.; Varma, K.B.R. *J. Am. Ceram. Soc.* **2000**, *83*, 1122.

[9] Kang, B.-S.; Gu-Choi, D.; Choi, S.-K. *J. Mater. Sci.: Mater. Electron.* **1998**, *9*, 139.

[10] Kanzig, W. *Phys. Rev.* **1955**, *98*, 549.

[11] Bachmann, R.; Barner, K. *Solid State Commun.* **1998**, *68*, 865.

[12] Chen, X.; Hu, X.; Feng, J. *Nanostruct. Mater.* **1995**, *6*, 309.

[13] Liu, J.; Coleman, J.P. *Mat. Sci. Eng. A-Struct.* **2000**, *286*, 144.

[14] Bueno, P.R.; Leite, E.R. *J. Phys. Chem. B* **2003**, *107*, 8868.

[15] Patrissi, C.J.; Martin, C.R. *J. Electrochem. Soc.* **1999**, *146*, 3176.

[16] Bueno, P.R.; Leite, E.R.; Giraldi, T.R.; Bulhojes, L.O.S.; Longo, E. *J. Phys. Chem B* **2003**, *107*, 8878.

[17] Chan, C.M.; Cao, G.Z.; Fong, H.; Sarikaya, M.; Robinson, T.; Nelson, L. *J. Mater. Res.* **2000**, *15*, 148.

[18] Guanghui, F.U.; Jiafeng, D.U.; Donghui, P.A.N.; Ouli, H.E. *J. Non-Cryst. Solids* **1989**, *112*, 454.

[19] Alam, M.J.; Cameron, D.C. *Thin Solid Films* **2000**, *377-378*, 455.

[20] Yu, D.; Yu, W.; Wang, D.; Qian, Y. *Thin Solid Films* **2002**, *419*, 166.

[21] Bel Hadj Tahar, R.; Ban, T.; Ohya, Y.; Takahashi, Y. *J. Appl. Phys.* **1998**, *83*, 2631.

[22] Emons, T.T.; Li, J.; Nazar, L.F. *J. Am. Chem. Soc.* **2002**, *124*, 8516.

[23] Li,C.; Zhang, D.; Liu, X.; Han, S.; Tang, T.; Han, J.; Zhou, C. *Appl. Phys. Lett.* **2003**, *82*, 1613.

[24] Rossetti, Jr., G.A.; Cline, J.P.; Navrotsky, A. *J. Mater. Res.* **1998**, *13*, 3197.

[25] Kanno, I.; Hayashi, S.; Kitagawa, M.; Takayama, R.; Hirao, T. *Appl. Phys. Lett.* **1995**, *66*, 145.

[26] Chattopadhyay, S. *Nanostruct. Mater.* **1997**, *9*, 551.

[27] Rossetti, Jr., G.A.; Cross, L.E.; Kushida, K. *Appl. Phys. Lett.* **1991**, *59*, 2524.

[28] Oh, S.H.; Jang, H.M. *J. Appl. Phys.* **1999**, *85*, 2815.

[29] Aegerter, M.A.; Avellaneda, C.O.; Pawlicka, A.; Atik, M. *J. Sol-Gel Sci. Techn.* **1997**, *8*, 689.

[30] Nabavi, M.; Doeuff, S.; Sanchez, C.; Livage, J. *Mater. Sci. Eng. B* **1989**, *3*, 203.

[31] Wang, Z.; Chen, J.; Hu, X. *Thin Solid Films* **2000**, *375*, 238.

4 Formation and properties of gold-coated oxide nanorods

4.1 Introduction

In addition to synthesizing simple one-component nanostructures, much research has gone into synthesis of multi-component systems, such as a (nanoscale) core of one material coated with a (nanoscale) shell of another. Systems such as this are referred to as core-shell nanostructures. Numerous spherical core-shell systems have been studied. Researchers have synthesized core-shell quantum dot structures, where a second semiconductor surrounds the central semiconductor material, which yields tunable optical properties[1,2]. SiO_2 encapsulated Au nanoparticles have been synthesized to show varying absorbance properties[3,4]. Au-coated TiO_2 nanoparticles, as another example, show slight shifts in absorbance peak with varying TiO_2:Au ratios, and have a distinct improvement in photo-catalytic oxidation of thiocyannate[5]. Au-coated SiO_2 particles have been synthesized to show a large number of properties. SiO_2 particles decorated with small Au clusters show differences in optical properties depending on the density of coverage[6]. When the SiO_2 particles are completely covered with Au, it is possible to tune the optical properties over a wide range by varying the core size and shell thickness[7,8,9]. For all of these systems, the optical properties depend strongly on the dimensions of the samples. For instance, the inner and outer diameter of Au shells on SiO_2 or the diameter and length of Ag wires controls the plasmon energies of the samples. This gives these types of structures essentially tunable optical properties, where control over the physical dimensions of a sample gives the desired behavior.

Although much work has been done on spherical core-shell systems, little research has been done on one-dimensional (i.e., rod-like) core shell structures. Some researchers have synthesized semiconductor core-shell rod structures[10], similar to the more common spherical core-shell quantum dot structures. Others have synthesized metal-metal core-shell nanorods[11], which have differing optical properties from those of nanorods of either the core or shell metal alone. In the area of metal-oxide core shell systems, one group has described the synthesis of silica-coated gold nanorods[12], which have differing optical properties from the uncoated gold rods. There is no prior

information in the literature about metal shells on oxide nanorods. This chapter discusses the synthesis and analysis of cylindrical nanoshells of Au formed on nanorods of SiO_2 and TiO_2. First, there is a brief introduction to the phenomena of surface plasmon resonance, and the description of this effect by Mie scattering theory. The template-based synthesis of SiO_2 and TiO_2 nanorods by a combination of sol preparation and electrophoresis is discussed, as well as the formation of an Au layer on the nanorods. Experimental and calculated absorbance spectra are compared for a variety of SiO_2 core diameters and Au shell thicknesses. Some preliminary results for Au shells on TiO_2 cores are also presented.

4.2 Background

The optical properties of these nanorods are due to the excitation of surface plasmons in the gold. The electric field of an incoming light wave induces a polarization of the (free) conduction electrons with respect to the much heavier ionic core of the metal. This coherent excitation leads to a net charge difference being felt at the particle surface, which in turn acts as a restoring force. In this way, a dipolar oscillation of the electrons is created[13]. This is known as the surface plasmon absorption. A simple model of this behavior can be seen in Figure 4-1.

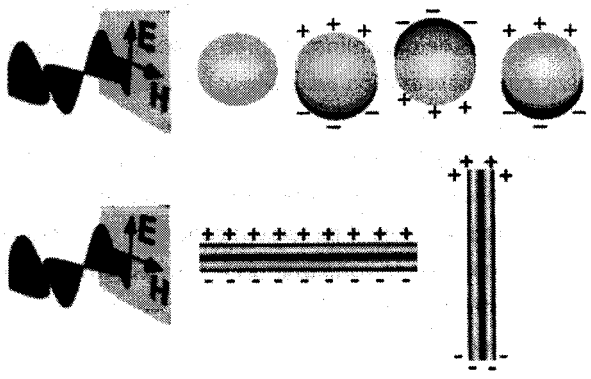

Figure 4-1 (Top) Schematic drawing of the interaction between an electromagnetic field and a metallic nanoparticle. (Bottom) Transverse and longitudinal electron oscillations in a metal nanorod. Taken from Reference 14

A description of this phenomenon was developed by Mie for the description of the observed color in small gold colloids[15]. The basis for this theory is the solution of Maxwell's equations within a metal particle, assuming the dielectric properties vary with frequency as in the bulk metal. A more refined version of the theory comes from allowing that, for small particles, the particle optical properties are size dependant[16]. One model for this behavior is to say that electrons are increasingly scattered at the surface of smaller particles, leading to a reduced effective mean free path length[13].

4.3 Gold coating of oxide nanorods

Oxide nanorods (SiO_2 and TiO_2) are first synthesized as discussed in Chapter 2, then coated with a gold shell. The formation of gold shells on the oxide nanorods is a two-step process. First, it is necessary to modify the surface of the nanorods so that they will have an affinity for gold. This is accomplished by placing amine groups on the nanorod surface. These chemically linked amine groups act as anchor sites to attach gold to the nanorod, which is reduced from solution.

4.3.1 Surface functionalization through self-assembly

Gold coatings on the nanorods are formed in a manner similar to that of Reference 7. The as-synthesized nanorods are suspended in DI water and boiled at 100 °C for ~2 hrs to re-hydrolyze their surface. Boiling silica has been demonstrated to be an effective means of re-hydrolyzing SiO_2 surfaces for the formation of silane self-assembled monolayers[17]. This is required for the self-assembly process to work. When the nanorods are first synthesized (before firing), there are a large number of hydroxide groups on the nanorod surface. These groups are removed (via condensation reactions) upon firing, so it is necessary to re-introduce them to the nanorod surface.

These re-hydrolyzed nanorods are dried to remove excess water, and re-suspended in ethanol. A small amount of 3-aminopropyltrimethoxysilane (APTMS) is added to this suspension. The methoxy groups on the APTMS undergo hydrolysis and condensation reactions with the hydroxyl groups on the nanorod surface:

$$MOH + (MeO)_3 Si - RNH_2 \rightarrow MOSi - RNH_2 + MeOH \qquad \text{Reaction 3-1}$$

to yield the amine-functionalized nanorods. After allowing the APTMS to react for ~ 24 hours, the suspensions are centrifuged and rinsed 4 times to remove excess reactants.

4.3.2 Gold coating of functionalized nanorods

To direct the deposition of gold from solution, small seed particles of gold are first attached to the amine-functionalized nanorods. The seed particles used are from an Au colloidal sol[18]. Briefly, this sol is created by reducing a solution of chloroauric acid and NaOH with tetrakis(hydroxymethyl)phosphonium chloride (THPC). This yields a sol of colloidal Au particles of ~ 2 nm. This sol is mixed with the APTMS-coated oxide nanorods, and left for several hours to allow complete attachment of the Au particles to the nanorods.

Once the Au nanoparticles are completely attached to the nanorods, a coating of Au is formed by reducing a 5mM solution of $HAuCl_4$ with 1mM $NaBH_4$[5], using a varying amount of solution to control the gold shell thickness. The Au seeds attached to the nanorod surface act as nucleation sights for the gold being reduced from solution, so the gold is preferentially deposited on the nanorod surface, rather than heterogeneously nucleating large Au particles in the solution. The gold coating forms over a time span from hours to days, depending on the concentration of the suspension, and the amount of Au and $NaBH_4$ used. Absorbance measurements of some samples show a shift with ageing. For example, 100 nm SiO_2 nanorods coated with 29 nm of gold show an absorbance peak at 547 nm shortly after formation. This peak shifted to 542 nm 8 days later, and remained at 542 nm after an additional 3 weeks.

4.3.3 Analysis of gold-coated nanorods

Figure 4-2 shows micrographs of two sets of the Au-coated nanorods. These images demonstrate the final thickness of the Au-nanorod assembly. Because the samples were not sputtered with a conductive layer prior to FE-SEM analysis, no correction to the measured diameters was needed. From this image, one can also see

that the coverage of gold is nearly uniform over the entire length of the nanorods. This technique was used to determine the Au shell thickness for all of the samples. Table 4-1 lists the combinations of oxide core diameter and Au shell thickness used in this study. The values reported are an average of several tens of values, measured on a digital image. The core diameters have a variation of about ± 15 nm (depending on template), and the shells have an additional variation of about ± 5 nm.

4.4 Optical properties of gold-coated nanorods

The most interesting properties of metal-insulator core-shell systems such as this are in their optical responses. Thus, all of the suspensions of gold-coated nanorods were characterized with UV-Vis absorbance spectroscopy. The absorbance spectra were also calculated to determine if the observed behavior was truly due to the gold coatings as expected.

4.4.1 Observed spectra

For analysis, suspensions of Au-coated nanorods in a mixture of ethanol and water were used. The absorbance spectra were recorded with a UV-Vis spectrometer (Ocean Optics PC2000) using a tungsten-halogen light source (Ocean Optics LS-1). As concentrations of the various nanorod suspensions were not constant, all spectra have

Figure 4-2 SEM micrographs of Au-coated SiO_2 nanorods. Left, 100 nm SiO2 with 22 nm of Au. Right, 100 nm SiO2 with 24 nm of Au.

Table 4-1 Combinations of oxide core diameter and Au shell thickness studied.

Core Material	Core Diameter (nm)	Au shell thickness (nm)
SiO_2	100	31
SiO_2	100	29
SiO_2	100	28
SiO_2	100	24
SiO_2	100	23
SiO_2	100	22
SiO_2	100	21
SiO_2	100	15
SiO_2	200	34
SiO_2	200	32
SiO_2	200	13
SiO_2	200	12
SiO_2	200	6
TiO_2	180	4
TiO_2	90	27

been normalized to have a peak height of 1. For comparison, the spectrum of the initial Au colloidal particles was also recorded. As expected, it shows no strong plasmon features, but rather a broad shoulder extending into the UV[18].

4.4.1.1 SiO_2

Figure 4-3 is a comparison of absorbance spectra for 100 nm SiO_2 nanorods coated with varying amounts of gold. In these samples, the absorbance peak decreases

from 571 nm for a 28 nm shell, to 568 for a 22 nm shell, to 557 nm for a 15 nm shell.. The spectra for 200 nm diameter SiO_2 cores are shown in Figure 4-4. For these, the absorbance peak decreases from 581 nm for a 34 nm shell, to 550 for a 12 nm shell, to a broad shoulder near ~520 nm for a 6 nm shell. Some of the peak breadth in these spectra may be from the slight spread in size of the nanorods. Although they are all ~ 10 μm in length when synthesized, some nanorods do break during sonication or stirring. Since the length of the rod does have a small effect on the absorbance properties, the broken rods broaden the absorbance peak somewhat. Figure 4-6 shows the variation in peak position for the two different core sizes. Another way to compare these data sets is to look at the variation of peak wavelength with shell:core ratio (that is, the shell thickness divided by the core diameter), as seen in Figure 4-5.

4.4.1.2 TiO_2

Because of the difference in dielectric constant between SiO_2 and anatase (about 2.1 and 6.3, respectively)[19], it is expected that these rods will have somewhat different peak positions for the same core-shell ratios. Figure 4-7 shows the preliminary data for these rods, comparing the spectra for two TiO_2 nanorod samples. The 180 nm diameter rod coated with 4 nm of Au shows a peak at 548 nm, and the 90 nm diameter rod with a 27 nm shell has a peak at 536 nm.

4.4.2 Calculated spectra

It is known that the absorbance behavior of metal nanorods can be modeled by Mie scattering theory, considering them as prolate spheroids with the given length and maximum diameter[13]. A similar model has also been shown for SiO_2 on Au nanorod core-shell structures[12]. This model should also be applicable for the Au on SiO_2/TiO_2 nanorods used in this study. Because core-shell nanorods are 1-D nanostructures, their optical properties are a combination of both nanosize and bulk effects. Along the radial dimension of these structures, the behavior is constrained by the size, but along the

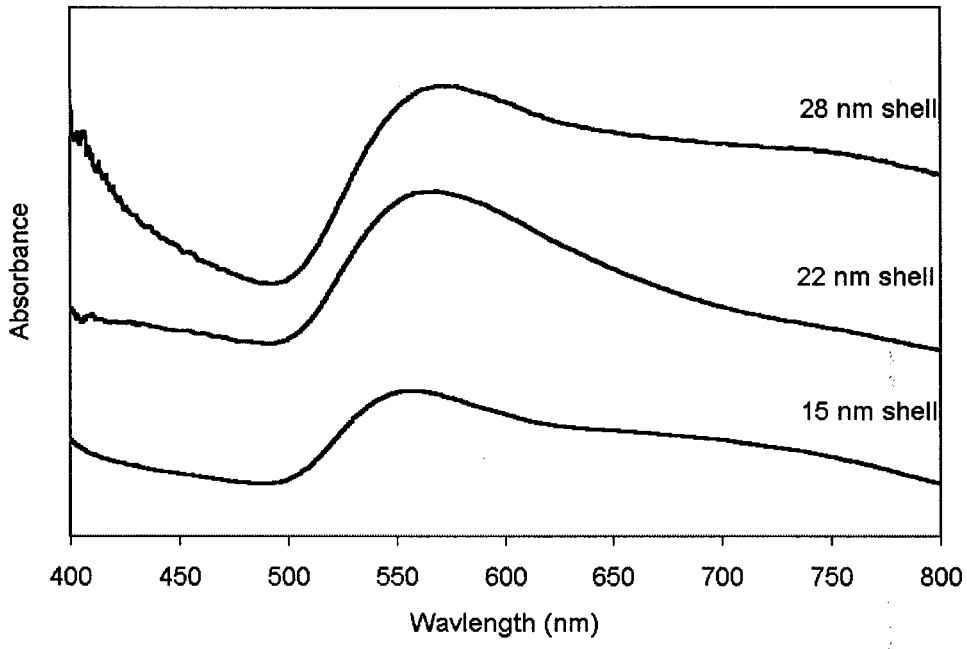

Figure 4-3 Absorbance spectra for Au-coated 100 nm SiO_2 nanorods.

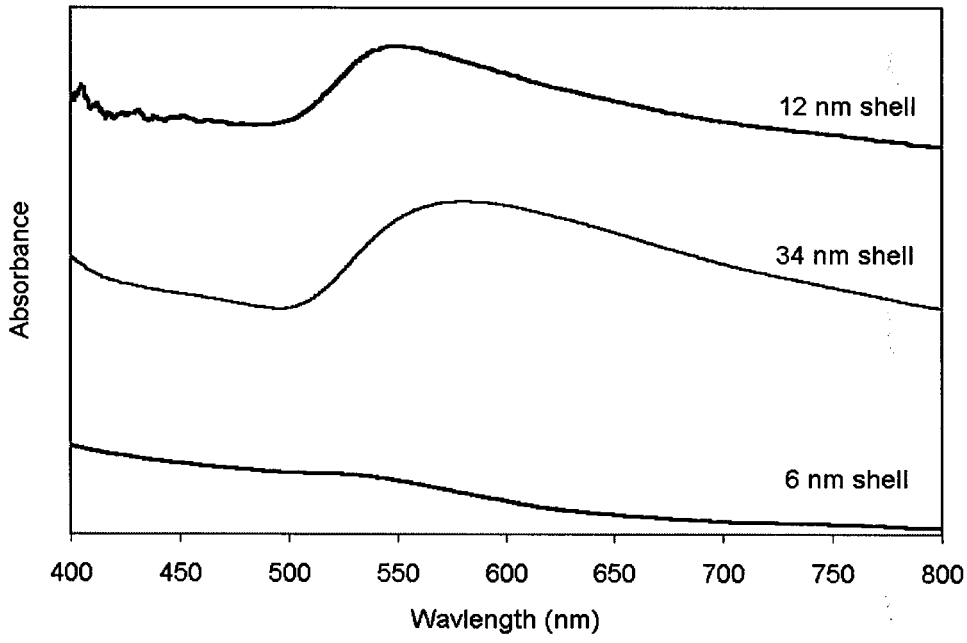

Figure 4-4 Absorbance spectra for Au-coated 200 nm SiO_2 nanorods

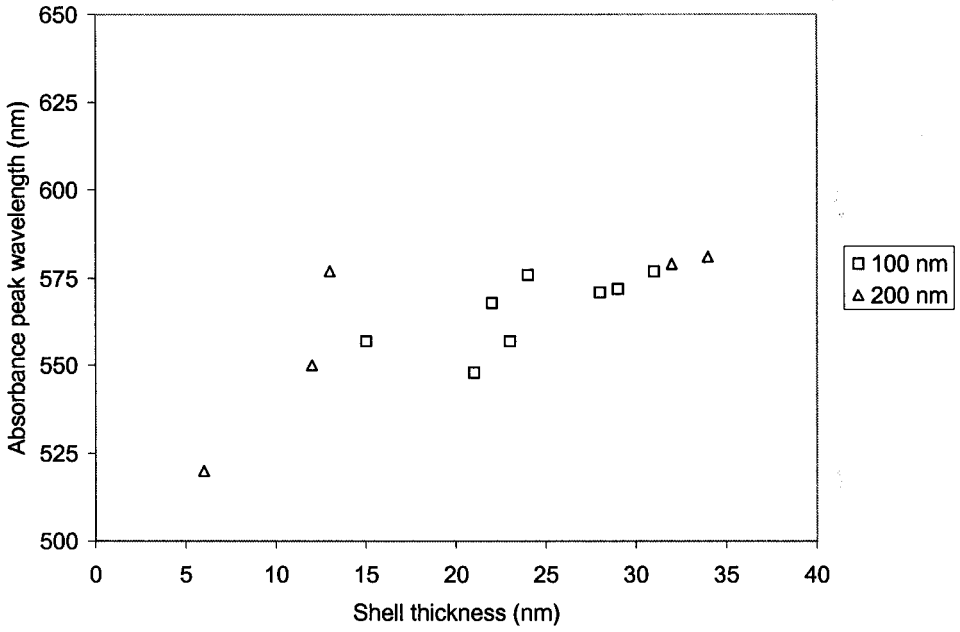

Figure 4-5 Variation in absorbance peak wavelength vs. shell:core ratio

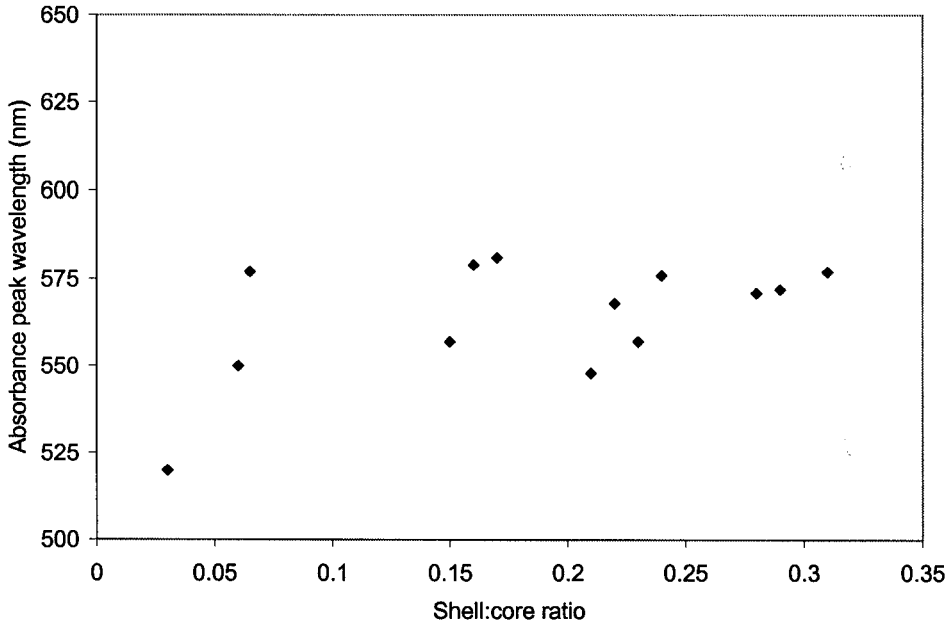

Figure 4-6 Variation in absorbance peak wavelength vs. Au shell thickness

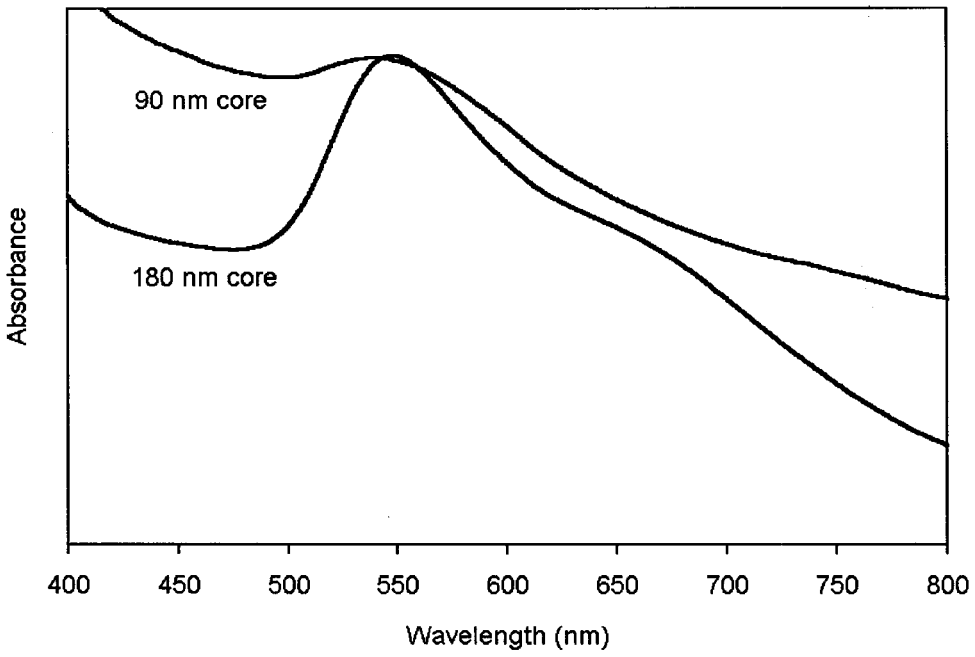

Figure 4-7 Absorbance spectra for Au-coated TiO_2 nanorods.

length (assuming a large enough aspect ratio), the properties are like that of a bulk material[20]. This assumption simplifies the scattering model. The Drude-Lorentz-Sommerfeld model for the dielectric function can be used for the longitudinal dielectric properties of the nanorod[16], incorporating the interband portion fitted from the bulk optical properties of Au[19] in the visible region. Along the radial direction, however, the Drude model also needs to include a modified electron mean free path, to account for the gold shell thickness[16]. Using these dielectric functions and the appropriate shape factors for a rod-like geometry in the polarizability equation for a core-shell system allows one to calculate the scattering behavior of the Au-coated nanorods. Combining all of these considerations leads to the following equations for the calculated absorbance:

$$\sigma(\lambda) = \frac{2\pi\varepsilon_m^{1/2}}{\lambda} \mathrm{Im}[\alpha_l + 2\alpha_t] \qquad \textbf{Equation 4-1}$$

where ε_m is the matrix (solvent) dielectric constant, and α_l and α_t are the longitudinal and transverse polarizabilities. They are functions of the core, shell, and matrix (complex) dielectric constants, and calculated as:

$$\alpha_{l,t} = \frac{V(\varepsilon_s - \varepsilon_m)\{\varepsilon_s + [(\varepsilon_c - \varepsilon_s)(P^1_{l,t} - P^2_{l,t})]\} + f\varepsilon_s(\varepsilon_c - \varepsilon_s)}{\{\varepsilon_s + (\varepsilon_c - \varepsilon_s)(P^1_{l,t} - fP^2_{l,t})][\varepsilon_m + (\varepsilon_s - \varepsilon_m)P^2_{l,t}]\} + fP^2_{l,t}\varepsilon_s(\varepsilon_c - \varepsilon_s)} \quad \textbf{Equation 4-2}$$

where V is the total (core plus shell) volume per particle, ε_s and ε_c are the shell (Au) and core (SiO_2 or TiO_2) dielectric constants, and f is the volume fraction of the core. The four values of P are the depolarization factors, where the superscripts 1 and 2 refer to the core and shell, respectively, and the subscripts l and t are for the longitudinal and transverse modes. With r the core radius, l the particle length and t_s the Au shell thickness, these depolarization values are calculated from:

$$P^1_l = \frac{1 - e_c^{\,2}}{e_c^{\,2}}\left[\frac{1}{2e_c}\ln\left(\frac{1+e_c}{1-e_c}\right)\right] \quad \textbf{Equation 4-3}$$

$$P^1_t = \frac{1 - P^1_l}{2} \quad \textbf{Equation 4-4}$$

$$P^2_l = \frac{1 - e_s^{\,2}}{e_s^{\,2}}\left[\frac{1}{2e_s}\ln\left(\frac{1+e_s}{1-e_s}\right)\right] \quad \textbf{Equation 4-5}$$

$$P^2_t = \frac{1 - P^2_l}{2} \quad \textbf{Equation 4-6}$$

The e values are shape factors, and are calculated for the core (c) and shell (s) as:

$$e_c^2 = 1 - r^2 \Big/ \left(\tfrac{1}{2}\right)^2 \quad \textbf{Equation 4-7}$$

$$e_s^2 = 1 - \frac{(r + t_s)^2}{(\frac{l}{2} + t_s)^2}$$ **Equation 4-8**

with r the core radius, t_s the shell thickness and l the length of the core/shell nanorod.

These calculations assume a random orientation of the nanorods in the solvent. Calculations were done assuming a nanorod length of 10 μm. Although some of the rods were observed to be shorter than assumed, the calculated data give a good fit to experimental. For instance, assuming a length of 5 μm in the calculation for 32 nm of Au on 200 nm SiO_2 only shifts the peak position ~ 4 nm. This is because the length has only a weak influence on the calculated absorbance band, which is due to the transverse plasmon absorbance. Longitudinal absorbance would be shifted into the IR, outside the range of our measurements, therefore the calculations were not done for that peak. A sample calculated spectrum for 100 nm SiO_2 nanorods coated with 23 nm Au is shown in Figure 4-8.

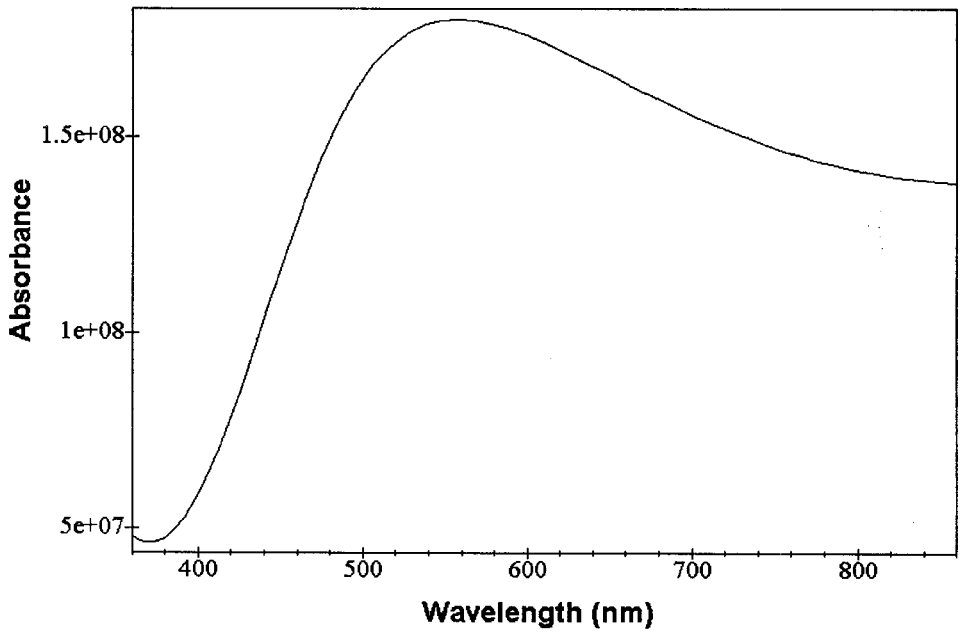

Figure 4-8 Calculated absorbance for 100 nm SiO_2 rod coated with 23 nm Au.

4.4.3 Comparison between measured and calculated spectra

Figure 4-10 and Figure 4-9 compare the experimental and calculated absorbance spectra for 22 nm Au/100 nm SiO_2 and 34 nm Au/200 nm SiO_2 samples respectively, showing the good fit of the calculated spectra to the observed ones. Figure 4-11 compares the experimental and calculated absorbance spectra for 180 nm TiO_2 cores with a 4 nm Au shell thickness, showing the similarities between observed and calculated peak positions. While most of the observed and calculated peak positions are quite close, the overall shapes of the calculated and observed spectra are not in as good of agreement as seen for spherical core-shell systems[7]. Part of this discrepancy is due to the way that the optical properties of gold were fitted. Since only data for the visible part of the spectrum were used, the calculations are applicable in the visible, which might account for the discrepancies near the UV. Also, the measured spectra were not corrected for the slight steady decrease in absorbance due to the cuvette and solvent seen in samples without the core-shell nanorods (See Figure B-5, Appendix B).

Table 4-2 lists a comparison of the calculated and observed peak positions for all the SiO_2 samples in this study. From this, one can observe some trends in the absorbance behavior of the SiO_2 samples. First, for a given core diameter, the absorbance peak wavelength (both observed and calculated) increases as the shell thickness increases. For a given ratio of core thickness to shell diameter, however, the value of the peak position is roughly the same, regardless of the core diameter. This is true for both the calculated and measured values, as seen in Figure 4-12. For example, 100 nm SiO_2 rods coated with 15 nm of Au have observed and calculated peak positions of 557 nm and 520 nm respectively. This is close to the values for 200 nm SiO_2 coated with 32 nm Au (core:shell ratio of 0.16) of 579 nm observed and 522 nm calculated. Similar results are seen for all SiO_2 samples. In addition, the difference between observed and calculated position is larger for 200 nm cores than for 100 nm SiO_2. Overall, the agreement between measured and calculated peak positions is much better for larger shell:core ratios. Thus, there may be problems with the thinnest shells. For samples with thin shells, it is quite likely that the coverage of the nanorod is incomplete. Halas et al. have noticed that it is difficult or impossible to achieve complete Au shells

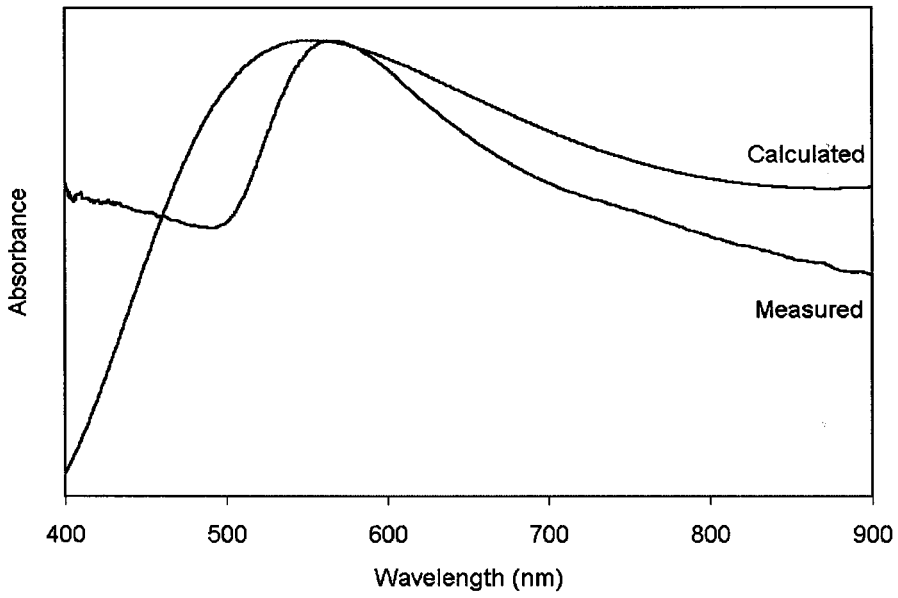

Figure 4-10 Comparison of the experimental and calculated absorbance spectra for 100 nm SiO_2 nanorods coated with 22 nm Au.

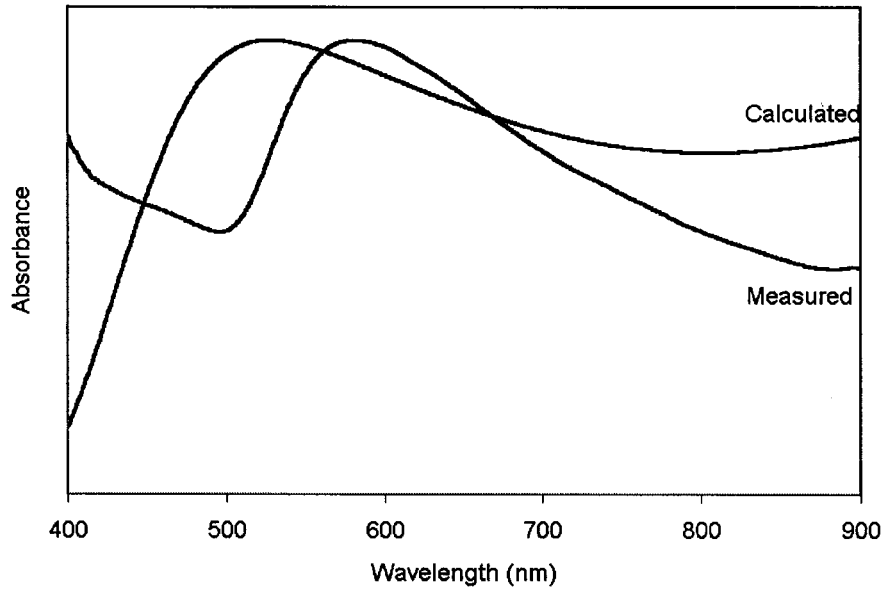

Figure 4-9 Comparison of the experimental and calculated absorbance spectra for 200 nm SiO_2 nanorods coated with 34 nm Au.

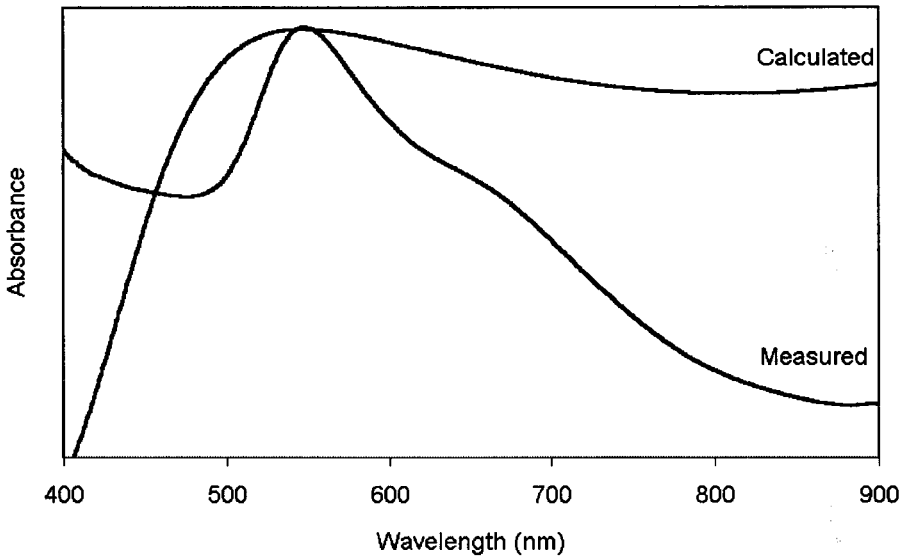

Figure 4-11 Comparison of the experimental and calculated absorbance spectra for 180 nm TiO_2 nanorods coated with 4 nm of Au.

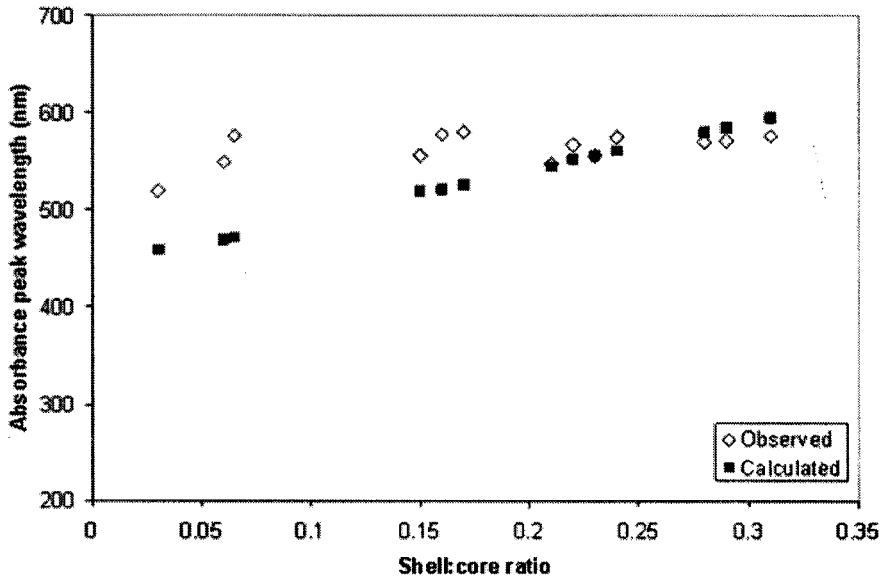

Figure 4-12 Comparison of measured and calculated peak maxima vs. shell:core ratio

Table 4-2 Comparison of the observed and calculated peak positions for Au-coated SiO_2 nanorods.

Sample	Observed peak position (nm)	Calculated peak position (nm)
31 nm Au / 100 nm SiO_2	577	596
29 nm Au / 100 nm SiO_2	572	586
28 nm Au / 100 nm SiO_2	571	581
24 nm Au / 100 nm SiO_2	576	562
23 nm Au / 100 nm SiO_2	557	557
22 nm Au / 100 nm SiO_2	568	553
21 nm Au / 100 nm SiO_2	548	546
15 nm Au / 100 nm SiO_2	557	520
34 nm Au / 200 nm SiO_2	581	527
32 nm Au / 200 nm SiO_2	579	522
13 nm Au / 200 nm SiO_2	577	472
12 nm Au / 200 nm SiO_2	550	470
6 nm Au / 200 nm SiO_2	Broad shoulder near ~ 520	459

of less than ~ 10 nm thickness on SiO_2 nanoparticles[7]. Thus, the wider discrepancies seen in the thinnest shells (6nm Au / 200 nm SiO_2 and 4 nm Au / 180 nm TiO_2) are likely caused by the formation of incomplete shells.

There are a few explanations for the discrepancies between the calculated and observed spectra. First, it is assumed that all the core-shell structures are uniform in size, but in actuality, there is a certain amount of spread in the core diameters. This could lead to a certain amount of peak broadening/shifting. Similarly, there is likely a spread of lengths of the structures, which would have a small effect on the observed spectra.

It is possible that when the spectra were recorded, the core-shell structures were poorly dispersed in the solution. If there were clusters of the nanorods in the liquid (agglomerated by van der Waals interactions, for example), that would alter the absorbance observed, as coupling between the structures shifted the absorbance peak to higher wavelengths. A similar problem would be the existence of bundles of nanorods completely enclosed in Au. Although this was not observed in the SEM, it may have occurred, and would further shift the absorbance behavior.

Lastly, there are potentially some slight difficulties with the model itself. The interband terms used were fitted from real data to a sixth order polynomial, which may not have accurately captured all of the behavior of the dielectric constant of gold over the wavelength interval of interest. In addition, the dielectric constant used for the medium is an approximate value for a mixture of ethanol and water. It is known that higher values of the medium dielectric constant will shift the absorbance peak to higher wavelengths. Although this value has only a slight effect on the calculated values, when combined with the other factors mentioned above, it might contribute somewhat to the discrepancies noted. In the calculated spectra for TiO_2 cores, the dielectric function used to TiO_2 was partly inaccurate. First, though the value used (6.3) is correct for bulk anatase, amorphous, poorly crystalline or porous samples can have dielectric constants as low as 4 or 5[21,22]. Additionally, anatase TiO_2 is a semiconductor with a band-gap of about 3.2 eV[23], or ~390 nm. Thus, there is a strong absorbance due to TiO_2 at lower wavelengths, which is not accounted for in the model.

4.5 Conclusions

Through a combination of sol-gel chemistry, electrophoresis, and self-assembly, it is possible to grow oxide nanorods with a thin shell of gold on their surface. By varying the diameter of the oxide rods, and the thickness of the Au coating, it is possible to tune the optical properties of these structures. For instance, changing from a 100 nm SiO_2 nanorod with 31 nm of Au coating to a 200 nm with 32 nm of Au induces a shift in the absorbance peak from 577 to 579 nm. Similarly, changing the thickness of Au coating on 100 nm SiO_2 nanorods from 15 to 31 nm shifts the absorbance peak from 557 to 577 nm. Changing the core material can also alter the optical properties of these core-shell structures. This can be seen in a change from SiO_2 (with a dielectric constant of ~2.1) to anatase TiO_2 (with a dielectric constant of ~6.3). 200 nm SiO_2 nanorods with 6 nm of Au have an absorbance shoulder near 525nm, where 180 nm TiO_2 nanorods with 4 nm of Au have a peak at 548 nm.

These results suggest that the formation of a general class of oxide-metal core-shell systems should be possible, giving 4 degrees of freedom in tuning the optical properties: core material, core diameter, shell material and shell thickness. Already a wide variety of core oxides can be formed into nanorods by sol electrophoresis. These nanorods could be easily functionalized to have amine or thiol groups on their surfaces to bind with the desired metal. Lastly, a metal colloid (such as Au, Ag and Pt) can be chosen as a seed for chemical deposition of the shell.

The absorbance spectra of the core-shell structures synthesized can also be calculated using Mie scattering theory. It was found that all but one sample followed the calculated trend of increasing absorbance peak position with increasing Au shell thickness. The calculated spectra show good agreement with the measured results. For example, in the SiO_2 nanorods, there was an average difference of about 24 nm between the observed and calculated spectra.

Notes to Chapter 4

[1] Dabbousi, B.O.; Rodriguez-Viejo, J.; Mikulec, F. V.; Heine, J.R.; Mattoussi, H.; Ober, R.; Jensen, K.F.; Bawendi, M.G. *J. Phys. Chem. B* **1997**, *101*, 9463.

[2] Yoffe, A.D. *Adv. Phys.* **2001**, *50*, 1.

[3] Hall, S.R.; Davis, S.A.; Mann, S. *Langmuir* **2000**, *16*, 1454.

[4] Caruso, F.; Spasova, M.; Salgueiriño-Maceira, V.; Liz-Marzán, L.M. *Adv. Mater.* **2001**, *13*, 1090.

[5] Dawson; A.; Kamat, P.V. *J. Phys. Chem. B* **2001**, *105*, 960.

[6] Westcott, S.L.; Oldenburg, S.J.; Lee, T.R.; Halas, N.J. *Langmuir* **1998**, *14*, 5396.

[7] Oldenburg, S.J.; Averitt, R.D.; Westcott, S.L.; Halas, N.J. *Chem. Phys. Lett.* **1998**, *288*, 243.

[8] Oldenburg, S.J.; Hale, G.D.; Jackson, J.B.; Halas, N.J. *Appl. Phys. Lett.* **1999**, *75*, 1063.

[9] Oldenburg, S.J.; Jackson, J.B.; Westcott, S.L.; Halas, N.J. *Appl. Phys. Lett.* **1999**, *75*, 2897.

[10] Manna, L.; Scher, E.C.; Li, L.-S; Alivisatos, A.P. *J. Am. Chem. Soc.* **2002**, *124*, 7136.

[11] Ah, C.S.; Hong, S.D.; Jang, D.-J. *J. Phys. Chem. B* **2001**, *105*, 7871.

[12] Shih, C.-W.; Lai, W.-C.; Hwang, C.-C.; Chang, S.-S.; Wang, C.R.C. In *Metal Nanoparticles* (Feldham, D.L.; Foss, Jr., C.A., Ed.), Marcel Dekker, Inc., New York, N.Y., 2002.

[13] Link, S.; El-Sayed, M.A. *Int. Rev. Phys. Chem.* **2000**, *19*, 409.

[14] Liz-Marzan, L.M., *Materials Today* **2004**, *7*, 26.

[15] Mie, G. *Ann. Phys.* **1908**, *25*, 329.

[16] Kreibig, U.; Vollmer, M. *Optical Properties of Metal Clusters*; Springer-Verlag, Berlin, 1995.

[17] Feng, X.; Fryxell, G.E.; Wang, L.-Q.; Kim, A.Y.; Liu, J.; Kemner, K.M. *Science* **1997**, *276*, 923.

[18] Duff, G.; Baiker, A.; Edwards, P.P. *Langmuir* **1993**, *9*, 2301.

[19] Lide, D.R., Ed. *CRC Handbook of Chemistry and Physics, 74th ed.*, CRC Press, Boca Raton, 1994.

[20] Sun, Y.; Gates, B.; Mayers, B.; Xia, Y. *Nano Lett.* **2002**, *2*, 165.

[21] Mardare, D.; Hones, P. *Mat. Sci. Eng. B* **1999**, *68*, 42.

[22] Won, D.-J.; Wang, C.-H.; Jang, H.-K.; Choi, D.-J. *Appl. Phys. A* **2001**, *73*, 595.

[23] Mosaddeq-ur-Rahman, M.; Yu, G.; Krishna, K.M.; Soga, T.; Watanabe, J.; Jimbo, T.; Umeno, M. *Appl. Optics* **1998**, *37*, 691.

5 Summary and Future work

The previous chapters have outlined the types of methods one could use for synthesizing nanorods, laid out a rationale for using the technique of sol electrophoresis, and demonstrated how the method works by synthesizing a number of oxide nanorods. There remain a number of areas of research that need to be investigated with respect to this project. This chapter outlines the different areas of work that one could pursue to continue this project.

5.1 Summary

The three main accomplishments of this work are: development of the sol electrophoretic deposition in templates method for formation of oxide nanorods; property measurements on such synthesized nanostructures; and the use of these nanorods to from more complex core:shell nanostructures. While electrophoresis of sols has long been used in film formation, no previous had developed sol EPD as a method for nanorod synthesis.

5.1.1 Template synthesis

The primary contribution of this work is the development of a new technique for the synthesis of oxide nanorods. Sol electrophoretic deposition in is a simple, flexible technique that can be used to synthesize a wide variety of oxide nanorod materials. While it is not a perfect method for every desired product, it has a large number of advantages that make it a very appealing method. For example, the ability to grow large area arrays of uniformly sized and nearly unidirectional aligned nanorods of various oxides. It is also believed to yield a more dense oxide nanorod prior to sintering than sol-gel without electrophoresis. Additionally, through careful control of the sol chemistry, nanorods of complex oxides are possible. Table 5-1 lists a comparison of the advantages and disadvantages of this synthesis method.

A wide variety of oxide nanorods, with diameters from ~45-200 nm and lengths of about 10-60 μm, were grown to demonstrate the ease and flexibility of the sol EPD

Table 5-1 Advantages and disadvantages of sol EPD for oxide nanorod synthesis

Advantages	Comments
Uniform size, easily controlled by selection of template	
Unidirectional alignment	Unlike many non-template solution methods, where the nanorods are randomly dispersed in a solvent
Large area arrays possible	
Simple experimental setup	Only requires supplies found in many labs, no specialized equipment
Inexpensive	
Simple and complex oxides	Few other techniques offer a general synthesis of all oxide materials
Disadvantages	
Require sintering to make dense and crystallize	
Polycrystalline	While not a disadvantage for all applications, in some situations single crystal nanorods would be preferred
Possible microstructure gradients	
Must control chemistry to obtain desired product	For complex oxides, homocondensation must be avoided

technique. Both simple and complex oxides were made, with a number of different functional properties available in the various oxides.

To better understand the growth of the oxide rods formed by this technique, many possible processing parameters were varied to see their effect on the final product. It was determined that particle charge, template charge (both through the sol pH),

deposition rate, condensation reactions and chemical additives all have a strong influence on the final product.

5.1.2 Property measurements

One of the chief reasons for interests in 1-D oxide nanostructures is their interesting potential for combinations of nanoscale and bulk properties. However, direct observation of such effects can often be difficult. One way around this difficulty is to measure macroscopic properties (bulk resistance, bulk dielectric constant) of large numbers of nanorods, which still show the interesting size-related behavior.

One example is conductivity measurements in the transparent conducting oxide material ITO. As the diameter of such rods decreases, scattering effects may begin to alter the conductivity. The direct measurement of individual rod properties is quite difficult, however. As a compromise, the properties of the rods were determined while still embedded in the AAM template, allowing for easier measurement. The measured apparent resistivity of ~5 Ω-cm is higher than that normally seen in films (but better than what has been observed in mesoporous samples) which may in part be due to the crude measurement techniques used.

Another example is the dielectric/ferroelectric properties of PZT nanorods. These samples were also analyzed in composite form, and were found to exhibit a peak in the dielectric constant-temperature cure at a much higher temperature than expected, possible due to stress effects or phase separation.

5.1.3 Core:shell nanorods

An interesting adaptation of the nanorods synthesized in this work is the further coating of nanorods with metallic shells to form interesting core:shell composite materials. By varying the diameter of the oxide rods, and the thickness of the Au coating, it is possible to tune the optical properties of these structures. These results suggest that the formation of a general class of oxide-metal core-shell systems should be possible by combining sol-gel electrophoresis with template growth.

5.2 Future work

5.2.1 Processing parameters

While the proceeding work focused on a large number of processing parameters, and their influence on the nanorod growth, there are still parameters that have been left unexplored. Two major areas left are the influence of template pore size, and the size of the sol nanoparticles.

Thus far, the assumption has been that pore size has no influence on the process of nanorod growth. While the driving for capillary action increases with decreasing pore size, the rate of filling also decreases with decreasing pore size. Additionally, there is some concern that the equations used to describe the behavior of sol nanoparticles inside the pores may change when the pore size becomes small enough (although calculations for pores down to ~10 nm agree quite well with experiment[1]). Thus, it would be of interest to examine the template pore size effect, particularly for very small pores.

There has also been no study on the influence of particle size in the formation of nanorods. However, one can image that the particle size will have a strong influence, since the mobility is related to particle size (at least for particles such that $\kappa a < \sim 10^3$). By taking advantage of techniques such as small angle x-ray scattering and/or or dynamic light scattering[2], one could easily determine the size of the sol nanoparticles. By aging the sols and tracking the increase in particle size, one could study the effect of particle size on nanorod synthesis by sol EPD.

5.2.2 Synthesis of doped oxide nanorods

One of the reasons oxide materials are useful is that their properties can be altered/enhanced by appropriate doping with other oxides. These enhanced possibilities from doping in oxides leads to a natural interest in the synthesis of doped oxide nanorods. One example of a doped material of interest is vanadium-doped titanium dioxide, $Ti_{1-x}V_xO_2$. This semiconductor has a band gap that is dependant on the quantity

x of V doped into the system[3], and shows enhanced catalytic activity over undoped TiO_2[4].

There are a number of potential difficulties to be overcome in the synthesis of such doped oxide nanostructures. First, it has been observed that in many nanostructures, the dopant atoms will tend to diffuse to the surface[5], which can be understood by the increase of surface-to-volume ratio as a material decreases in size. A second potential difficulty is related to the sol-gel processing of materials. As more species are incorporated into a sol, the possibility of homo-condensation and phase separation increases. This problem, however, is the same for both doped materials and complex oxides, so given the previous success in the synthesis of complex oxide nanorods; I believe that this obstacle can be overcome. The chief processing technique will be a careful control of the sol preparation conditions, so that hetero-condensation predominates and phase segregation is avoided. For example, in the $Ti_{1-x}V_xO_2$ system mentioned above, both of the precursors are highly reactive, and hetero-condensation could be hard to achieve. One way to get around this might include partially hydrolyzing the less reactive precursor before combining it with the more reactive precursor. If done correctly, this could lead to condensation reactions between the two species, and the formation of, for instance, Ti-V oligomeric alkoxides. Further hydrolysis and condensation of these species would incorporate Ti-O-V linkages, and phase separation could be avoided.

5.2.3 Valence control

Many of the oxides synthesized thus far (or planned for the future) contain transition metal ions that have multiple possible oxidation states. In order to achieve a desired crystalline phase, and thus materials property, etc., it will be important in some cases to control the valence state of the relevant ions. One example is that of V^{5+}/V^{4+}. Both of these oxidation states are of potential interest, as V_2O_5 is electrochromic and useful for Li^+ ion batteries, while VO_2 undergoes a massive change in its electrical conductivity near 67 °C[6]. Thus, there are a number of reasons to try to control the V ion oxidation state.

Two methods will be investigated for controlling the valence state of ions in oxide nanorods. First, materials can be simply subjected to appropriate heat treatments under oxidizing or reducing conditions to obtain the desired valence state. This works quite well for the conversion of V^{5+} to V^{4+}, for example[6]. Secondly, by working with precursors which have the desired oxidation state, materials can be synthesized maintaining that valence. For example, by using V^{4+} precursors, Zhao et al synthesized $Ti_{1-x}V_xO_2$ where V^{4+} remained in the TiO_2 matrix even when the $Ti_{1-x}V_xO_2$ was heated at 600-800°C in air[3].

5.2.4 Synthesis of single-crystal nanorods

All of the nanorod samples synthesized by sol electrophoretic deposition thus far have been polycrystalline. Although this is perfectly acceptable for many conceivable applications, there is still much fundamental interest in the synthesis of single crystal nanorods. As such, one could pursue several methods that may work for the synthesis of oxide nanorods.

First, there is the suggestion put forth by Martin et al[80] that nanorods below a certain critical size may be single crystal. This could be pursued in a number of oxide systems. Second, there is the idea of using electrochemical methods like those of Miao et al[100] to synthesize single crystal nanorods. Research in this direction is already underway in the synthesis of V_2O_5 nanorods. Lastly, there are a number of other possibilities that may be useful for synthesis of some single-crystal nanorods, including use of crystalline colloids, hydrothermal treatment of the deposits or use of an epitaxial template.

5.2.5 Other considerations

Additionally, there remain a few areas of work with respect to the materials already synthesized. Particularly, there is a great interest in attempting the synthesis of more nanorods in AAM templates and other sizes of PC templates.

Many of the potential applications for the types of oxide nanorods synthesized (or under consideration) would be greatly enhanced by the formation of parallel arrays of nanorods upright on a surface. So far, this has mostly been accomplished by

attaching a filled template (after nanorods growth) to the desired surface with an adhesive, followed by removal of the template. Although effective, this method requires several steps, and is not optimal for forming electrical contact between the nanorods and the substrate. To overcome this, one could use a method whereby an AAM template is formed directly onto a conducting substrate (such as ITO glass)[7]. This conductive substrate would serve as the working electrode during nanorod growth, with the deposited nanorods being directly in contact with the ITO. Upon removal of the anodic alumina template, this would leave an array of oxide nanorods directly attached to the ITO glass substrate.

Notes to Chapter 5

[1] Basu, S.; Sharma, M.M. *J. Membrane Sci.* **1997**, *124*, 77.

[2] Green, D.L.; Lin, J.S.; Lam, Y.-F.; Hu, M.Z.-C.; Schaefer, D.W.; Harris, M.T. *J. Colloid Interf. Sci* **2003**, *266*, 346.

[3] Zhao, G.; Kozuka, H.; Lin, H.; Yoko, T. *Thin Solid Films* **1999**, *339*, 123.

[4] Yu, J.C.; Lin, J.; Kwok, R.W.M. *J. Photoch. Photobio. A* **1997**, *111*, 199.

[5] Radovanovic, P.V.; Gamelin, D.R.; *J. Am. Chem. Soc.* **2001**, *123*, 12207.

[6] Lu, S.; Hou, L.; Gan, F. *J. Mater. Sci.* **1993**, *28*, 2169.

[7] Chu, S.-Z.; Wada, K.; Inoue, S.; Todoroki, S.-I.; Takahashi, Y.K.; Hono, K. *Chem. Mater.* **2002**, *14*, 4595.

Appendix A

Table A-1 Symbols used in this work

Symbol	Definition	Typical Units	Equations
α	Absorption coefficient	cm^{-1}	2-1
α_l	Longitudinal polarizability		4-1, 4-2
α_t	Transverse polarizability		4-1, 4-2
δ	Deposit thickness	m	2-16, 2-17
ε	Permittivity of TiO_2	F/m	2-2
ε_0	Electric constant	F/m	1-2, 1-3, 2-4, 2-6
ε_c	Effective permittivity of deposit	F/m	2-17
ε_c	Core dielectric constant	None	4-2
ε_L	Permittivity of liquid	F/m	2-16, 2-17
ε_m	Matrix dielectric constant	None	4-1, 4-2
ε_r	Dielectric constant of medium (sol)	None	1-1, 1,-2, 1,-3, 2-4, 2-6
ε_s	Complex shell dielectric constant	None	4-2
η	Overpotential	mV	2-18
η	Viscosity	Pa-s	1-3, 2-6, 2-16
φ_c	Cast packing factor	None	2-16
φ_s	Volume concentration of particles	$Number/m^3$	2-16
κ	Sol conductivity	S/cm	2-18
κ	1/ Debye length (size of electrical double layer)	nm^{-1}	1-1, 1-2, 2-4
λ	Wavelength	m	4-1

Symbol	Definition	Typical Units	Equations
μ	Electrophoretic mobility	m/V-s	1-3, 2-10, 2-13, 2-14
μ	Reduced effective exciton mass	kg	2-2
ν	Frequency	Rad/s	2-1
$\rho_{deposit}$	Density of deposit	kg/m^3	2-13,2-14
ρ_{sol}	Resistivity of the sol	Ohm-m	2-7, 2-9, 2-11
ρ_{TiO2}	Resistivity of TiO_2 deposit	Ohm-m	2-8
σ	Absorbance		4-1
ζ	Zeta potential	mV	1-1, 1-3, 2-4, 2-6, 2-16
a	Size of nanoparticle	nm	1-1, 2-5
A	Hamaker's constant	J	2-5
A_c	Cross-sectional area of growth cell	m^2	2-11, 2-12
$A_{deposit}$	Area of deposit	m^2	2-13
A_p	Pore cross-sectional area	m^2	2-7 through 2-10
c	Sol concentration	kg/m^3	2-12, 2-13, 2-14
d	Distance between electrodes	M	2-10, 2-11, 2-12, 2-14, 2-16, 2-17
d_l	Thickness of deposit	M	2-7 through 2-10, 2-12, 2-14
e	Electron charge	C	1-2, 2-2,
E	Electric field	V/m	2-6, 2-13
e_c	Core shape factor	None	4-3, 4-5, 4-7
E_g	Band-gap energy	J	2-1, 2-2
E_s	Electric field	V/m	2-17
e_s	Shell shape factor	None	4-3, 4-5, 4-8
f	Volume fraction of core	None	4-2

Symbol	Definition	Typical Units	Equations
h	Planck constant	J-s	2-1, 2-2
H	Separation distance	m	2-4
h	Dimensionless separation distance (H/a)	None	2-5
I	Current	mA	2-15
i	Current density	mA/cm^2	2-18
k	Boltzmann constant	J/K	1-2,
l	Characteristic length	cm	2-18
l	Length of core/shell nanorod	m	4-8
$M_{deposit}$	Mass of deposit	kg	2-13
n_i	Bulk concentration of i^{th} ion	$Number/m^3$	1-2
N_p	Pore density	$Number/m^2$	2-7 through 2-10
P (4 different values)	Depolarization factors		4-2 through 4-6
Q	Charge on a particle	C	1-2
Q	Effective charge per unit mass	C/kg	2-10, 2-12
R	Particle size	m	2-2
r	Core radius	m	4-7, 4-8
$R_{n,p}$	Resistance in section n due to the particles	Ohm	2-8, 2-10, 2-12, 2-15
$R_{n,sol}$	Resistance in section n due to the sol	Ohm	2-7, 2-9, 2-11, 2-15
s	Template thickness	m	2-8, 2-11
T	Temperature	K	1-2,
t_s	Shell thickness	m	4-8
v	Nanoparticle velocity	m/s	2-6
V	Voltage drop	V	2-14, 2-15

Symbol	Definition	Typical Units	Equations
V	Volume per particle	m^3	4-2
V_A	Attractive energy (van der Waals)	J	2-3, 2-5
V_a	Applied voltage	V	2-15, 2-16
$V_{deposit}$	Volume of deposit	m^3	2-13
V_R	Electrostatic repulsion energy	J	2-3, 2-4
V_t	Total interaction energy	J	2-3
W_a	Wagner number	None	2-18
z_i	Valence of i^{th} ion	None	1-2

Appendix B

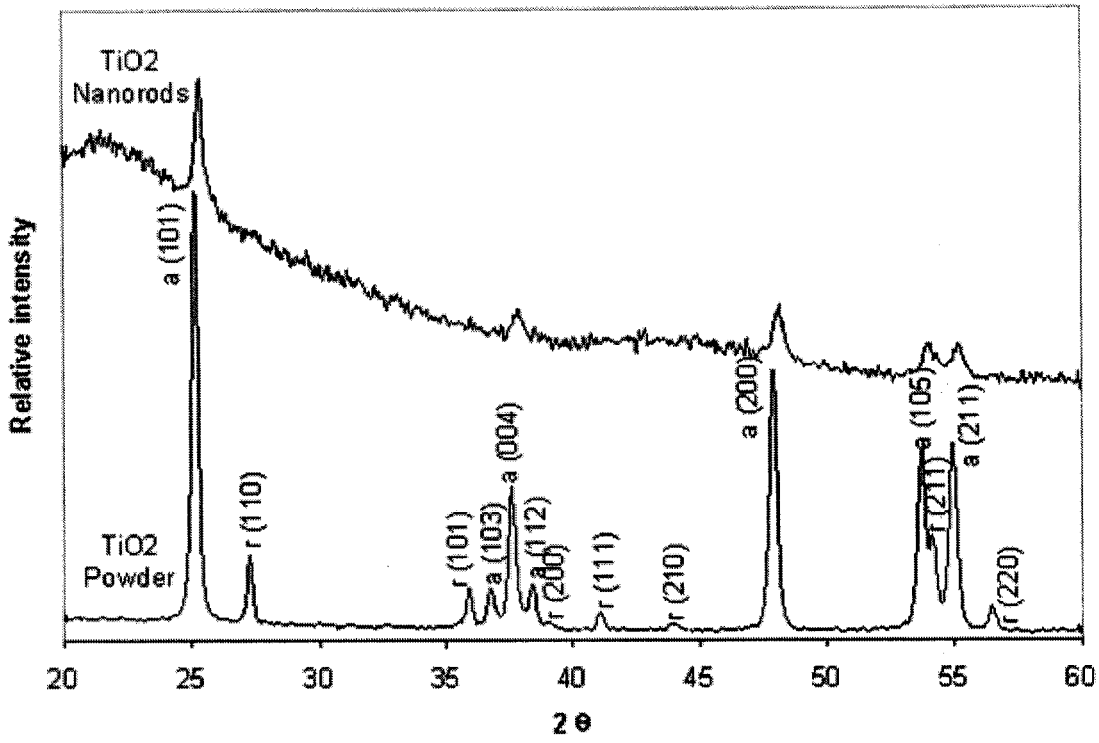

Figure B-1 X-ray diffraction of TiO_2 nanorods and powders fired at 700 deg C, showing both anatase and rutile phases.

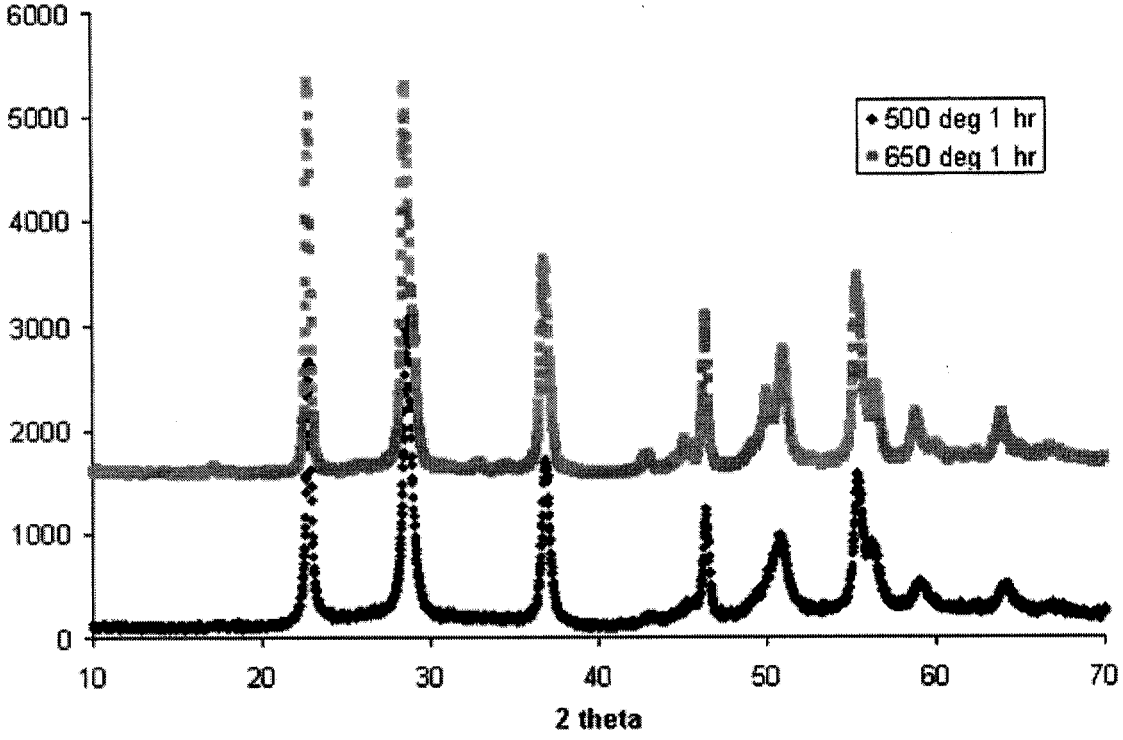

Figure B-2 X-ray diffraction of Nb_2O_5 powders fired at both 500 and 650 deg C.

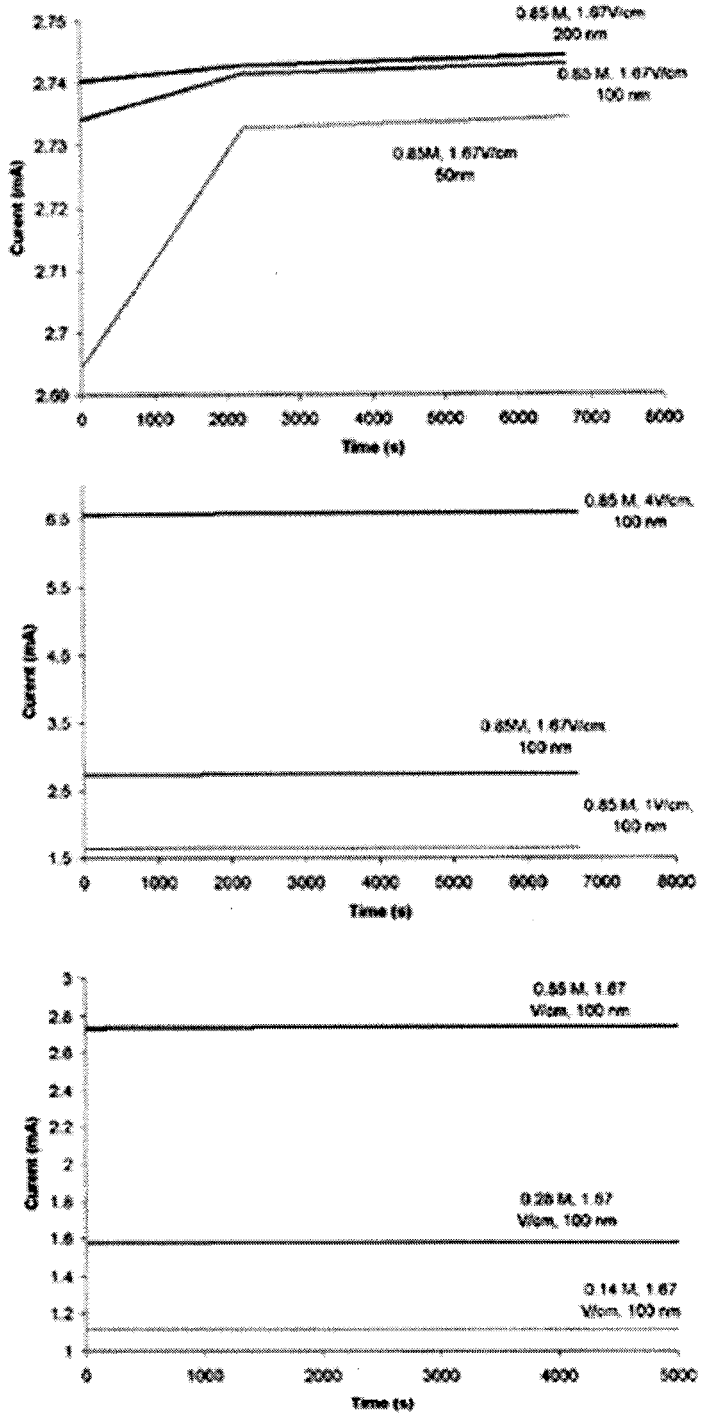

Figure B-3 Computed currents during nanorod growth from first model. Top, different templates. Middle, different fields. Bottom, different concentrations.

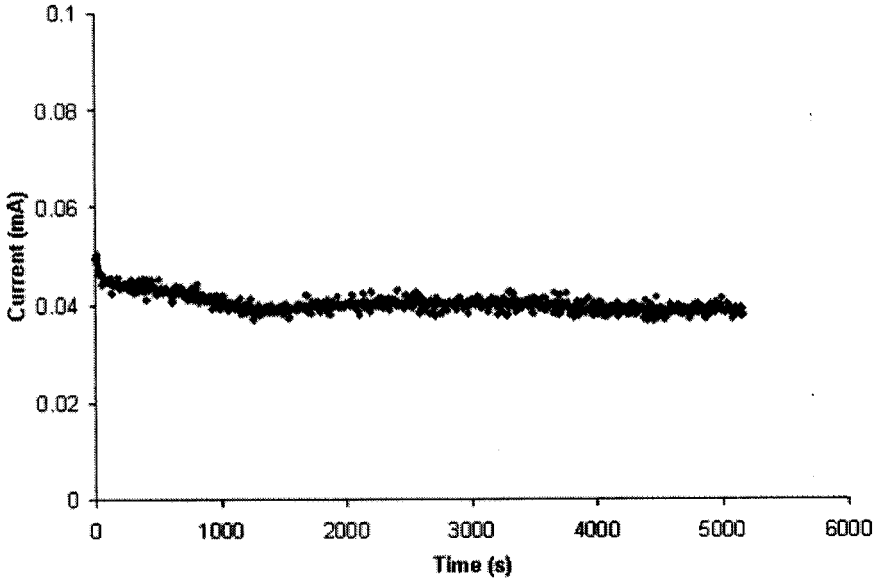

Figure B-4 Recorded current for solution without nanoparticles in 100 nm PC template at 1.67 V/cm.

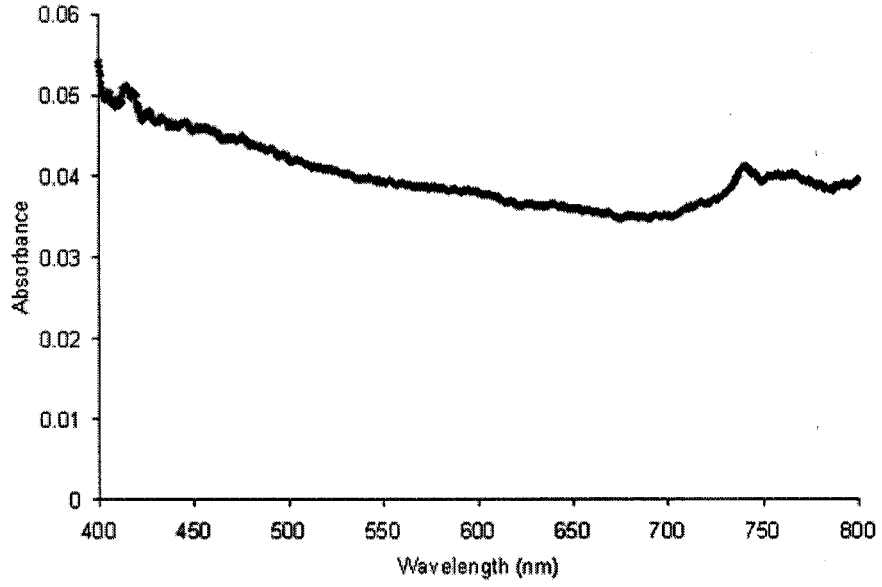

Figure B-5 Absorbance of water-ethanol mixture in plastic cuvette.

Bibliography

1. Aegerter, M.A. *Sol. Energ. Mat. Sol. C.* **2001**, *68*, 401.
2. Aegerter, M.A.; Avellaneda, C.O.; Pawlicka, A.; Atik, M. *J. Sol-Gel Sci. Techn.* **1997**, *8*, 689.
3. Ah, C.S.; Hong, S.D.; Jang, D.-J. *J. Phys. Chem. B* **2001**, *105*, 7871.
4. Ajayan, P.M. ; Ebbesen, T.W.; Ichihashi, T.; Iijima, S.; Tanigaki, K.; Hiura, H. *Nature* **1993**, *362*, 522.
5. Ajayan, P.M.; Iijima, S. *Nature* **1993**, *361*, 333.
6. Ajayan, P.M.; Stephan, O.; Redlich, P.; Colliex, C. *Nature* **1995**, *375*, 564.
7. Alam, M.J.; Cameron, D.C. *Thin Solid Films* **2000**, *377-378*, 455.
8. Alam, M.J.; Cameron, D.C. *Thin Solid Films* **2000**, *377-378*, 455.
9. Atkins, P., *Physical Chemistry*, 5th Ed., Oxford University Press, Oxford, 1994.
10. Bachmann, R.; Barner, K. *Solid State Commun.* **1998**, *68*, 865.
11. Bai, Z.G.; Yu, D.P.; Zhang, H.Z.; Ding, Y.; Wang, Y.P.; Gai, X.Z.; Hang, Q.L.; Xiong, G.C.; Feng, S.Q. *Chem. Phys. Lett.* **1999**, *303*, 311.
12. Barati, M.; Sadeghi, E. *Nanotechnology* **2001**, *12*, 277.
13. Barboux-Doeuff, S.; Sanchez, C. *Mat. Res. Bull.* **1994**, *29*, 1.
14. Basu, G.; Yeranos, W.; Belford, R.L. *Inorg. Chem.* **1964**, *3*, 929.
15. Basu, S.; Chatterji, K.K. *Z. Phys. Chem. (Leipzig)* **1958**, *209*, 360.
16. Basu, S.; Sharma, M.M. *J. Membrane Sci.* **1997**, *124*, 77.
17. Bel Hadj Tahar, R.; Ban, T.; Ohya, Y.; Takahashi, Y. *J. Appl. Phys.* **1998**, *83*, 2631.
18. Bergström, L. *Advan. Colloid Interface Sci.* **1997**, *70*, 125.
19. Bernal, I.; Rieger, P.H. *Inorg. Chem.* **1963**, *2*, 256.
20. Bhatia, R.B.; Brinker, C.J.; Gupta, A.K.; Singh, A.K. *Chem. Mater.* **2000**, *12*, 2434.
21. Brinker, C.J.; Scherer, G.W. *Sol-gel science : the physics and chemistry of sol-gel processing*, Academic Press, Boston, 1990.

22. Brinker, C.J.; Scherer, G.W. *Sol-Gel Science: the Physics and Chemistry of Sol-Gel Processing*, Academic Press, San Diego, CA, 1990.
23. Bruyère, V.I.E.; Morando, P.J.; Blesa, M.A. *J. Colloid Interf. Sci.* **1999**, *209*, 207.
24. Bueno, P.R.; Leite, E.R. *J. Phys. Chem. B* **2003**, *107*, 8868.
25. Bueno, P.R.; Leite, E.R.; Giraldi, T.R.; Bulhojes, L.O.S.; Longo, E. *J. Phys. Chem B* **2003**, *107*, 8878.
26. Callister, W.D. *Materials Science and Engineering: An Introduction*, John Wiley & Sons, New York, 1997.
27. Cao, G.Z. In *Nanostructures and Nanomaterials: Synthesis, Properties, and Applications*, Imperial College Press, London, 2004.
28. Caruso, F.; Spasova, M.; Salgueiriño-Maceira, V.; Liz-Marzán, L.M. *Adv. Mater.* **2001**, *13*, 1090.
29. Chan, C.M.; Cao, G.Z.; Fong, H.; Sarikaya, M.; Robinson, T.; Nelson, L. *J. Mater. Res.* **2000**, *15*, 148.
30. Chattopadhyay, S. *Nanostruct. Mater.* **1997**, *9*, 551.
31. Chen, Q.; Zhou, W.; Du, G.; Peng, L.-M. *Adv. Mater.* **2002**, *14*, 1208.
32. Chen, X.; Hu, X.; Feng, J. *Nanostruct. Mater.* **1995**, *6*, 309.
33. Chen, Y.K.; Green, M.L.H.; Tsang, S. C. *Chem. Comm.* **1996**, 2489.
34. Cheng, B.; Samulski, E.T. *J. Mater. Chem.* **2001**, *11*, 2901.
35. Chu, S.-Z.; Wada, K.; Inoue, S.; Todoroki, S.-I.; Takahashi, Y.K.; Hono, K. *Chem. Mater.* **2002**, *14*, 4595.
36. Cullity, B.D. *Elements of X-Ray Diffraction*, **2**nd edition, Addison-Wesley, Reading, MA, 1978.
37. Dabbousi, B.O.; Rodriguez-Viejo, J.; Mikulec, F. V.; Heine, J.R.; Mattoussi, H.; Ober, R.; Jensen, K.F.; Bawendi, M.G. *J. Phys. Chem. B* **1997**, *101*, 9463.
38. Dai, Z.R.; Pan, Z.W.; Wang, Z.L. *Solid State Commun.* **2001**, *118*, 351.
39. Dawson; A.; Kamat, P.V. *J. Phys. Chem. B* **2001**, *105*, 960.
40. Del Monte, F.; Larsen, W.; Mackenzie, J.D. *J. Am. Ceram. Soc.* **2000**, *83*, 1506.
41. Doeuff, S.; Henry, M.; Livage, J. *Mat. Res. Bull.* **1990**, *25*, 1519.
42. Doeuff, S.; Henry, M.; Sanchez, C.; Livage, J., *J. Non-Cryst. Solids* **1987**, *89*, 206.

43. Duff, G.; Baiker, A.; Edwards, P.P. *Langmuir* **1993**, *9*, 2301.

44. Emons, T.T.; Li, J.; Nazar, L.F. *J. Am. Chem. Soc.* **2002**, *124*, 8516.

45. Enzel, P.; Zoller, J.J.; Bein, T. *Chem. Comm.* **1992**, 633.

46. Fan, S.; Chapline, M.G.; Franklin, N.R.; Tombler, T.W.; Cassell, A.M.; Dai, H. *Science* **1999**, *283*, 512.

47. Feldman, L.C.; Mayer, J.W. *Fundamentals of Surface and Thin Film Analysis, Elsevier Science Publishing Co., Inc.*, New York, NY, 1986.

48. Feng, X.; Fryxell, G.E.; Wang, L.-Q.; Kim, A.Y.; Liu, J.; Kemner, K.M. *Science* **1997**, *276*, 923.

49. Fleisher, R.L.; Price, P.B.; Walker, R.M. *Nuclear Tracks in Solids*, University of California Press, Berkeley, CA, 1975.

50. Forouhi, A.R.; Bloomer, I. *Phys. Rev. B* **1986**, *34*, 7018.

51. Fu, Y.; Chen, J.; Zhang, H. *Chem. Phys. Lett.* **2001**, *350*, 491.

52. Furneaux, R.C.; Rigby, W.R.; Davidson, A.P. *Nature* **1989**, *337*, 147.

53. Gaskell, D.R. *Introduction to the Theromodynamics of Materials*, Taylor and Francis, Washington, D.C., 1995.

54. González-Cuenca, M.; Biesheuvel, P.M.; Verweij, H., *AIChE J.* **2000**, *46*, 626.

55. Govender, K.; Boyle, D.S.; O'Brien, P.; Binks, D.; West, D.; Coleman, D. *Adv. Mater.* **2002**, *14*, 1221.

56. Green, D.L.; Lin, J.S.; Lam, Y.-F.; Hu, M.Z.-C.; Schaefer, D.W.; Harris, M.T. *J. Colloid Interf. Sci* **2003**, *266*, 346.

57. Gu, G.; Zheng, B.; Han, W.Q.; Roth, S.; Liu, J. *Nano Lett.* **2002**, *2*, 849.

58. Gu, Y. *J. Colloid Interf. Sci* **2000**, *231*, 199.

59. Gu, Y.; Li, D. *J. Colloid Interf. Sci.* **1999**, *217*, 60.

60. Guanghui, F.U.; Jiafeng, D.U.; Donghui, P.A.N.; Ouli, H.E. *J. Non-Cryst. Solids* **1989**, *112*, 454.

61. Guerret-Piecourt, C.; Le Bouar, Y.; Loiseau, A.; Pascard, H. *Nature* **1994**, *372*, 761.

62. Gundian, G.; Govindaraj; A.; Rao, C.N.R. *Chem. Phys. Lett.* **2002**, *351*, 189.

63. Guo, L.; Cheng, J.X.; Li, X.-Y.; Yan, Y.J.; Yang, S.H.; Yang, C.L.; Wang, J.N.; Ge, W.K. *Mat. Sci. Eng. C* **2001**, *16*, 123.

64. Guo, L.; Wu, Z.; Liu, T.; Wang, W.; Zhu, H. *Chem. Phys. Lett.* **2000**, *318*, 49.

65. Hall, S.R.; Davis, S.A.; Mann, S. *Langmuir* **2000**, *16*, 1454.

66. Hanrath, T.; Korgel, B.A. *Adv. Mater.* **2003**, *15*, 437.

67. Hanrath, T.; Korgel, B.A. *J. Am. Chem. Soc.* **2002**, *124*, 1424.

68. Hasegawa, K.; Kunugi, S.; Tatsumisago, M.; Minami, T. *J. Sol-Gel Sci. Tech.* **1999**, *15*, 243.

69. Hashimoto, M.; Koreeda, T.; Koshida, N.; Komuro, M.; Atoda, N. *J. Vac. Sci. Technol. B* **1998**, *16*, 2767.

70. Huang, L.; Wang, H.; Wang, Z.; Mitra, A.; Zhao, D.; Yan, Y. *Chem. Mater.* **2002**, *14*, 876.

71. Huang, M.H.; Wu, Y.; Feick, H.; Tran, N.; Weber, E.; Yang, P. *Adv. Mater.* **2001**, *13*, 113.

72. Hunter, R.J. *Zeta Potential in Colloid Science*, Academic Press, London, 1981.

73. Hunter, R.J. *Zeta Potential in Colloid Science: Principles and Applications*, Academic Press, London, 1981.

74. Ivanda, M.; Musić, S.; Popović, S.; Gotić, M., *J. Mol. Struct.* **1999**, *480-481*, 645.

75. Jiang, X.; Herricks, T.; Xia, Y. *Nano. Lett.* **2002**, *2*, 1333.

76. Kamei, M.; Shigesato, Y.; Takaki, S. *Thin Solid Films* **1995**, *259*, 38.

77. Kan S.,; Mokari, T.; Rothenberg, E.; Banin, U. *Nature Mater.* **2003**, *2*, 155.

78. Kang, B.-S.; Gu-Choi, D.; Choi, S.-K. *J. Mater. Sci.: Mater. Electron.* **1998**, *9*, 139.

79. Kanno, I.; Hayashi, S.; Kitagawa, M.; Takayama, R.; Hirao, T. *Appl. Phys. Lett.* **1995**, *66*, 145.

80. Kanzig, W. *Phys. Rev.* **1955**, *98*, 549.

81. Kavan, L.; O'Regan, B.; Kay, A.; Grätzel, M. *J. Electroanal. Chem.* **1993**, *346*, 291.

82. Kenane, S.; Piraux, L. *J. Mater. Res.* **2002**, *17*, 401.

83. Kim, K.J.; Fane, A.G.; Nyström, M.; Pihlajamaki, A. *J. Membrane Sci.* **1997**, *134*, 199.

84. Kolmakov, A.; Zhang, Y.; Cheng, G.; Moskovits, M., *Adv. Mater.* **2003**, *15*, 997.

85. Kosmulski, M. *Langmuir* **1997**, *13*, 6315.

86. Kosmulski, M.; Matijević, E. *Colloid. Surface.* **1992**, *64*, 57.

87. Kreibig, U.; Vollmer, M. *Optical Properties of Metal Clusters*; Springer-Verlag, Berlin, 1995.

88. Kumar, R.V.; Koltypin, Y.; Gedanken, A.; Felner, I. *J. Appl. Phys.* **2001**, *89*, 6324.

89. Kumar, S.R.; Suresh, C.; Vasudevan, A.K.; Perumal, P.; Warrier, K.G.K. *Trans. Indian Ceram. Soc.* **1999**, *58*, 118.

90. Kurihara, K.; Iwadate, K.; Namatsu, H.; Nagase, M.; Murase, K. *J. Vac. Sci. Technol. B* **1995**, *13*, 2170.

91. Lakshmi, B.B.; Dorhout, P.K.; Martin, C.R. *Chem. Mater.* **1997**, *9*, 857.

92. Lakshmi, B.B.; Patrissi, C.J.; Martin, C.R. *Chem. Mater.* **1997**, *9*, 2544.

93. Lao, J.; Huang, J.; Wang, D.; Ren, Z., *Adv. Mater.* **2004**, *16*, 65.

94. Leaustic, A.; Babonneau, F.; Livage, J. *Chem. Mater.* **1989**, *1*, 248.

95. Lefevre, M.J.; Speck, J.S.; Schwartz, R.W.; Dimos, D.; Lockwood, S.J. *J. Mater. Res.* **1996**, *11*, 2076.

96. Lei, Y.; Zhang, L.D.; Fan, J.C. *Chem. Phys. Lett.* **2001**, *338*, 231.

97. Lei, Y.; Zhang, L.D.; Meng, G.W.; Li, G.H.; Zhang, X.Y.; Liang, C.H.; Chen, W.; Wang, S.X. *Appl. Phys. Lett.* **2001**, *78*, 1125.

98. Lettmann, C.; Möckel, D.; Staude, E. *J. Membrane Sci.* **1999**, *159*, 243.

99. Li, D.; Herricks, T.; Xia, Y. *Appl. Phys. Lett.* **2003**, *83*, 4586.

100. Li, D.; Xia, Y. *Nano. Lett.* **2003**, *3*, 555.

101. Li, Y.; Cheng, G.S.; Zhang, L.D. *J. Mater. Res.* **2000**, *15*, 2305.

102. Li, Y.; Wan, J.; Gu, Z. *Mat. Sci. Eng. A* **2000**, *286*, 106.

103. Li,C.; Zhang, D.; Liu, X.; Han, S.; Tang, T.; Han, J.; Zhou, C. *Appl. Phys. Lett.* **2003**, *82*, 1613.

104. Liang, C. H.; Meng, G. W.; Wang, G. Z.; Wang, Y. W.; Zhang, L. D.; Zhang, S. Y. Appl. Phys. Lett. 2001, 78, 3202.

105. Liao, H.W.; Wang, Y.F.; Liu, X.M.; Li, Y.D.; Qian, Y.T. *Chem. Mater.* **2000**, *12*, 2819.

106. Lide, D.R., Ed. *CRC Handbook of Chemistry and Physics, 74th ed.*, CRC Press, Boca Raton, 1994.

107. Lieber, C.M. *Solid State Commun.* **1998**, *107*, 607.

108. Limmer, S.J.; Cao, G.Z. *Adv. Mater.* **2003**, *15*, 427.

109. Link, S.; El-Sayed, M.A. *Int. Rev. Phys. Chem.* **2000**, *19*, 409.

110. Liu, H.I.; Biegelsen, D.K.; Ponce, F.A.; Johnson, N.M.; Pease, R.F. *Appl. Phys. Lett.* **1994**, *64*, 1383.

111. Liu, J.; Coleman, J.P. *Mat. Sci. Eng. A-Struct.* **2000**, *286*, 144.

112. Liu, Y.; Wang, G.; Xua, C.; Wang, W. *Chem. Comm.* **2002**, 1486.

113. Liu, Y.; Yin, C.; Wang, W.; Zhan, Y.; Wang, G. *J. Mater. Sci. Lett.* **2002**, *21*, 137.

114. Liu, Y.; Zheng, C.; Wang, W.; Yin, C.; Wang, G. *Adv. Mater.* **2001**, *13*, 1883.

115. Livage, J.; Henry, M. In *Ultrastructure Processing of Advanced Ceramics*, John Wiley & Sons, New York, NY,1988.

116. Liz-Marzan, L.M., *Materials Today* **2004**, *7*, 26.

117. Lu, S.; Hou, L.; Gan, F. *J. Mater. Sci.* **1993**, *28*, 2169.

118. Ma, J.; Zhang, R.; Liang,, C.H.; Weng, L. *Mater. Lett.* **2003**, *57*, 4648.

119. Ma, X.; Zhang, H.; Xu, J.; Niu, J.; Yang, Q.; Sha, J.; Yang, D. *Chem. Phys. Lett.* **2002**, *363*, 579.

120. Manna, L.; Scher, E.C.; Li, L.-S; Alivisatos, A.P. *J. Am. Chem. Soc.* **2002**, *124*, 7136.

121. Mardare, D.; Hones, P. *Mat. Sci. Eng. B* **1999**, *68*, 42.

122. Masuda, H.; Ohya, M.; Nishio, K.; Asho, H.; Nakao, M.; Nohtomi, M.; Yokoo, A; Tamamura, T. *Jpn. J. Appl. Phys. 2* **2000**, *39*, L1039.

123. McNaught, A.D.; Wilkinson, A., Eds, *Compendium of chemical terminology: IUPAC recommendations*, Blackwell Science, Oxford, 1997

124. Miao, Z.; Xu, D.; Ouyang, J.; Guo, G.; Zhao, X.; Tang, Y. *Nano Lett.* **2002**, *2*, 717.

125. Mie, G. *Ann. Phys.* **1908**, *25*, 329.

126. Min, Y.-S.; EBae, E.J.; Jeong, K.S.; Cho, Y.J.; Lee, J.-H.; Choi, W.B.; Park, G.-S., *Adv. Mater.* **2003**, *15*, 1019.

127. Mosaddeq-ur-Rahman, M.; Yu, G.; Krishna, K.M.; Soga, T.; Watanabe, J.; Jimbo, T.; Umeno, M. *Appl. Optics* **1998**, *37*, 691.

128. Muster, J.; Kim, G.T.; Krstic, V.; Park, J.G.; Park, Y.W.; Roth, S.; Burghard, M. *Adv. Mater.* **2000**, *12*, 420.

129. Nabavi, M.; Doeuff, S.; Sanchez, C.; Livage, J. *Mater. Sci. Eng. B* **1989**, *3*, 203.

130. Nakamoto, K. *Infrared and Raman Spectra of Inorganic and Coordination Compounds*, 3rd ed., John Wiley & Sons, New York, 1978

131. Nass, R.; Schmidt, H. *J. Non-Cryst. Solids* **1990**, *121*, 329.

132. Natarajan, C.; Nogami, G. *J. Electrochem. Soc.* **1996**, *143*, 1547.

133. Navarro, A.; Alcock, J.R.;. Whatmore, R.W. *J. Eur. Ceram. Soc.* **2004**, *24*, 1073.

134. Newnham, R.E.; Udayakumar, K.R.; Trolier-McKinstry, S. In *Chemical Processing of Advanced Materials* (Hench, L.L.; West, J.K., Ed.), John Wiley and Sons, New York, 1992.

135. Ni, Y.; Ge, X.; Liu, H.; Zhang, Z.; Ye, Q.; Wang, F. *Mater. Lett.* **2001**, *49*, 185.

136. Nishide, T.; Mizukami, F. *Thin Solid Films* **1995**, *259*, 212.

137. Nishino, J.; Teekateerawej, S.; Nosaka, Y. *J. Mater. Sci. Lett.* **2003**, *22*, 1007.

138. Oh, S.H.; Jang, H.M. *J. Appl. Phys.* **1999**, *85*, 2815.

139. Oldenburg, S.J.; Averitt, R.D.; Westcott, S.L.; Halas, N.J. *Chem. Phys. Lett.* **1998**, *288*, 243.

140. Oldenburg, S.J.; Hale, G.D.; Jackson, J.B.; Halas, N.J. *Appl. Phys. Lett.* **1999**, *75*, 1063.

141. Oldenburg, S.J.; Jackson, J.B.; Westcott, S.L.; Halas, N.J. *Appl. Phys. Lett.* **1999**, *75*, 2897.

142. Orel, B.; Maček, M.; Grdadolnik, J.; Meden, A. *J. Solid State Electr.* **1998**, *2*, 221.

143. Pacholski, C.; Kornowski, A.; Weller, H. *Angew. Chem. Int. Ed.* **2002**, *41*, 1188.

144. Pan, D.; Shuyuan, Z.; Chen, Y.; Hou, J.G. *J. Mater. Res.* **2002**, *17*, 1981.

145. Pan, Z.W.; Dai, Z.R.; Wang, Z.L. *Science* **2001**, *291*, 1947.

146. Papet, P.; Le Bars, N.; Baumard, J.F.; Lecomte, A.; Dauger, A. *J. Mater. Sci.* **1989**, **24**, 3850.

147. Park, I.-S.; Jang, S.-R.; Hong, J.S.; Vittal, R.; Kim, K.-J. *Chem. Mater.* **2003**, *15*, 4633.

148. Park, W.I.; Kim, D.H.; Jung, S.-W.; Yi, G.-C. *Appl. Phys. Lett.* **2002**, *80*, 4232.

149. Parks, G.A. *Chem. Rev.* **1965**, *65*, 177.

150. Pascual, J.I.; Méndez, J.; Gómez-Herrero, J.; Baró, A.M.; Garcia, N.; Landman, U.; Luedtke, W.D.; Bogachek, E.N.; Cheng, H.-P. *Science* **1995**, *267*, 1793.

151. Patrissi, C.J.; Martin, C.R. *J. Electrochem. Soc.* **1999**, *146*, 3176.

152. Patzke, G.R.; Krumeich, F; Nesper, R. *Agnew. Chem. Int. Ed.* **2002**, *41*, 2446.

153. Patzke,G.R.; Michailovski, A.; Krumeich, F.; Nesper, R.; Grunwaldt, J.-D.; Baiker, A. *Chem. Mater.* **2004**, *16*, 1126.

154. Peng, X.S.; Meng, G.W.; Wang, X.F.; Wang, Y.W.; Zhang, J.; Liu, X.; Zhang, L.D. *Chem. Mater.* **2002**, *14*, 4490.

155. Peng, X.S.; Wang, Y.W.; Zhang, J.; Wang, X.F.; Zhao, L.X.; Meng, G.W.; Zhang, L.D. *Appl. Phys. A* **2002**, *74*, 437.

156. Penn, R.L.; Banfield, J.F. *Geochim. Cosmochim. Ac.* **1999**, 63, 1549.

157. Pol, V.G.; Palchik, O.; Gedanken, A.; Felner, I. *J. Phys. Chem. B* **2002**, *106*, 9737.

158. Possin, G.E. *Rev. Sci. Instrum.* **1970**, *41*, 772.

159. Prasad, K.V.R.; Raju, A.R.; Varma, K.B.R. *J. Mater. Sci.* **1994**, *29*, 2691.

160. Radovanovic, P.V.; Gamelin, D.R.; *J. Am. Chem. Soc.* **2001**, *123*, 12207.

161. Reed, J.S. *Introduction to Principles of Ceramic Processing*, Wiley, New York, 1988.

162. Reed, J.S. *Introduction to the Principles of Ceramic Processing*, John Wiley & Sons, New York, 1988.

163. Rossetti, Jr., G.A.; Cline, J.P.; Navrotsky, A. *J. Mater. Res.* **1998**, *13*, 3197.

164. Rossetti, Jr., G.A.; Cross, L.E.; Kushida, K. *Appl. Phys. Lett.* **1991**, *59*, 2524.

165. Ryan, J.V.; Berry, A.D.; Anderson, M.L.; Long, J.W.; Stroud, R.M.; Cepak, V.M.; Browning, V.M.; Rolison, D.R.; Merzbacher, C.I. *Nature* **2000**, *406*, 169.

166. Sanchez, C.; Livage, J.; Henry, M.; Babonneau, F. *J. Non-Cryst. Solids* **1988**, *100*, 65.

167. Sarkar, P.; Nicholson, P.S., *J. Am. Ceram. Soc.* **1996**, *79*, 1987.

168. Sarmini, K.; Kenndler, E. *J. Biochem. Biophys. Methods* **1999**, *38*, 123.

169. Satishkumar, B. C., Govindaraj, A.; Natha, M.; Rao, C. N. R. *J. Mater. Chem.* **2000**, *10*, 2115.

170. Satishkumar, B. C.; Govindaraj, A.; Vogl, E.M.; Basumallick, L.; Rao, C.N.R. *J. Mater. Res.* **1997**, *12*, 604.

171. Sedlar, M.; Sayer, M. *J. Sol-Gel Sci. Techn.* **1995**, *5*, 27.

172. Selbin, J. *Chem. Rev.* **1965**, *65*, 153.

173. Seraji, S.; Wu, Y.; Jewell-Larson, N.E.; Forbess, M.J.; Limmer, S.J.; Chou, T.P.; Cao, G.Z. *Adv. Mater.* **2000**, *12*, 1421.

174. Seshadri, K.S.; Kesavamoorthy, R.; Srinivasan, M.P.; Varatharajan, K.; Ahmed, J.; Krishnasamy, V. *B. Electrochem.* **1998**, *14*, 16.

175. Shantha, K.; Varma, K.B.R. *J. Am. Ceram. Soc.* **2000**, *83*, 1122.

176. Shaw, D.J. *Introduction to Colloid and Surface Chemistry,* 4th edition, Butterworth-Heinemann Ltd., Oxford, 1992.

177. Shaw, L.; Abbaschian, R. *J. Am. Ceram. Soc.* **1995**, *78*, 3376.

178. Shaw, T.M.; Trolier-McKinstry, S.; McIntyre, P.C. *Annu. Rev. Mater. Sci.* **2000**, *30*, 263.

179. Shen, Z.Q.; He, L.L.; Wu, E.D.; Fan, Y.Y.; He, J.F.; Cheng, H.M.; Li, D.X.; Ye, H.Q. *J. Mater. Res.* **2002**, *17*, 2761.

180. Shih, C.-W.; Lai, W.-C.; Hwang, C.-C.; Chang, S.-S.; Wang, C.R.C. In *Metal Nanoparticles* (Feldham, D.L.; Foss, Jr., C.A., Ed.), Marcel Dekker, Inc., New York, N.Y., 2002.

181. Simone, A.; Spinelli, P. *Mater. Eng.* **2002**, *13*, 33.

182. Stoica, T.F.; Stoica, T.A.; Vanca, V.; Lakatos, E.; Zaharescu, M. *Thin Solid Films* **1999**, *348*, 273.

183. Sun Y.; Gates, B.; Mayers, B.; Xia, Y *Nano Lett.* **2002**, *2*, 165.

184. Sun, Y.; Gates, B.; Mayers, B.; Xia, Y. *Nano Lett.* **2002**, *2*, 165.

185. Tahan, D.M.; Safari, A.; Klein, L.C. *J. Am. Ceram. Soc.* **1996**, *79*, 1593.

186. Tan, Y.T.; Durrani; Z.A.K.; Ahmed, H. *J. Appl. Phys.* **2001**, *89*, 1262.

187. Tang, C.; Bando, Y.; Sato, T. *J. Phys. Chem. B* **2002**, *106*, 7449.

188. Tian, Z.R.; Voigt, J.A.; Liu, J.; Mckenzie B.; Mcdermott, M.J. *J. Am. Chem. Soc.* **2002**, *124*, 12954.

189. Ting, C.-C.; Chen, S.-Y.; Liu, D.-M. *J. Appl. Phys.* **2000**, *88*, 4628.

190. Tohge, N.; Fujii, E.; Minami, T. *J. Mater. Sci.-Mater. El.* **1994**, *5*, 356.

191. Tonucci, R.J.; Justus, B.L.; Campillo, A.J.; Ford, C.E. *Science* **1992**, *258*, 783.

192. Urban, J.J.; Yun, W.S.; Gu, Q.; Park, H., *J. Am. Chem. Soc.* **2002**, *124*, 1186.

193. Vandeperre, L.J.; van der Biest, O.O. In *Innovative Processing and Synthesis of Ceramics, Glasses, and Composites 1997*, American Ceramic Society, Westerville, Ohio, 1997.

194. Vayssieres, L.; Beermann, N.; Lindquist, S.-E.; Hagfeldt, A. *Chem. Mater.* **2001**, *13*, 233.

195. Villegas, M.A.; Pascual, L. *Thin Solid Films* **1999**, *351*, 103.

196. Visser, J. *Advan. Colloid Interface Sci.* **1972**, *3*, 331.

197. Viswanathamurthi, P.; Bhattarai, N.; Kim, H.Y.; Lee, D.R. *Scripta Mater.* **2003**, *49*, 577.

198. Viswanathamurthi, P.; Bhattarai, N.; Kim, H.Y.; Lee, D.R.; Kim, S.R.; Morris, M.A. *Chem. Phys. Lett.* **2003**, *374*, 79.

199. Wagner, R.S.; In *Whisker Technology* (Levitt, A.P., Ed.), Wiley, New York, 1970.

200. Wagner, R.S.; Ellis, W.C. *Appl. Phys. Lett.* **1964**, *4*, 89.

201. Wagner, R.S.; Ellis, W.C.; Jackson, K.A.; Arnold, S.M. *J. Appl. Phys.* **1964**, *35*, 2993.

202. Wang, W.; Wang, G.; Wang, X.; Zhan, Y.; Liu, Y.; Zheng, C. *Adv. Mater.* **2002**, *14*, 67.

203. Wang, W.; Xu, C.; Wang, G.; Liu, Y.; Zheng, C. *Adv. Mater.* **2002**, *14*, 837.

204. Wang, X.; Li, Y. *Chem. Comm.* **2002**, 764.

205. Wang, X.; Li, Y. *J. Am. Chem. Soc.* **2002**, *124*, 2880.

206. Wang, Y.; Furlan, R.; Ramos, I.; Santiago-Aviles, J.J. *Appl. Phys. A* **2004**, *78*, 2004, 1043.

207. Wang, Y.C.; Leu, I.C.; Hon, M.H. *J. Cryst. Growth* **2002**, *237-239*, 564.

208. Wang, Y.C.; Leu, I.C.; Hon, M.H. *J. Mater. Chem.* **2002**, *12*, 2439.

209. Wang, Y.W.; Liang, C.H.; Wang, G.Z.; Gao, T.; Wang, S.X.; Fan, J.C.; Zhang, L.D. *J. Mater. Sci. Lett.* **2001**, *20*, 1687.

210. Wang, Z.; Chen, J.; Hu, X. *Thin Solid Films* **2000**, *375*, 238.

211. Wang, Z.; Li, H.L. *Appl. Phys. A* **2002**, *74*, 201.

212. Westcott, S.L.; Oldenburg, S.J.; Lee, T.R.; Halas, N.J. *Langmuir* **1998**, *14*, 5396.

213. Won, D.-J.; Wang, C.-H.; Jang, H.-K.; Choi, D.-J. *Appl. Phys. A* **2001**, *73*, 595.

214. Wong, E.W; Sheehan, P.E.; Lieber, C.M. *Science* **1997**, *277,* 1971.

215. Wu, C.-G.; Bein, T. *Science* **1994**, 264, 1757.

216. Wu, H.-Q.; Shao, M.-W.; Wei, X.-W.; Gu, J.-S.; Qu, M.-Z. *Chinese J. Chem.* **2002**, *20*, 610.

217. Wu, J.-J.; Yu, C.-C., *J. Phys. Chem. B.* **2004**, *108*, 3377.

218. Xia, Y.; Rogers, J.A.; Paul, K.E.; Whitesides, G.M. *Chem. Rev.* **1999**, *99*, 1823.

219. Xiao, J.; Xie, Y.; Tang, R.; Qian, Y. *J. Solid State Chem.* **2001**, *161*, 179.

220. Yamamoto, O.; Sasamoto, T. *J. Mater. Res.* **1992**, *7*, 2488.

221. Yamasaki, K.; Sone, K. *Nature* **1950**, *166*, 998.

222. Yin, Y.; Zhang, G.; Xia, Y. *Adv. Funct. Mater.* **2002**, *12*, 293.

223. Yoda, S.; Ohshima, S.; Kamiya, K.; Kawai, A.; Uchida, K.; Gotoh, A.; Ikazaki, F. *J. Non-cryst solids* **1996**, *208*, 191.

224. Yoffe, A.D. *Adv. Phys.* **2001**, *50*, 1.

225. Yu, D.; Yu, W.; Wang, D.; Qian, Y. *Thin Solid Films* **2002**, *419*, 166.

226. Yu, D.P.; Hang, Q.L.; Ding, Y.; Zhang, H.Z.; Bai, Z.G.; Wang, J.J.; Zou, Y.H.; Qian, W.; Xoing, G.C.; Feng, S.Q. *Appl. Phys. Lett.* **1998**, *73*, 3076.

227. Yu, J.C.; Lin, J.; Kwok, R.W.M. *J. Photoch. Photobio. A* **1997**, *111,* 199.

228. Zach, M.P.; Newberg, J.T.; Sierra, L.; Hemminger, J.C.; Penner, R.M., *J. Phys. Chem. B* **2003**, *107*, 5393.

229. Zhang, D.-F.; Sun, L.-D.; Yin, J.-L.; Yan, C.-H., *Adv. Mater.* **2003**, *15*, 1022.

230. Zhang, H.T.; Gui, Z.; Fan, R.; Chen, X.H. *Inorg. Chem. Comm.* **2002**, *5*, 399.

231. Zhang, J.; Sun, L.; Pan, H.; Liao, C.; Yan, C. *New J. Chem.* **2002**, *26*, 33.

232. Zhang, M.; Bando, Y.; Wada, K.; Kurashima, K. *J. Mater. Sci. Lett.* **1999**, 18, 1911.

233. Zhang, Q.; Gao, L.; Guo, J. *J. Eur. Ceram. Soc.* **2000**, *20*, 2153.

234. Zhang, X.; Yao, B.; Zhao, L.; Liang, C.; Zhang, L.; Mao, Y. *J. Electrochem. Soc.* **2001**, *148*, G398.

235. Zhang, Y.; Zhu, J.; Zhang, Q.; Yan, Y.; Wang, N.; Zhang, X. *Chem. Phys. Lett.* **2000**, *317*, 504.

236. Zhang, Y.F.; Tang, Y.H.; Duan, X.F.; Zhang, Y.; Lee, C.S.; Wang, N.; Bello, I.; Lee, S.T. *Chem. Phys. Lett.* **2000**, *323*, 180.

237. Zhang, Z.; Sun, X.; Dresselhaus, M.S.; Ying, J.Y.; Heremans, J. *Phys. Rev. B* **2000**, *61*, 4850.

238. Zhao, G.; Han, G.; Takahashi, M.;Yoko, T. *Thin Solid Films* **2002**, *410*, 14.

239. Zhao, G.; Kozuka, H.; Lin, H.; Yoko, T. *Thin Solid Films* **1999**, *339*, 123.

240. Zheng, M.; Li, G.; Zhang, X.; Huang, S.; Lei, Y.; Zhang, L. *Chem. Mater.* **2001**, *13*, 3859.

241. Zheng, M.; Zhang, L.; Zhang, X.; Zhang, J.; Li, G. *Chem. Phys. Lett.* **2001**, *334*, 298.

242. Zheng, M.J.; Zhang, L.D.; Li, G.H.; Shen, W.Z. *Chem. Phys. Lett.* **2002**, *363*, 123.

243. Zhitomirsky, I. *Adv. Colloid Interf. Sci.* **2002**, *97*, 297.

244. Zhou Y.; Li, H. *J. Mater. Sci* **2002**, *37*, 5261.

245. Zhu, D.; Zhu, H.; Zhang, Y. *Appl. Phys. Lett.* **2002**, *80*, 1634.

Vita

Steven J. Limmer was born in Salt Lake City, Utah. He earned his Bachelor of Science degree in Physics from the University of Utah in 1995, followed by a second Bachelor of Science in Materials Science and Engineering in 1999, also from University of Utah. In 2004, he earned a Doctor of Philosophy at the University of Washington in Materials Science & Engineering.

While persuing his doctorate, Steven received numerous fellowships, including two NSF-IGERT fellowships from the University of Washington Center for Nanotechnology, a Ford Motor Company fellowship and a Joint Institute for Nanoscience fellowship from the University of Washington/Pacific Northwest National Laboratory. He also received an award for TA of the year from the senior class of the MSE department in 2001. He published numerous peer-reviewed journal articles (including seven as first author) and presented at several regional, national and international conferences during his studies at the University of Washington.

List of Publications

Peer-reviewed journals

- "Films and nanorods of transparent conducting oxide ITO by a citric acid sol route," S.J. Limmer, S.V. Cruz, G.Z. Cao, Applied Physics A (2004), 79 (3), 421-424.
- "Synthesis and electrochemical properties of single crystal V_2O_5 nanorod arrays by template-based electrodeposition," K. Takahashi, S.J. Limmer, G.Z. Cao, Journal of Physical Chemistry B, in press.
- "A study on the growth of TiO_2 nanorods using sol electrophoresis", S.J. Limmer, T.P Chou, G.Z. Cao, Journal of Materials Science (2004), 39(3), 895-901.

- "Formation and optical properties of cylindrical gold nanoshells on silica and titania nanorods", S.J. Limmer, T.P Chou, G.Z. Cao, Journal of Physical Chemistry B (2003), 107 (48), 13313 -13318.
- "Sol-gel electrophoretic deposition for the growth of oxide nanorods", S.J. Limmer, G.Z. Cao, Advanced Materials (2003), 15(5), 427-431.
- "Nanorods of various oxides and hierarchically structured mesoporous silica by sol-gel electrophoresis", S.J. Limmer, T.L. Hubler, G.Z. Cao, Journal of Sol-Gel Science and Technology (2003), 26(1/2/3), 577-581.
- "Synthesis of cadmium tungstate films via sol-gel processing", K. Lennstrom, S.J. Limmer, G.Z. Cao, Thin Solid Films (2003), 434(1-2), 55-61.
- "Template-based growth of various oxide nanorods by sol-gel electrophoresis", S.J. Limmer, S. Seraji, Y. Wu, T.P. Chou, C. Nguyen, G.Z. Cao, Advanced Functional Materials (2002), 12(1), 59-64.
- "Influence of tungsten doping on dielectric properties of strontium bismuth niobate ferroelectric ceramics", Y. Wu, S.J. Limmer, T.P. Chou, C. Nguyen, G.Z. Cao, Journal of Materials Science Letters (2002), 21(12), 947-949.
- "Advancement of bismuth layer structured ferroelectrics through substitution/doping and other processing", Y. Wu, S.J. Limmer, G.Z. Cao, Recent Research Developments in Applied Physics (2002), 5, 313-338.
- "Organic-inorganic sol-gel coating for corrosion protection of stainless steel", T.P. Chou, C. Chandrasekaran, S.J. Limmer, C. Nguyen, G.Z. Cao, Journal of Materials Science Letters (2002), 21(3), 251-255.
- "Processing and properties of vanadium doped strontium niobate", S. Seraji, Y. Wu, S.J. Limmer, T. Chou, C. Nguyen, M.J. Forbess, G.Z. Cao, Materials Science & Engineering, B: Solid-State Materials for Advanced Technology (2002), B88(1), 73-78.
- "Electrophoretic growth of lead zirconate titanate nanorods", S.J. Limmer, S. Seraji, M.J. Forbess, Y. Wu, T.P. Chou, C. Nguyen, G.Z. Cao, Advanced Materials (2001), 13(16), 1269-1272.

- "Processing and properties of strontium bismuth vanadate niobate ferroelectric ceramics", Y. Wu, C. Nguyen, S. Seraji, M.J. Forbess, S.J. Limmer, T. Chou, Tammy; G.Z. Cao, Journal of the American Ceramic Society (2001), 84(12), 2882-2888.
- "Doping effect in layer structured $SrBi_2Nb_2O_9$ ferroelectrics", Y. Wu, M.J. Forbess, S. Seraji, S.J. Limmer, T.P. Chou, C. Nguyen, G.Z. Cao, Journal of Applied Physics (2001), 90(10), 5296-5302.
- "Influence of oxygen annealing on the dielectric properties of $SrBi_2(V_{0.1}Nb_{0.9})_2O_9$ ceramics", Y. Wu, M.J. Forbess, S. Seraji, S.J. Limmer, T. Chou, G.Z. Cao, Journal of Physics D: Applied Physics (2001), 34(17), 2665-2669.
- "Organic-inorganic hybrid coatings for corrosion protection", T.P. Chou, C. Chandrasekaran, S.J. Limmer, S. Seraji, Y. Wu, M.J. Forbess, C. Nguyen, G.Z. Cao, Journal of Non-Crystalline Solids (2001), 290(2,3), 153-162.
- "Impedance study of $SrBi_2Ta_2O_9$ and $SrBi_2(Ta_{0.9}V_{0.1})_2O_9$ ferroelectrics", Y. Wu, M.J. Forbess, S. Seraji, S.J. Limmer, T.P. Chou, G.Z. Cao, Materials Science & Engineering, B: Solid-State Materials for Advanced Technology (2001), B86(1), 70-78.
- "Oxygen-vacancy-related dielectric relaxation in $SrBi_2Ta_{1.8}V_{0.2}O_9$ ferroelectrics", Y. Wu, M.J. Forbess, S. Seraji, S.J. Limmer, T.P. Chou, G.Z. Cao, Journal of Applied Physics (2001), 89(10), 5647-5652.
- "Sol-gel-derived mesoporous silica films with low dielectric constants", S. Seraji, Y. Wu, M.J. Forbess, S.J. Limmer, T. Chou, G.Z. Cao; Advanced Materials (2000), 12(22), 1695-1698.
- "Patterned microstructure of sol-gel derived complex oxides using soft lithography", S. Seraji, Y. Wu, N.E. Jewell-Larson, M.J. Forbess, S.J. Limmer, T.P. Chou, G.Z.Cao, Advanced Materials (2000), 12(19), 1421-1424.

Proceedings:

- "Electrochromic and transparent conducting oxide nanorods", S.J. Limmer, K. Takahashi, G.Z. Cao, Nanomaterials and Their Optical Applications, SPIE Proceedings 5224, 2003, 25-32.
- "Template-based growth of vanadia nanorod arrays by electrochemical deposition", K. Takahashi, S.J. Limmer, and G.Z. Cao, Nanomaterials and Their Optical Applications, SPIE Proceedings 5224, 2003, 33-42.
- "Optically Transparent Superhydrophobic Films by Sol-Gel Processing and Self-Assembly", M.H. Shang, Y. Wang, S.J. Limmer, and G.Z. Cao, Nanomaterials and Their Optical Applications, SPIE Proceedings 5224, 2003, 70-77.
- "Growth of oxide nanorods using sol-gel electrophoretic deposition", S.J. Limmer, G.Z. Cao, Guozhong, Electrophoretic Deposition: Fundamentals and Applications (Electrochemical Society Proceedings v. 2002-21) (2002), 271-278.
- "Formation and optical properties of cylindrical gold nanoshells on silica and titania nanorods", S.J. Limmer, T.P. Chou, G.Z. Cao, Guozhong, Proceedings of SPIE - The International Society for Optical Engineering, v 4809, 2002, p 222-230.
- "Template-based growth of various oxide nanorods by sol-gel electrophoresis", S.J. Limmer, S. Seraji, Y. Wu, T.P. Chou, C. Nguyen, G.Z. Cao, Guozhong, International SAMPE Technical Conference (2001), 33 709-719.